DISPLACEMENT ESTIMATION TECHNIQUES FOR ULTRASOUND ELASTGRAPHY

By

Marwan Hassan Hussein Muhammad

A Thesis Submitted to the
Faculty of Engineering at Cairo University
in Partial Fulfillment of the
Requirements for the Degree of
MASTER OF SCIENCE
in
Systems & Biomedical Engineering

FACULTY OF ENGINEERING, CAIRO UNIVERSITY
GIZA, EGYPT
June 2013

Engineer's Name:	Marwan Hassan Hussein Muhammad
Date of Birth:	10/05/1988
Nationality:	Egyptian
E-mail:	marwan.hussein@eng.cu.edu.eg
Phone:	01112972571
Address:	79, Khatem Al-Morsaleen St, Giza.
Registration Date:	4/2012
Awarding Date:	…./…./……..
Degree:	Master of Science
Department:	Systems and Biomedical Engineering Department

Supervisors:

Prof. Dr. Yasser M. Kadah

Examiners:

Prof. Dr. Yasser M. Kadah   (Thesis main advisor)
Prof. Dr. AbdAllah Sayed Ahmed   (Internal examiner)
Prof. Dr. Mohamed Ibrahim Al-Adawi (External examiner)

Title of Thesis: Displacement Estimation Techniques for Ultrasound Elastography

………………………………………………………………………………………
………………………………………………………………………………………

Key Words:

Ultrasound elastography; displacement estimation; displacement field; block matching algorithms; continuity constraints; optimized exhaustive search.

Summary:

Elastography is a promising medical imaging modality to image the distribution of elastic properties in a region of interest. This technique maps the distribution of parameters related to the mechanical attributes in the target to color coded visual information. In medical imaging, elastography is being studied for its potential as a diagnostic tool in detecting pathological changes in soft tissues by monitoring stiffness changes. For instance, scirrhous carcinoma appears as extremely hard nodules in the breast elastogram.

Many approaches to displacement estimation in ultrasound elastography exist. The standard estimation technique, which is based on 1D gated crosscorrelation, has some disadvantages. It cannot operate well under high applied compression and does not utilize inherent smoothness in tissues. This leads to redundant searches for successive radio frequency segments and occurrence of false detections.

It can be noticed that displacement estimation in elastography is similar to the motion estimation phase in video compression domain. Although some differences exist between the natures of the ultrasonic image and the photographic image, 2D block matching algorithms can be used with ultrasound radio frequency frames to generate displacement fields.

In this study, we review the basic principles underlying elastography. Then, we introduce steps of standard gated 1D crosscorrelation elastography and the impact each step has on signal-to-noise ratio, contrast-to-noise ratio and computation time of elastogram. Then, we propose a modified version of one of the 2D block matching algorithms which make it more oriented to work with US data. We also utilize the inherent continuity in the imaged tissue to make an optimized version of the previously modified algorithm. Additional constraints on the displacement estimation are imposed to reduce discontinuities. We tested the effects of some parameters and postprocessing on the estimation output. Quantitative and visual assessments of the resulting elastograms show that the new technique does not suffer from the same drawbacks of the standard technique. We conclude with potential future work to enhance the quality and runtime of the proposed 2D displacement estimation method.

Acknowledgment

Dedication

To my Mother, nothing can describe your love and care..

Table of Contents

List of Tables

List of Figures

Abstract

Elastography is a promising medical imaging modality to image the distribution of elastic properties in a region of interest. This technique maps the distribution of parameters related to the mechanical attributes in the target to color coded visual information. In medical imaging, elastography is being studied for its potential as a diagnostic tool in detecting pathological changes in soft tissues by monitoring stiffness changes. For instance, scirrhous carcinoma appears as extremely hard nodules in the breast elastogram.

Many approaches to displacement estimation in ultrasound elastography exist. The standard estimation technique, which is based on 1D gated crosscorrelation, has some disadvantages. It cannot operate well under high applied compression and does not utilize inherent smoothness in tissues. This leads to redundant searches for successive radio frequency segments and occurrence of false detections.

It can be noticed that displacement estimation in elastography is similar to the motion estimation phase in video compression domain. Although some differences exist between the natures of the ultrasonic image and the photographic image, 2D block matching algorithms can be used with ultrasound radio frequency frames to generate displacement fields.

In this study, we review the basic principles underlying elastography. Then, we introduce steps of standard gated 1D crosscorrelation elastography and the impact each step has on signal-to-noise ratio, contrast-to-noise ratio and computation time of elastogram. Then, we propose a modified version of one of the 2D block matching algorithms which make it more oriented to work with US data. We also utilize the inherent continuity in the imaged tissue to make an optimized version of the previously modified algorithm. Additional constraints on the displacement estimation are imposed to reduce discontinuities. We tested the effects of some parameters and postprocessing on the estimation output. Quantitative and visual assessments of the resulting elastograms show that the new technique does not suffer from the same drawbacks of the standard technique. We conclude with potential future work to enhance the quality and runtime of the proposed 2D displacement estimation method.

Chapter 1 : Introduction

Elastography is an established medical imaging modality used to image the distribution of elastic properties such as stiffness and elastic moduli as well as viscoelastic and poroelastic properties in a region of interest [1]. This technique maps the distribution of parameters related to the mechanical attributes in the target to color coded visual information. In medical imaging, elastography is being studied for its potential as a diagnostic tool in detecting pathological changes in soft tissues [2].

1.1. Motivation

1.1.1. Conventional detection of cancers and cirrhosis

Long before medical imaging, palpation was an important clinical examination method, and was practiced by the ancient Egyptians about 5000 years ago. The first treatise in the book of the heart at the Edwin Smith and Ebers Papyrus, a part is shown in Figure 1.1, is entitled "Beginning of the secret of the physician" and written between 1500 and 3000 B.C. [3].
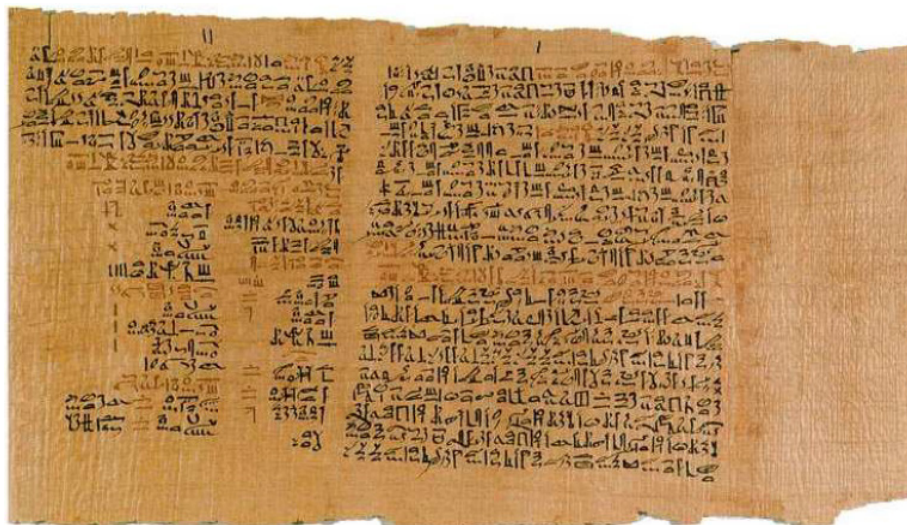
Figure 1.1: Part of the Ebers papyrus, one of the earliest known descriptions of cancer documents believed to have been written in Egypt about 1600 B.C.

According to [4], this papyrus included the first written evidence suggestive of breast cancer, which was detected by palpation. The Ebers papyrus describes large tumors of skull lesions suggestive of metastatic cancer, which have been found in skeletal remains from the Bronze age, 1900 to 1600 B.C. Stone describes in his work [5] how the ancient physician followed the same steps in the process of examination as we follow in our modern medical practice. Interrogation of the patient was the first step, followed by the classical steps of inspection, palpation of the body and the diseased organs.

Palpation is still one of the standard examination method performed in the modern diagnosis for the detection of breast, thyroid, prostate, and liver abnormalities. Palpation is used to measure swelling, detect bone fracture, find and measure the pulse, or to locate changes in the pathological state of tissue and organs. On the one hand, palpation is not very accurate, because of its poor sensitivity with respect to small and deeply located lesions as well as to its limited accuracy in terms of morphological localization of lesions.

Early detection is one of the primary requirements of successful cancer treatment especially in breast and prostate cancer. Thus, early detection through screening methods, such as mammography, is considered central to cancer surveillance programs throughout the world. In spite of the unquestionable successes, there remains an urgent need to improve both sensitivity and specificity of cancer imaging modalities. In the USA and other developed countries, cancer is responsible for about 25% of all deaths. On a yearly basis, 0.5% of the population is diagnosed with cancer, especially breast and prostate cancer, which present about 33% of all common cancer cases for females and males respectively [6, 7]. Adenocarcinoma of the prostate is the most prevalent malignant cancer and the second cause of cancer-specific death in men. Its annual incidence is approximately 185,000 in Europe [7]. Its therapy is more effective when cancer is diagnosed at an early stage, but this carcinoma is usually asymptomatic and therefore reliable diagnostic modalities are required. Accurate assessment of the local extent of the disease is fundamentally important in the selection of appropriate local treatment modalities.

When it comes to prostate cancer specifically, it is curable at an early stage. Therefore, early detection is extremely important. At an early stage the prostate cancer is mostly limited to the interior prostate capsule, which is the physical organ border that separates the organ from surrounding tissue. Once tumor cells have broken through the gland capsule, they spread throughout the body and affect other organs. A radical prostatectomy is preferred, when tumor growth is still inside the prostate capsule. Even at later stages radical prostatectomies are performed in special cases, in order to relief pain or to enable physical activities. Nowadays several types of diagnostic methods are used to detect prostate cancer using the evaluation of this area through digital rectal examination (DRE) and the use of serum prostate-specific antigen (PSA). A major tool in the diagnosis of prostate cancer is the DRE, which is using the fact that most tumors of the prostate are significantly stiffer than normal surrounding tissues.

During DRE, the prostate is palpated manually by the physician, who has to be experienced to achieve reliable diagnostic results. This method is unfortunately limited in effectiveness, because small tumors and those deep inside the prostate or not close to the rectal wall are usually not found using DRE alone. The PSA measurement provides a level of suspicion for the presence of cancer, and an overall indication of its development, but it does not give any information about the location, size and type of the tumor. Transrectal ultrasonography (TRUS) is performed by applying B-mode (brightness mode) US, which provides information about the relative ultrasonic reflectivity of tissues, and is routinely used in prostate examination. Originally hailed as a possible diagnostic modality for prostate cancer, TRUS is now known to have limited applicability for initial diagnosis. Malignant lesions in the prostate can be hypoechoic, isoechoic, or hyperechoic. Currently, TRUS offers the best available opportunity to

demonstrate prostate cancer. It is widely available, has a relatively low cost, and provides the opportunity for precise and accurate needle biopsy of the gland. However, because many prostatic tumors are both isoechoic and multifocal, TRUS has major limitations in fully demonstrating prostate cancers. Furthermore, TRUS has low echotexture specificity because many pathologic conditions may demonstrate similar appearances as hypoechoic areas in the peripheral zone of the prostate. TRUS imaging can detect approximately 2/3 of all tumors, whereas the remaining 1/3 appear isoechoic and cannot be identified as tumors [8]. Neither MRI nor CT scans can replace TRUS adequately for prostate cancer detection. However endorectal MRI permits the determination of occult extraprostatic spread in given individual cases. The gold standard remains the minimal invasive method using sextant biopsies guided by TRUS examination. This process is an invasive sampling procedure that unfortunately cannot exclude cancer for sure.

1.1.2. Value of Elasticity Imaging

Changes in tissue elasticity are related to the physiological health of the tissue. Changes in tissue stiffness may manifest as changes in tissue elasticity which may indicate pathogenic or malignant growth. A tumor is 5-28 times stiffer than the background of normal soft tissue. For instance, scirrhous carcinoma appears as extremely hard nodules in the breast [9]. In standard medical practice, tissue elasticity is qualitatively assessed by palpation. While palpation may still be the preliminary diagnostic step, its subjectivity (perception of degree of stiffness may vary from physician to another) makes results more prone to inconsistency and hence less reliable.

The elastic properties of soft tissues depend on their molecular building blocks, and on the microscopic and macroscopic structural organization of these blocks [10]. Some data on tissue elastic properties were collected by Sarvazyan et al. [11], Parker et al. [12] and Walz et al. [13]. Some of the authors' recent results on breast and prostate tissues in vitro are given in Table 1.1 and Table 1.2 [14] and visualized in Figure 1.2. These results indicate that in the normal breast fibrous tissues are stiffer than glandular tissues, which are in turn stiffer than adipose tissues. The two kinds of tumors studied show different behaviors, with the infiltrating ductal carcinomas being significantly stiffer than the ductal tumors. Some of the tissues exhibit marked non-linear changes in their stiffness behavior with applied precompressive strain, while others remain unchanged. There appear to be opportunities in differentiating breast tissues based on their stiffness values as well as their non-linear stiffness behavior. Table 1.2 also show significant differences are also evident among normal, BPH and cancerous tissues of the.

Although many researchers have proposed imaging the stiffness distribution in tissue to enhance diagnosis of cancer disease, as shown in [15], current medical practice routinely uses sophisticated diagnostic tests through magnetic resonance imaging (MRI), computed tomography (CT) and ultrasound (US) imaging, which cannot provide direct measure of tissue elasticity.
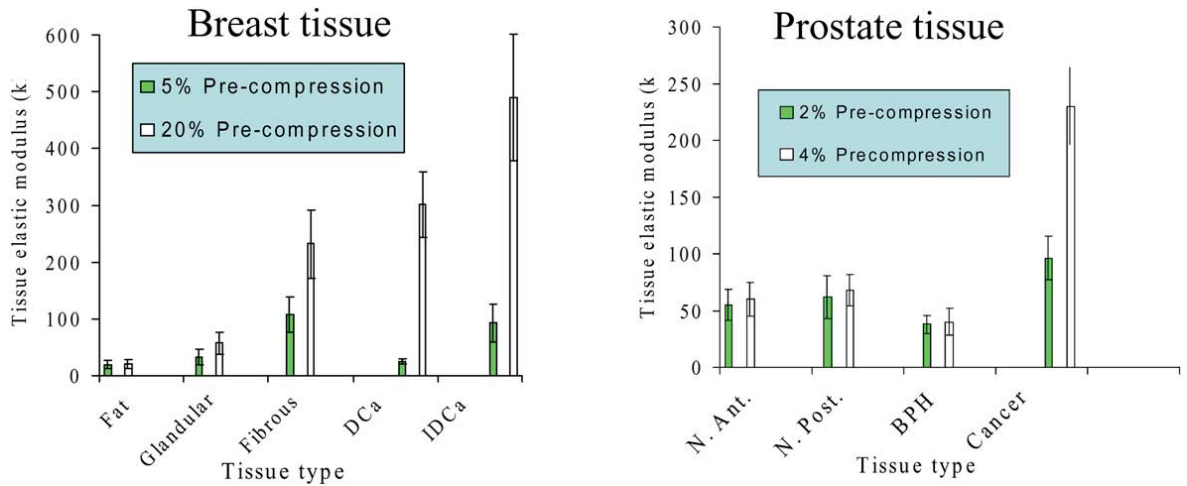
Figure 1.2: Tissue elastic moduli obtained from normal and abnormal breast and prostate tissues (DCa = ductal carcinoma, IDCa = intraductal carcinoma, N. Ant. = anterior portion of the normal prostate, N. Post. = posterior portion of the normal prostate, BPH = benign prostatic hypertrophy).

Table 1.1: Results of actual stiffness measurements (in kPa) of normal and abnormal breast tissues in vitro (20% precompression – 2% strain rate).

Tissue Type	Stiffness Modulus (kPa)
Normal Fat	20±8
Normal Glandular	48±15
Fibrous	220±88
Ductal CA	291±67
Infiltrating ductal CA	558±180

Table 1.2: Results of actual stiffness measurements (in kPa) of normal and abnormal prostate tissues in vitro (4% precompression – 8% strain rate).

Tissue Type	Stiffness Modulus (kPa)
Normal anterior	63±18
Normal posterior	70±14
BPH	36±11
CA	221±32

1.1.3. Value of elasticity imaging using Ultrasound (US Elastography)

1.1.3.1. Ultrasound in Medical Applications

Ultrasonic waves are acoustic waves with frequencies above the audible range of the human ear. Acoustic waves are merely the organized vibrations of matter that is able to support the propagation of these waves. Medical ultrasound instrumentations typically use much higher frequencies than the audible human hearing range. Most of the medical applications are achieved with ultrasound at frequencies between $1 - 10$ MHz. Most recent applications of ultrasound for examining the surface layers of skin and the walls of blood vessels have involved frequencies in the range up to 40 MHz. At even higher frequencies, acoustic microscopy can provide detailed images, based on the acoustical characteristics of tissues. The choice of the suitable frequency for certain application is a tradeoff between the combined needs of good resolution and good penetrating ability. As the frequency is increased, the wavelength of ultrasound waves gets progressively smaller, which accounts for the improved resolution capabilities of ultrasound compared to ordinary sound waves. Before the first documented use in diagnostic applications by Dussik in 1942, US was used in the field of medicine in therapy. The incident and absorbed focused waves produce heat, which can be used to decrease muscle cramps and to reduce pain. The destructive ability of high intensity ultrasound had been also recognized earlier in the 1920s. One of the most important ultrasound therapy applications is Lithotripsy, a clinical procedure whereby extracorporeal shock waves are focused onto kidney stones to fragment them into pieces small enough that they can be passed naturally [16]. The first diagnostic use of US was reported in 1949 [17]. The researchers discovered the physical characteristics of ultrasound and studied the acoustic impedance of various types of human tissue, as well as the attenuation of ultrasound energy in tissues, impedance mismatch between various tissues and related reflection coefficients, and the optimal sound wave frequency for a diagnostic instrument to achieve adequate penetration of tissues and resolution, without incurring tissue damage.

Nowadays, the use of ultrasound in the modern medical diagnosis has found a solid niche among the various methods for imaging the body. Advantages of ultrasound imaging against other imaging techniques are the following:

- The safe application at low radiated power; there is no documented hazard associated with its safe use, and no radiating or ionizing waves are used, within the range determined for medical applications compared to radiography which has a well-documented hazard, depending on the dosage required [18].
- Sonography is a non-invasive or minimal invasive method, as waves are generated entering the body and no foreign substances are needed to be injected into the body to interact with the waves. The exception is using hazardless ultrasound contrast agents, used in a few applications.
- The ability to produce real-time images to differentiate between soft tissue types; ultrasound waves interact and propagate through soft tissue and liquid, where they are partially reflected at interfaces between different soft tissues. Thus, an US scan may be more sensitive to real time variations in soft tissue type than a computed radiograph (CT) or magnetic resonance image (MRI).
- Simplicity, convenience and low cost for the patient and the physician: ultrasound imaging is a simple technique, the session takes a few minutes and

the scanning procedure itself is quite easy, so the patient mostly does not need any precautions or complicated preparations. It must be noted, however, that the advantage that ultrasound possesses in soft tissue scans is counterbalanced by the lack of penetration in bony areas or air spaces. This limits the applications of ultrasound in the skull, skeleton or in the lungs or some gastrointestinal areas.

1.1.3.2. Elasticity Imaging using US

As stated before, a small sized lesion or one that is embedded deep inside the tissue is hard to detect by palpation. This necessitates painful, invasive biopsies. Among other medical imaging modalities, acoustic imaging techniques are most well suited for screening and routine diagnostic examinations of tissues that have strong sound contrast properties. US B-mode imaging has been used extensively in clinical applications ranging from obstetrics and gynecology to abdominal, cardiac and cancer imaging. Ultrasonic imaging works on the principle of acoustic reflectivity and regions with good contrast in echogenicity are detected well in the US image. However, two regions with the same echogenicity may have different stiffness contrast. For instance, tumors in the breast or prostate are much stiffer than the embedding tissue and scirrhosis of the liver increases the stiffness of the whole tissue, yet the tissues may appear normal in US scans. In other words, elasticity and echogenicity are uncorrelated and traditional B-mode imaging may not detect elastic contrast. Elastography can provide new information about areas opaque to sonography due to acoustic shadowing, areas with hard lesions in a soft background and isoechoec regions that are invisible to sonography.

This is the primary motivation behind elasticity imaging using US (elastography) - to provide new information on tissue stiffness that can be complemented with echo contrast information available from US imaging in order to have a more clinically useful, specific and accurate diagnostic report. An example for that is the image shown in Figure 1.3. Much research effort has been directed toward US elastography realization since its inception [19]. Though still a relatively novel technique in the area of imaging, elastography has evolved from a research bench to a diagnostic tool capable of providing information for improved diagnosis. Today, elastography is being considered as a potential replacement for painful biopsies.

(a)   (b)
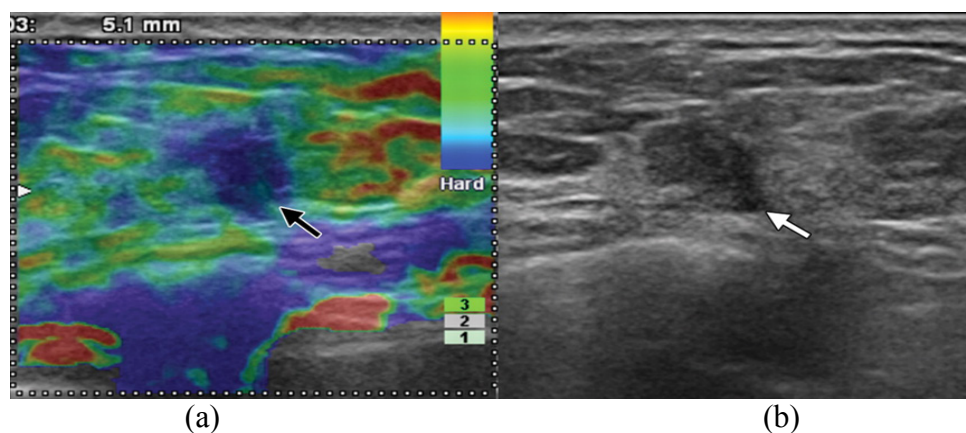
Figure 1.3: (a) US image fused with elastography strain color map. (b) US image alone (Isoechoec stiff nodule: suggesting invasive ductal CA (Hitachi Medical, Tokyo, Japan))

1.2. **Organization of the thesis**

In Chapter 2, we review the basic principles underlying elastography. Then, we introduce steps of standard gated 1D crosscorrelation elastography and the impact each step has on signal-to-noise ratio, contrast-to-noise ratio and computation time of elastogram. This basic 1D elastography technique suffers from some issues. So, in Chapter 3, we propose a modified version of one of the 2D block matching algorithms which make it more oriented to work with US data. We also utilize the inherent continuity in the imaged tissue to make an optimized version of the previously modified algorithm. The effects of imposing more constraints on the optimized algorithm are studied. Also, we show the effects of the block size and postprocessing on the estimation output. In the end, we present our conclusions and potential future work in Chapter 4.

Chapter 2 : 1D Crosscorrelation Elastography

2.1. Elastography Principles

Elasticity imaging is typically done by processing the ultrasound RF data to estimate tissue displacements induced by external stimuli or internal motion. Quasi static compressions are used to excite the tissue externally in the direction of ultrasonic radiation [19, 20]. Alternatively, internal stimuli from inherent activity of the organs such as cardiovascular activity of the heart or blood flow can be used to produce elastographic signal [2]. The resultant speckle patterns contain information about internal displacement of the individual tissue components. Coherent echoes before and after compression, in the direction of applied strain, are then divided into overlapping windows in the time domain. The delay between these windows is tracked using speckle tracking methods such as cross-correlation [21]. Assuming the velocity of sound in the tissue is constant, the delay in time domain can be converted to longitudinal displacement between the adjacent windows. The resultant strain distribution can be obtained by computing the gradient of displacement. The resultant strain images are referred to as 'axial strain elastograms'. Each pixel in an elastogram denotes the amount of strain $\hat{\epsilon}$ experienced by the tissue during compression, given by

$$\hat{\epsilon} = \frac{\hat{\tau}_1 - \hat{\tau}_2}{\Delta t}, \qquad\qquad 2.(1)$$

where $\hat{\tau}_1$ and $\hat{\tau}_2$ denote the axial displacement estimates in windows 1 and 2 respectively separated by a distance of Δt. The applied compression is typically in the range of 0.5-2% of tissue depth. The echoes are traced during or after the time that the tissue undergoes deformation caused by the excitation.

A schematic of a typical elastography experiment is shown in Figure 2.1.The basic assumption made in tissue elastography is that the tissue behaves as an elastic, incompressible solid while in reality, it is viscoelastic. The assumption implies that there is a linear relationship between tissue stress and strain, the tissue is isotropic, there is no hysteresis, stress relaxation or creep. This assumption was justified in quasi-static elastography experiments by Ophir et al [19].

In this simplistic model, the tissue is modeled as a cascaded spring with a rigid base as shown in Figure 2.1. This is the 1D spring model of a layered tissue. In Figure 2.1 (a), a transducer-compressor assembly is placed on the surface of the tissue, ultrasonic pulses are fired and the echo response of the uncompressed tissue is recorded. In Figure 2.1 (b), the tissue is uniformly compressed under quasi-static controlled conditions, and the echo response of the compressed tissue is recorded. In the case of uniaxial tensile stress in a cascaded spring assembly, the force in all the spring segments is the same. Consequently, the mathematical model of tissue is simplified and the equation of quasi-static uniaxial stress reduces to the Hookean equation [2]

$$F_0 = K\Delta x, \qquad\qquad 2.(2)$$

where K is the local stiffness of the tissue, F_0 is the applied stress and Δx is the resulting local change in displacement.

The equivalent equation in this model for the continuous case becomes

$$Y = \frac{F_0}{\Delta x}.$$ 2.(3)

Plugging 2.(2) into 2.(3), we get

$$Y \propto K.$$ 2.(4)
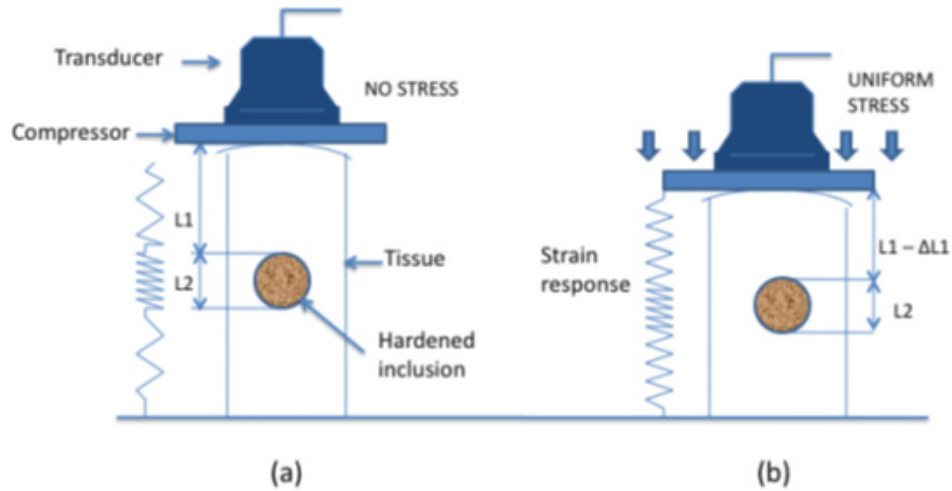
Figure 2.1: Schematic demonstrating the principle of elastography (a) precompression (b) postcompression.

From 2.(4) we see that in the cascaded spring model, stiffness constant for a tissue region can be quantified by Young's Modulus. Experiments have established that the larger the area of the compressor, the more uniform the longitudinal stress fields and consequently more uniform strain fields.

Figure 2.2 shows the strain profile of the set up in Figure 2.1. The level of applied strain is kept small to maintain the Hookean equation in the linear range of stress-strain relationship.
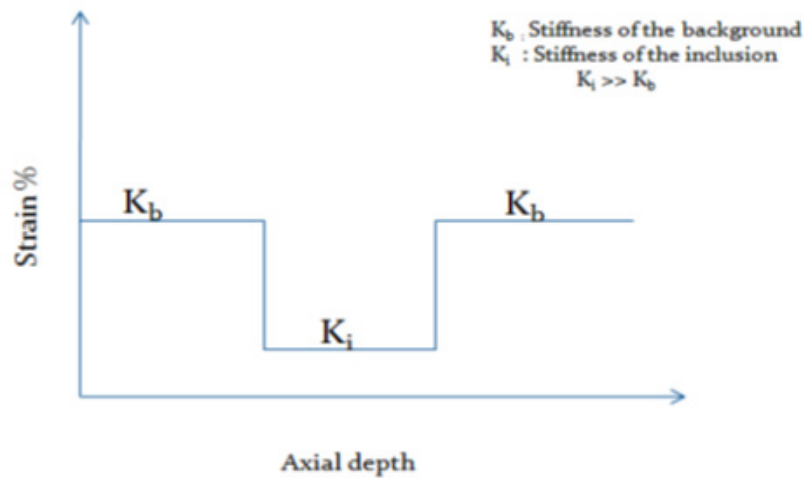
Figure 2.2: Ideal strain profile of a target with stiffer inclusion.

Strain is a 3D tensor, strain elastography is fundamentally a three dimensional problem with displacement in the axial, lateral and elevational directions. Though recent work on lateral and elevational strain estimation [22, 23] suggest that it is possible to generate lateral and elevational elastograms, in this study we will focus only on axial displacement and axial strain estimation. The concepts and approaches developed in this work, however, can be easily extended to lateral and elevational strain elastography.

2.2. Steps of 1D CC elastography

The general block diagram of any static US elastography is shown in Figure 2.3.
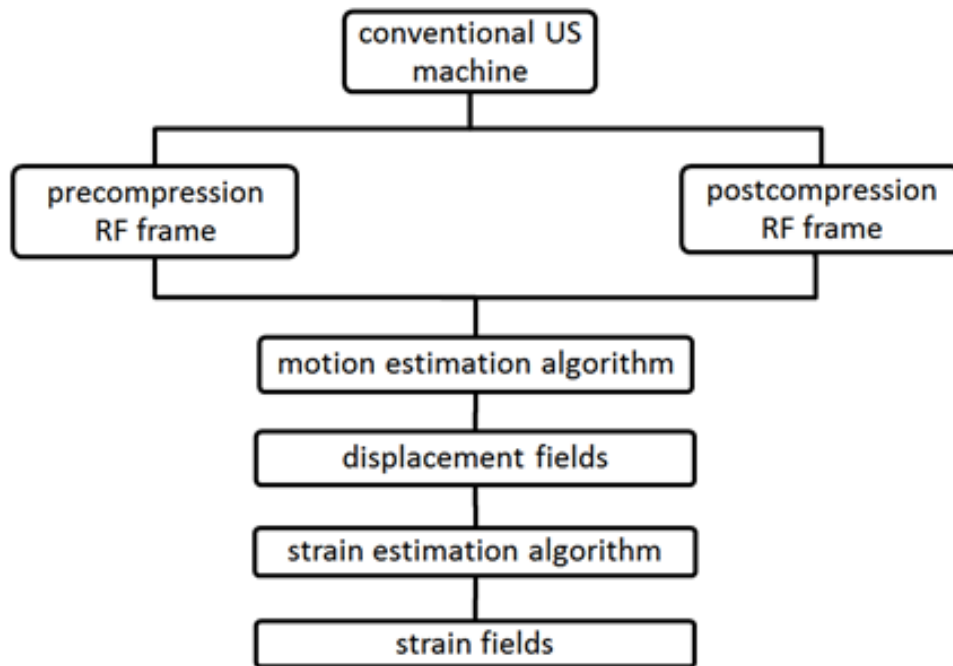
Figure 2.3: Elastography general block diagram.

2.2.1. Data Acquisition

2.2.1.1. US Imaging System and Principles

Most of the modern ultrasound medical diagnostic machines are based on the pulse-echo technique as shown in Figure 2.4. In this technique, a short pulse of ultrasound is transmitted by a transducer into the tissue regions being investigated. Reflections from each of the various tissue boundaries due to changes in the acoustical impedance are received back at the transducer, and the total transit time from initial pulse transmission to reception of the echo is proportional to the depth of the boundary. As the transmitted pulse progresses through the tissue of impedance Z_1 toward the interface at depth l_1 with the organ of impedance Z_2, essentially no reflection takes place as long as the impedance Z_1 is more or less homogeneous.

The first significant signal received is the reflection from the anterior organ boundary at the depth point l_1 after the echo has returned to the transducer. Therefore, the received echoes are only depending on areas of different echogenity and can be reconstructed along the line of pulse propagation. The time from the initial pulse emission to the time of arrival of the first boundary echo can be calculated as

$$t_1 = \frac{l_1}{c/2}.$$

2.(5)

The pulse direction of propagation is called the axial direction. Displaying this single line information according to the amplitude of the reflected wave is defined as the A-mode3 display, see Figure 2.4.
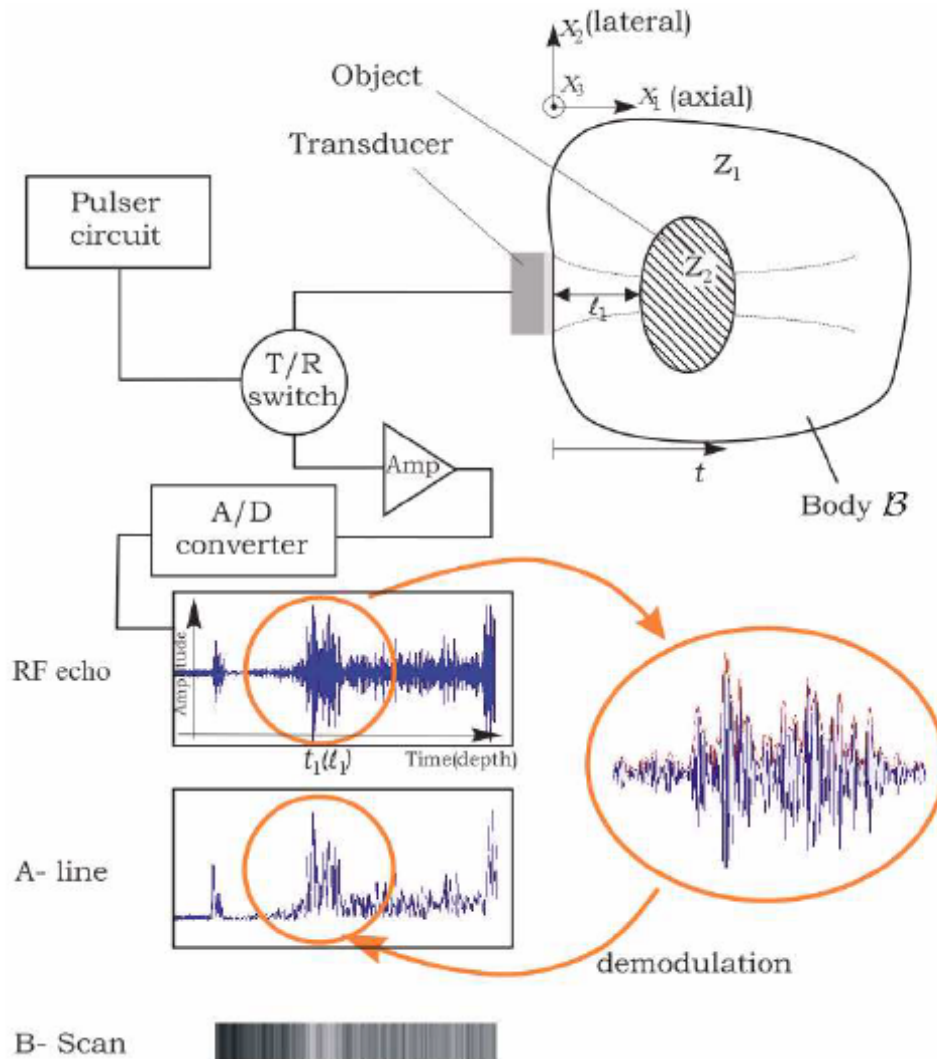
Figure 2.4: Elements of a simplified ultrasound pulse echo instrument. The received RF echo signals are presented on the vertical axis, where the horizontal axis defines the time of flight which is converted to equivalent depth of penetration. RF signals are then demodulated representing the A-mode signals and the B-mode image lines. The envelope of the echo signals is seen to the right, which yields 1D-information about the tissue.

In order to develop the 2D information image of tissue echogenity distribution, the ultrasonic pulse must be sent along transferred lines (A-lines) within one axis. The

ultrasound beam is then translated to the perpendicular axis, which is called lateral direction. From the demodulated signals (by methods like Hilbert transform) a gray scale plane image of the tissue is generated, where the logarithmical compressed envelope amplitude of the received echoes represents the image brightness. This grey colored image defines the conventional B-scan (B-mode image). Figure 2.4 shows elements of an A-mode pulse echo instrument and the demodulation from RF echo signals to A-lines or to B-scans.

As seen from Eq. 2.(5), to relate the time of flight to the depth of the tissue boundaries, the phase velocities in each medium have to be known. In the meantime, all ultrasound scanners assume that the tissue phase velocity have a value partway between those of water and muscle, that is $c = 1540$ m/s. The emission of the beam is mainly controlled electronically.

Basically there are three different kinds of images acquired by multi-element array transducers, i.e. linear, convex, and phased as shown in Figure 2.5. When imaging with a linear array, each A-line is constructed with a different sub-aperture composed of a certain number of elements. The sub-aperture is translated over a region of interest. This enables to construct a rectangular 2D B-mode image. A larger area can be scanned with a smaller array if the elements are placed on a convex surface. A sector scan is then obtained. This is useful for imaging the abdomen for example. The principle of translating the active sub-aperture all over the probe is the same as for the linear array. But in some cases this can still be insufficient. For imaging the heart for example, smaller arrays are used in order to steer between the ribs; those arrays are called phased arrays. Phased arrays enable to have a large field of view using a small array. In phased arrays all elements of the array are used in transmit and receive. The direction of the beam is controlled by electronically delaying the signals emitted and/or received by the elements. The image can be acquired through a small window and the beam rapidly swept over the region of interest. Recently more advanced transducers have been developed. The number of elements is always increasing, and two dimensional arrays are nowadays standard products. For both convex and phased array transducers, a coordinate transformation is needed to interpolate (typically bilinear) the data accurately on the display depending on the display resolution. Figure 2.6 shows an example of scan conversion from polar to Cartesian coordinate typical of ultrasound systems.

In all different kinds of arrays, beamforming can be used in emit and receive in order to improve contrast, depth of field or more generally to control the characteristics of the ultrasound image. A single focus can be used in transmit, and the user can select the depth of the focus. The reflected and scattered field is then received by the transducer again and amplified by the time gain compensation (TGC) amplifier. This compensates for the loss in amplitude due to the attenuation experienced during propagation of the sound field in the tissue. The US system components are shown in details in Figure 2.7.
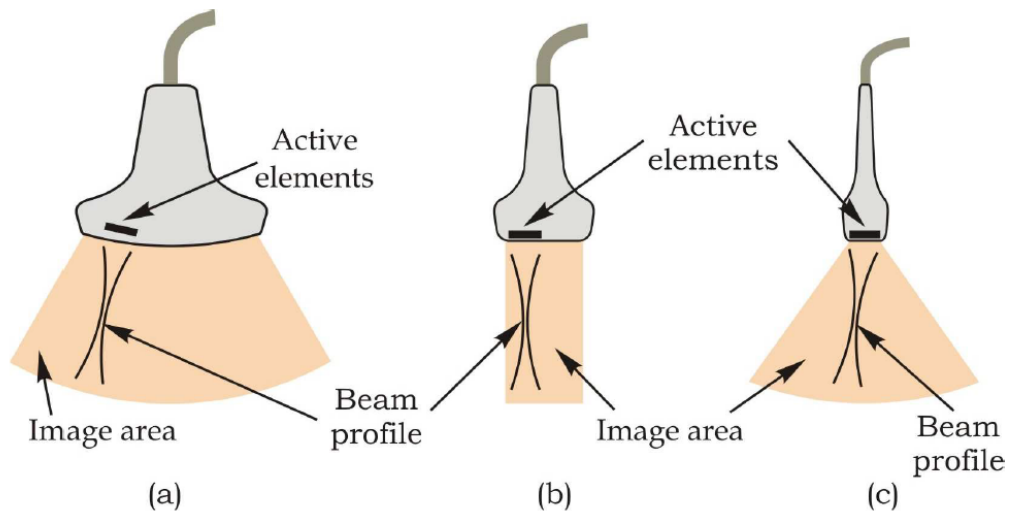
Figure 2.5: (a) Convex array transducer for obtaining a polar cross-sectional image. (b) Linear array transducer for obtaining a rectangular cross-sectional image. (c) Phased array transducer for obtaining a polar cross-sectional image using a transducer with a small aperture.
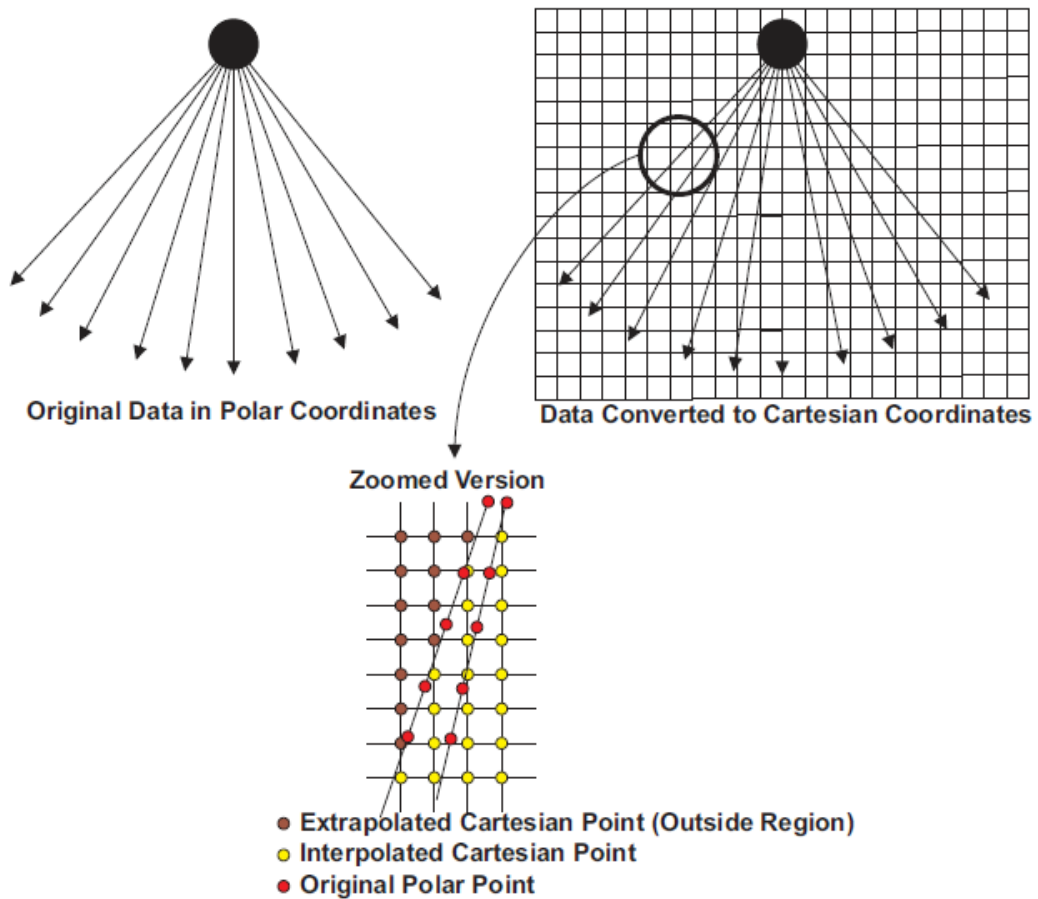
Figure 2.6: Scan conversion process.
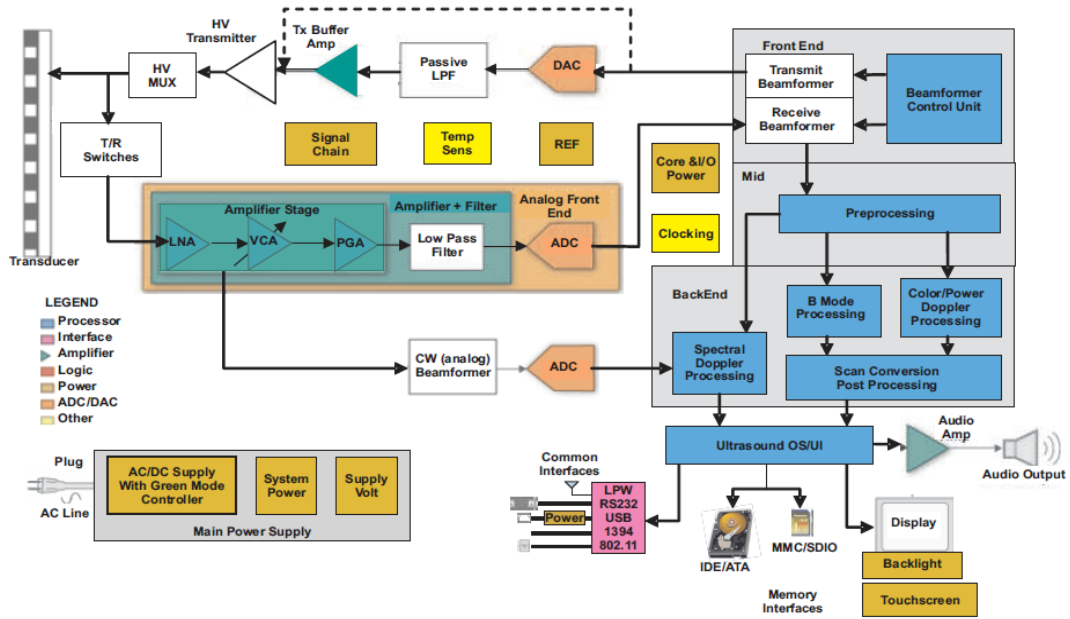
Figure 2.7: Detailed US system with its components.

2.2.1.1. RF acquisition pre and postcompression

In our experiment, a set of digitized RF echo data is obtained after placing a rectilinear array ultrasound transducer on the surface of the target tissue (the general idea is represented in Figure 2.8). As stated before, the scanner usually operates between 1MHz and 20MHz in order to optimize for resolution and penetration. The surface is then slightly compressed with the transducer or with a transducer-compressor assembly, and another set of digitized and compressed RF echo data is obtained from the same area of interest. The pre- and post-compression signals are independently stationary but jointly non-stationary and this should be taken into account while processing these signals as will be presented later.

For testing purpose, we used the same phantom RF data in Rivaz et al. (applied compression ≈ 2%) which is a CIRS elastography phantom (CIRS, Norfolk, VA) [24], [25]. The B-mode images for pre and postcompression frames are shown in Figure 2.9. The size of both frames is 1700*508 samples. The semicircular stiff lesion can be fairly seen due to being isoechoec with the surrounding tissue. An ROI around the lesion is delineated by white rectangles in Figure 2.9(a,b) and shown separately in Figure 2.9(c,d). The height of the ROI is bigger than the width to include wide range of axial TDE values. The size of the ROI is 1301*188 samples[1].

---

[1] In some discussions, we test the discussed algorithm on the full data. In others, we will test the algorithm on the ROI.
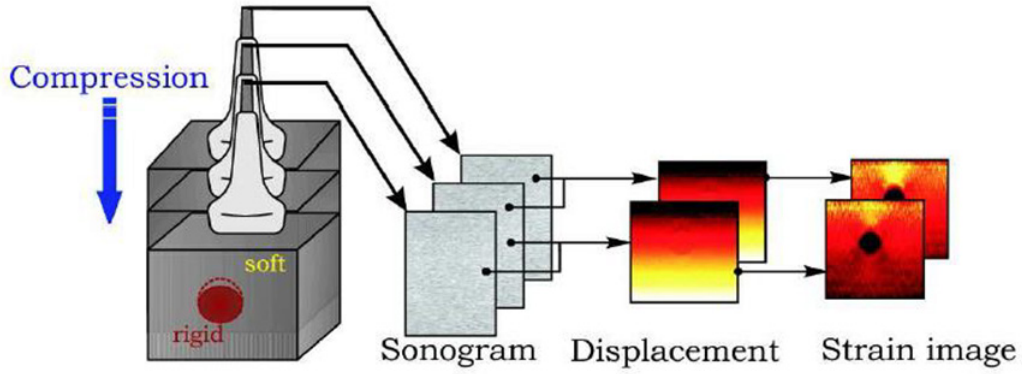
Figure 2.8: US RF data acquisition pre and postcompression

2.2.1. Time Delay Estimation for Axial Displacement

A time delay between the pre- and post-compressed echo signals arise from the spatial shift of the compressed tissue. Assuming the speed of sound in the soft tissue is constant, the spatial shift is proportional to the time shift. Hence, delay estimation in time domain is equivalent to displacement estimation in spatial domain. Figure 2.10 shows an example for time delay between pre- and post-compressed A lines in elastography. The quality of elastograms depends directly on the ability to estimate time delay accurately [21]. The presence of noise in the post-compressed echo signal induced by mechanical compression, imposes a limit on the accuracy achievable in time delay estimation [26]. Time-delay estimation (TDE) can be performed using several methods [27], [28]. Available estimators are Sum of Absolute Difference (SAD), Mean Square Error (MSE), Cross-Correlation based tracking algorithms, Fourier-based phase-tracking techniques [29], etc. Cross-correlation techniques are appropriate for quasi-static applications.

In our implementation, local displacements are estimated by measuring time shifts in short time histories. The resultant displacement between the gated pre- compression and post-compression echo signal segments is estimated as the location of the peak of cross-correlation between the pre- and post-compression signals in that window of observation. Given the expression of the cross-correlation as

$$\hat{r}_{xy}[\tau] = \frac{1}{N} \sum_{i=1}^{N} (y[i]x[i+\tau]), \qquad 2.(6)$$

where x is the pre-compressed signal, y is the post-compressed signal, $\hat{r}_{xy}$ is the estimated cross-correlation between pre- and post-compression signals, τ is the time delay between pre- and post-compression and N is the number of sample points in a window. The estimated displacement is τ at which $\hat{r}_{xy}$ is maximum. The cross correlation window is translated for all depths. Each window of observation is shifted by a pre-defined linear distance till the last window of observation is reached for all depths of observation.
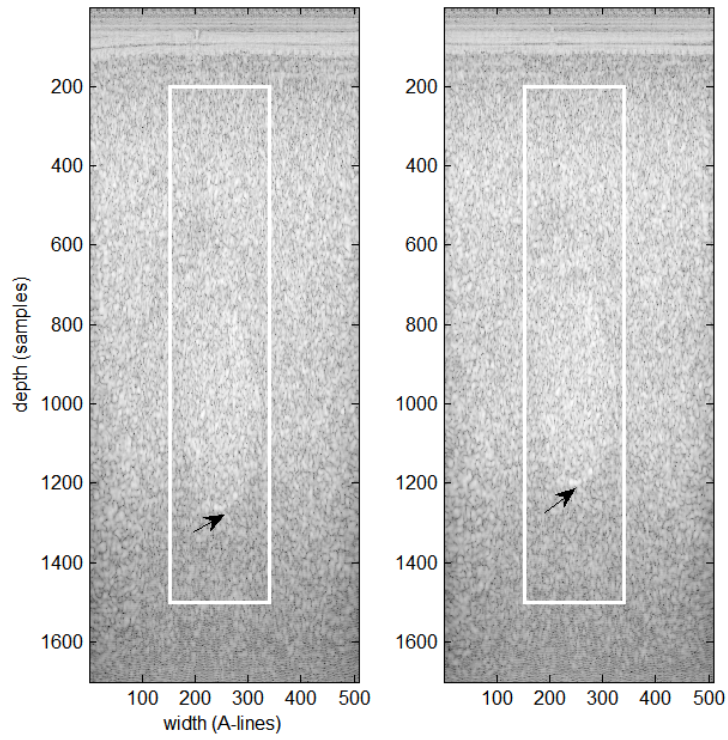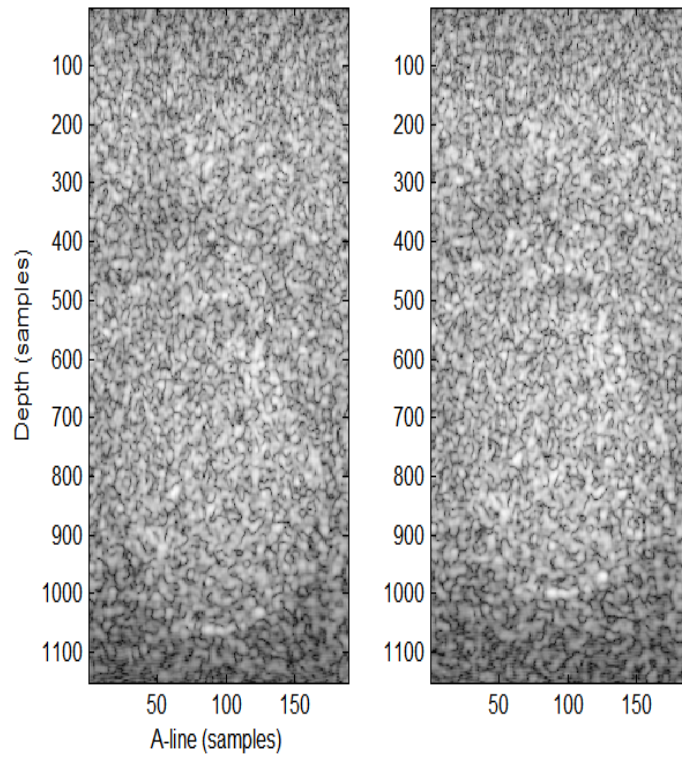
Figure 2.9: Phantom B-mode images. (a) Precompression. (b) Postcompression. (c) Precompression (after cropping). (d) Postcompression (after cropping).

16
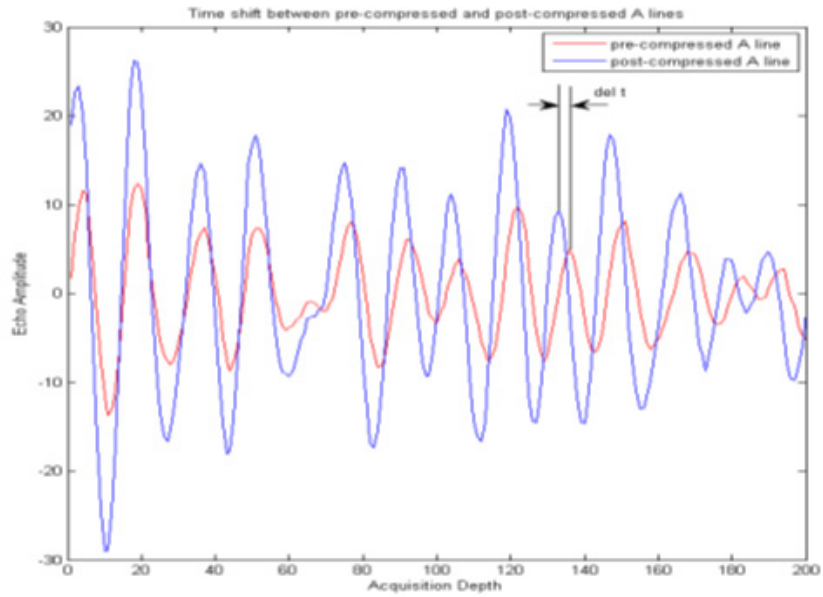
Figure 2.10: An example of time delay between pre & postcompression RF lines.

The resulting displacement field of applying gated 1D CC to our phantom data without any pre or postprocessing (window size = 3mm with 80% overlap) is shown in Figure 2.11(a). The ideal displacement field (by numerical finite element (FE) simulation) generated in [30] is shown also in Figure 2.11(b) for qualitative comparison (quantitative measures will be shown later). It can be seen that basic 1D gated CC processing alone is not enough to get appropriate axial TDE fields and further pre and postprocessing is required.

(a)

(b)
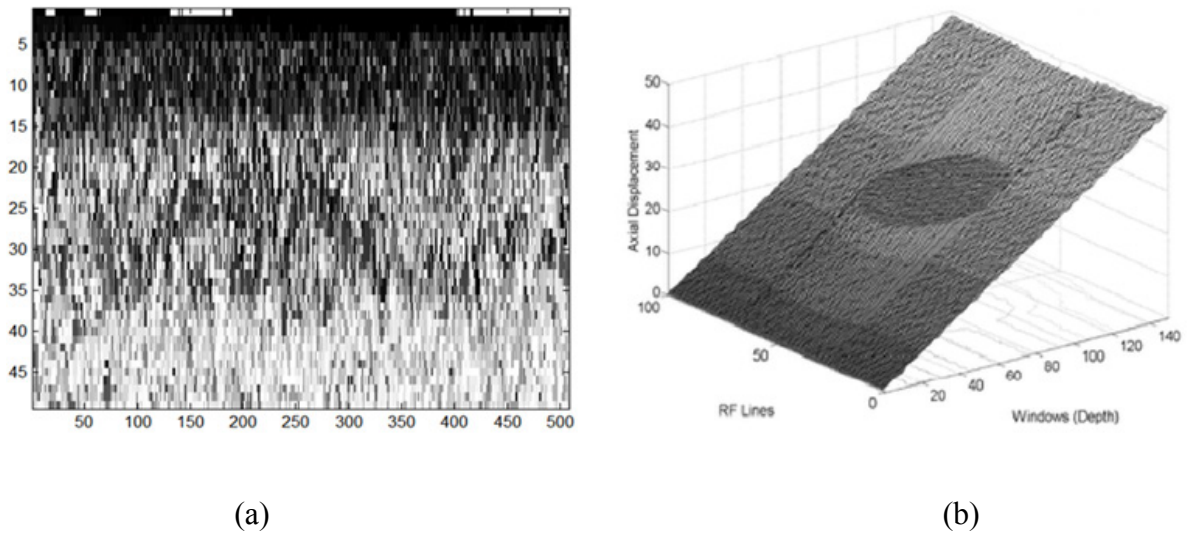
Figure 2.11: (a) Displacement field by basic 1D CC TDE. (b) Ideal displacement field (by simulations).

2.2.2. Preprocessing (before 1D CC)

The quality of time delay estimation depends on the extent of similarities between the pre-compressed and post-compressed echoes. In elastography, the amount of similarity is reduced due to the parameters involved in data acquisition. When mechanically compressed, the tissue scatterer spacing is reduced and the resultant echoes reflected from physically compressed acoustic scatterers will be distorted [2]. Note that this distortion also constitutes the actual strain that is displayed in the elastograms. Due to this distortion, crosscorrelation between an uncompressed echo and another temporally compressed echo will be poor since the compressed echo is no longer a delayed replica of the uncompressed echo. This is referred to as decorrelation noise. To partially correct this, the post compressed echo is usually temporally stretched prior to CC computation. This step alleviates some of the axial decorrelation and improves the SNR_e [31]. Essentially, the stretching realigns the scatterers within the correlation window. An appropriate stretching factor will make the post compression echo a closer replica of the pre-compression echo and the cross correlation will improve considerably. The choice of stretching factor is based on the amount of applied strain. This is a constraint of this method - apriori knowledge of the applied strain is required. Other methods like logarithmic amplitude compression and 1-bit quantization do not require prior knowledge of the applied strain [32].

Temporal stretching is usually implemented using resampling (linear interpolation). That is, stretching a signal $s(t)$ by a factor of a means resampling the signal to obtain $s(\frac{t}{a})$. For example, if the precompression signal is compressed by 1%, then the stretching factor a for the postcompression signal should be 0.99 [33]. Stretching can be done either globally, where all windows are stretched equally, or adaptively, where windows are stretched by different factors [34]. Adaptive stretching is iterative and computationally intensive. For small strains (<2%), global stretching is usually acceptable for signal conditioning. However, it is important to note that global stretching works optimally when the target is homogeneous. When the target is non-homogeneous (our case), stretching the target globally with a factor in the order of the applied strain would imply over-stretching low-strain areas inside the inclusion or under-stretching high strain areas in the background. This has the potential to corrupt the strain image. Hence a global stretch factor should be chosen carefully. Figure 2.12 shows a practical simulation example to illustrate the effect of stretching on non-homogeneous targets. The result of applying temporal stretching (stretch factor = applied strain) in our study (where applied strain = 6%) is shown in Figure 2.13.
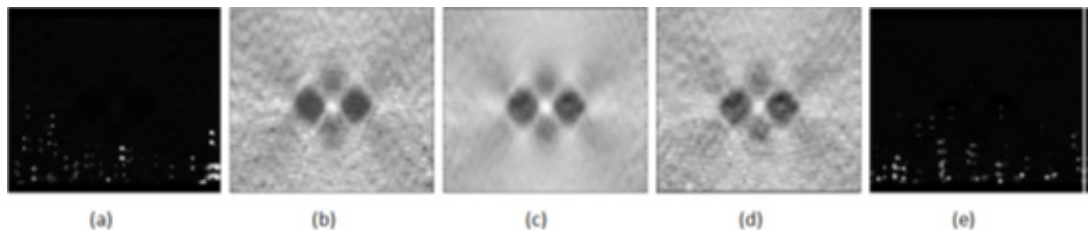
Figure 2.12: Effect of varying stretch factor on CC result of simulation (FE) phantom. (a) 0% stretch (b) 1% stretch (c) 2% stretch (d) 3% stretch (e) 4% stretch.
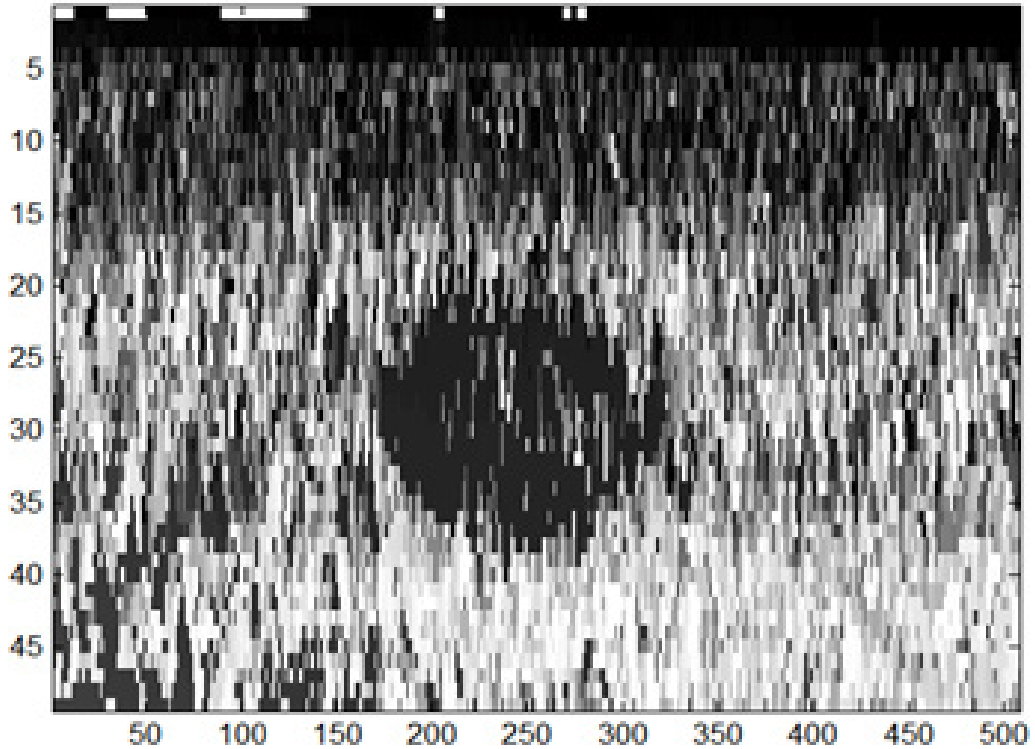
Figure 2.13: TDE with temporal stretching (global) of postcompression RF line.

2.2.3.   Postprocessing

2.2.3.1.   Subsample TDE

In the CC approach, the time delay obtained between the pre-compressed and the post-compressed A-lines is an integral multiple of the pixel sample interval. This is the time quantization error due to digitization of RF data. In elastography where the applied strain is in the range of 0.5%-2%, the actual time delay is much smaller than the sample interval. To estimate sub-sample displacement values, it is required to interpolate between samples [21]. One method to perform interpolation is by oversampling. However, this method is computationally inefficient since it increases the length of the entire cc function while we need finer resolution only near the peak, and hence is not used here. An efficient interpolator used instead is parabolic interpolator around the estimated peak.

The parabolic interpolation method that uses 3 points - the estimated peak and its left and right neighbor points to compute the quadratic order polynomial passing through them [35]. However, parabolic interpolation is a biased estimator of the true location of the peak because it imposes a predetermined analytical shape on the estimate. The bias error is minimum when the estimated peak coincides with the true peak, or the true peak is half-way between the two samples. The bias error is maximum when the true peak is about $0.25T_s$ distance from the estimated peak (T_s is the sampling period). Reconstructive (sinc) interpolation can also be used. It is an unbiased estimator but computationally expensive [35].

The result of adding 3-point parabolic interpolation to latest result in Figure 2.13 is shown in Figure 2.14.
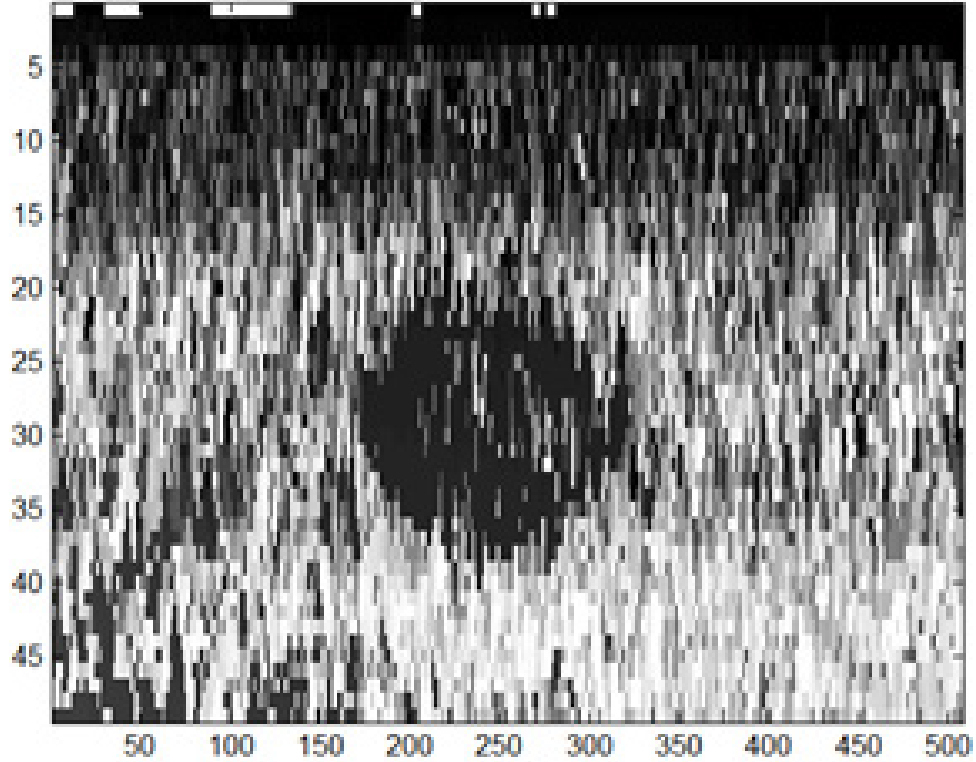
Figure 2.14: TDE after adding subsample 3-point parabolic interpolation.

2.2.3.2. 2D continuity check (median filtration)

Median filtering is an image engineering technique of noise-smoothing. Its edge preserving feature makes it more useful than low-frequency linear filters in medical imaging applications. It is effective for smoothing salt-pepper noise and false peaks. Median filtering is also computationally more accurate, because it relies on numerical comparisons and is not prone to overflow or rounding errors which may occur in linear filtering implementations.

The result of adding median filtration to the last result is shown in Figure 2.15.

2.2.4. Strain Estimation

2.2.4.1. Spatial gradient

Axial strain is the spatial derivative of the displacement along the axial axis. Being a differential measurement, it is more visually comprehensible than the TDE field which is a measurement relative to the probe (consequently, TDE does not express true physical displacement of scatterer – see Figure 2.11). It is estimated by computing the local gradient of displacement over adjacent overlapping windows. The axial tissue strain ϵ estimated from two adjacent TDEs τ_2 and τ_1 separated by an interval Δt is

$$\epsilon = \frac{\tau_2 - \tau_1}{\Delta t}. \qquad\qquad 2.(7)$$

20
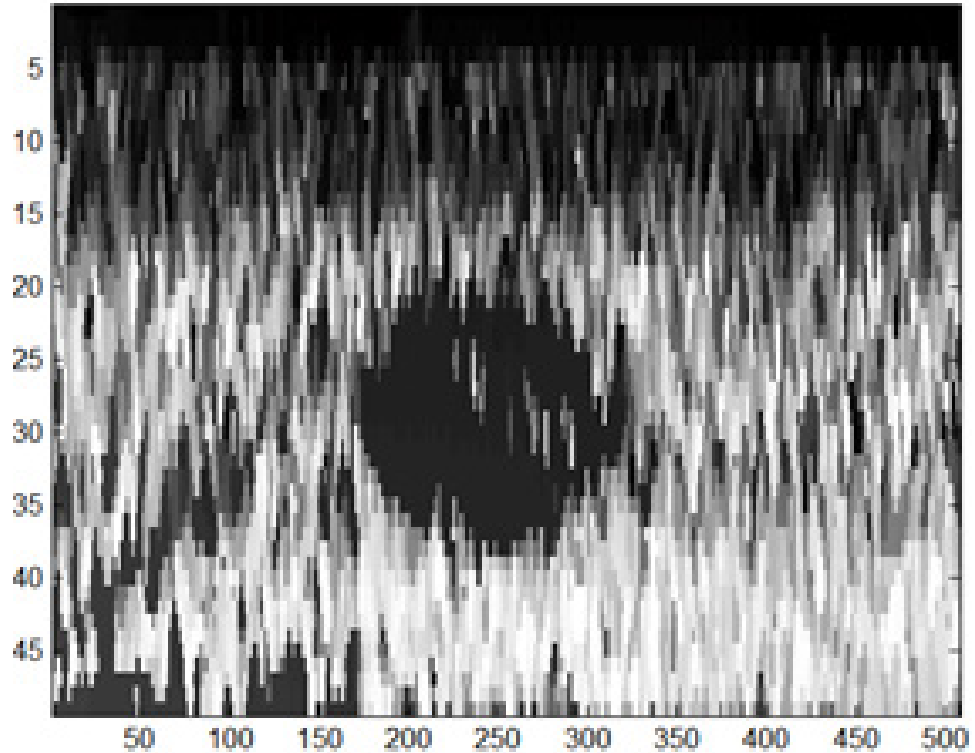
Figure 2.15: TDE after adding median filtration to remove false estimates.

High window overlaps generate more pixels in the elastogram but also introduces large noise. This degrades the $SNRe$ of the strain estimate, rendering it less than useful for detailed diagnosis [36].

2.2.4.2. Least-Squares strain estimator

Another strain estimator used instead of direct spatial derivation is a linear regression-based estimator called Least-squares strain estimator (LSQSE) [36]. In this method, each RF line is first differentiated independently: for each sample i, a line is fitted to the displacement estimates in a window of length $2k + 1$ around i (i.e. to the samples $i - k$ to $i + k$). The slope of the line is calculated as the strain measurement at i, ϵ_i. The center of the window is then moved to $i + 1$ along the axial direction and the strain value ϵ_{i+1} is calculated similarly. This estimator is reported to decrease noise in resultant strain field.

We applied LSQSE in our study to the resultant TDE field in Figure 2.15 to generate the axial strain field in Figure 2.16. Ideally, the strain field should have two values, one for the background and lower one for the stiffer target according to Figure 2.2.
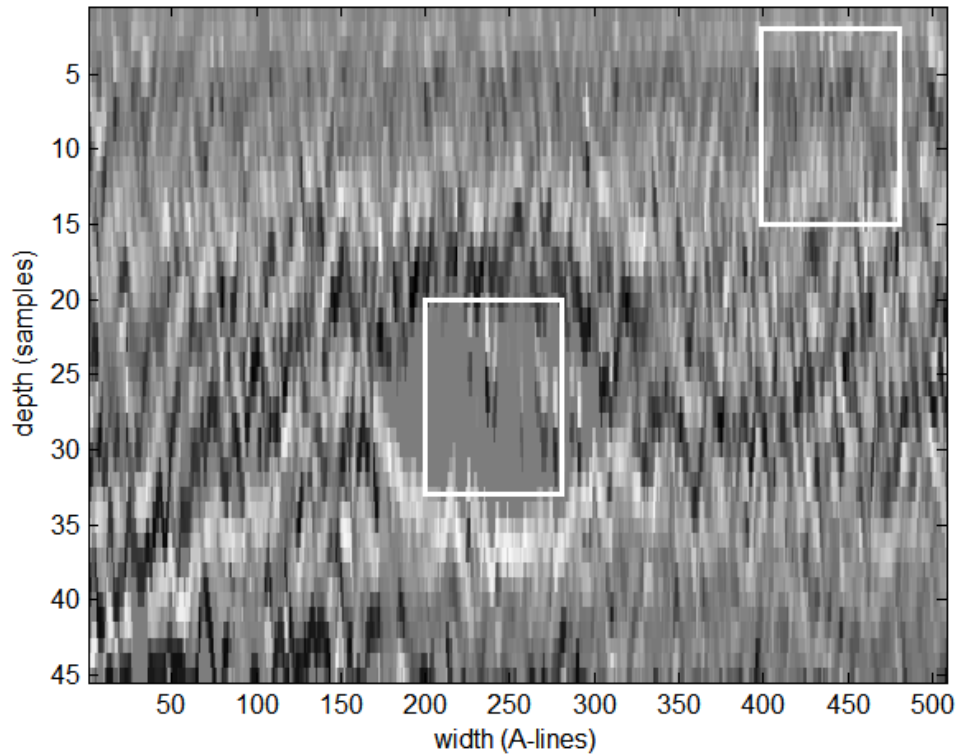
Figure 2.16: Axial strain field by applying LSQSE on TDE field in Figure 2.15.

2.3. Quality and Performance Analysis

2.3.1. Factors affecting elastographic quality

The elastographic performance is mainly affected by the following groups of parameters [1]:

2.3.1.1. US parameters

These are factors related to acquisition of US data, like transducer center frequency, f_c, bandwidth, BW, sonographic SNR, sampling frequency, f_s.

2.3.1.2. DSP parameters

These are factors related to processing US data to generate elastograms, like the length of the CC window and the shift between two consecutive CC windows.

2.3.1.3. Mechanical artefacts

Strain in the tissue depends not only on the modulus distribution in the tissue but also on boundary conditions, both internal and external. These can include stress concentrations and dilutions and target hardening artefacts [2]. Unlike other factors, mechanical artefacts represent true variations in strain; other artefacts generally hinder

an accurate depiction of the strain in the tissue. The mechanical artefacts may sometimes be beneficial and facilitate diagnosis by highlighting the targets.

These three sets of parameters are somehow interdependent and need to be in agreement with each other for optimal performance. For instance, the window length, a DSP parameter, needs to be a function of the ultrasonic wavelength, an acoustic parameter. Any change in the input parameters should be accompanied by adjusting the interdependent parameters. When the applied strain is increased, the stretch factor by which to reduce the decorrelation noise has to be increased in order to retain the quality of the elastograms. Another example, the elastographic resolution improves with increasing window overlaps. However, the upper bound of achievable resolution is defined by the bandwidth of the transducer [37].

2.3.2. Quality and performance metrics

We chose two unitless measures used extensively in elastography for quantitative assessment. That is the elastographic signal-to-noise ratio (SNR_e) and contrast-to-noise ratio (CNR_e) defined by the following equation:

$$SNR_e = \frac{\bar{s}_b}{\sigma_b}, \qquad\qquad CNR_e = \sqrt{\frac{2(\bar{s}_b - \bar{s}_t)^2}{\sigma_b{}^2 + \sigma_t{}^2}}, \qquad\qquad 2.(8)$$

where $\bar{s}_b$ and σ_b are the spatial average and standard deviation of the strain field in a theoretically homogeneous strain window (typically background) and $\bar{s}_t$ and σ_t are the spatial average and standard deviation of the strain field in the target window (circular inclusion). The $SNRe$ of a TDE and strain fields of a FE simulation is ∞ because in this ideal case no variations occur in the homogenous window (consequently $\sigma_b = 0$). Variations (artefacts) are introduced by the imaging system. The advantage of using $CNRe$ as a quantitative measure of contrast is that it is not affected by output screen variations between different setups such as brightness, contrast or gamma correction [38].

2.3.3. Quantitative assessment of phases of 1D CC elastography

All the discussed steps of the 1D gated CC strain estimation were tested on full RF frames (1700*508 RF samples). The SNR_e, CNR_e and runtime[2] of the TDE block (t_{TDE}) for TDE and strain fields in 2.2 are shown in Table 2.1(The background and target measurement widows are delineated by white rectangles in Figure 2.16).

Table 2.1: Quantitative assessment of TDE fields in 2.2.

TDE method	Basic TDE (gated 1D CC)	+temporal stretching	+parabolic interpolation	+median filtration
SNR_e	0.34	0.36	0.37	0.51
CNR_e	0.15	0.47	0.47	0.61
t_{TDE} (s)	88.1	90.2349	93.4	93.9

---

[2] All algorithms are implemented in MATLAB 2012a (Mathworks Inc., MA, USA) and tested on a 2.0 GHz Intel processor.

2.4. **Disadvantages of 1D CC Techniques**

The ultimate goal of elastography is to provide accurate information about the health of tissues that will enable detection of disease at real-time and aid in fast and objective diagnostic decision making. As shown before, the first trial of basic elastography was based on estimation of displacement between a pair of RF signals which can be accomplished using crosscorrelation techniques. Standard gated 1D CC displacement estimators introduced by Ophir [19] have some disadvantages. They cannot operate well under high applied strain ratios (>2%) due to off-axis decorrelation (moving of scatterers in the lateral & elevation directions) which cannot be solved using temporal stretching techniques (global or local iterative) [38]. Also, 1D CC techniques do not utilize smoothness conditions, which are inherent tissue property, in their operation. This leads to redundant searches for successive RF segments and occurrence of false peaks when large search windows are used. 1D CC techniques are also computationally expensive. Their asymptotic performance of $O(n^2 n_w \log_2(n_w))$, (where n is the size of the input data and n_w is the size of the correlation window) when operated on a pair of 1D RF data makes it challenging to employ them for real time processing on standard hardware [39]. Consequently, dense (pixel-order resolution) motion fields cannot be generated by 1D CC techniques.

Chapter 3 : 2D Block Matching Elastography

It can be noticed that the TDE problem in elastography is similar to the motion estimation phase in video compression domain (e.g. MPEG compression). Although some differences exist between the natures of the ultrasonic image and the photographic image (see Table 3.1) [40], block matching algorithms (BMAs), used with photographic images, can be used with US radio frequency frames to generate displacement fields.

Table 3.1: Comparison of photographic image and US image motion estimation [40].

Image Type	Photographic Image	US Image
Image capture	Camera	Ultrasound scanner
Image plane	Perspective projection of 3-D objects	Cross section of 3-D tissue structures
Intensity function	Smooth, slow varying across objects	Speckle-like pattern, rapidly varying
Motion types	Translation + rotation rigid	Translation + rotation + deformation
Typical resolution	Pixel resolution (approx.)	Pulse dimension resolution
Challenges	Changes in external illumination, occlusion, aperture problems, no gray value changes	Low SNR, speckle decorrelation, motion ambiguities, spatial aliasing

In this chapter, we propose a modified version of one of the BMAs. This modification makes the BMA more oriented to work with US data. We also utilize the inherent continuity in the imaged tissue to make an optimized version of the previously modified BMA. This continuity criterion accounts for the axial continuity, so we add a lateral continuity correction step to remove false peaks along the horizontal direction and enhance the resultant fields. Then, the effects of imposing more constraints on the optimized algorithm are studied. Also, we show the effects of the block size and postprocessing on the estimation output[3] **[41, 42]**.

3.1. Modified Exhaustive Search (ES)

3.1.1. Basic ES

We used one of the BMAs (commonly used in video compression domain) to estimate the displacement field of the precompression image. In the video compression domain, where the video is a series of frames, BMAs are based on dividing a frame into a matrix of non-overlapping square macro blocks and each block is compared with the

---

[3] Based on our work in this part, we published two papers in IEEE conferences cited in the "References" section of this thesis.

corresponding block and its adjacent neighbors in the previous frame to create a vector that represents the movement of a macro block in the previous frame from one location to another in the current frame. This movement, calculated for all the macro blocks comprising a frame, constitutes the displacement field.

The search criterion between blocks is based on minimizing a cost function. The searched block that generates the least cost is considered the best match for the reference block. Two cost functions are frequently used due to their simplicity, namely Mean Absolute Difference (MAD) and Mean Squared Error (MSE) given by the following equations:

$$MAD = \frac{1}{N^2}\sum_{i=0}^{N-1}\sum_{j=0}^{N-1}\left|G_{ij} - \acute{G}_{ij}\right|, \qquad MSE = \frac{1}{N^2}\sum_{i=0}^{N-1}\sum_{j=0}^{N-1}\left(G_{ij} - \acute{G}_{ij}\right)^2, \qquad 3.(1)$$

where N is the side of the macro bock, G_{ij} and $\acute{G}_{ij}$ are the pixels being compared in the reference macro block and searched macro block, respectively. The formula for the BMA is

$$MAD(m,n) = \frac{1}{N_1 N_2}\sum_{j=-\frac{N_2-1}{2}}^{\frac{N_2+1}{2}}\sum_{i=-\frac{N_1-1}{2}}^{\frac{N_1+1}{2}}\left|G(I+i, J+j) - \acute{G}(I+i+m, J+j+n)\right|, \qquad 3.(2)$$

where (m, n) is the search location (limited by the search range p), N_1 and N_2 are the horizontal and vertical block dimensions respectively, (I, J) is the location of the center of the reference image block.

For our application (US elastography), the search parameter p was initially set to 5 samples (the idea is represented in Figure 3.1(a)). There are various techniques for block matching which differ in accuracy and speed [43], but we chose to start with the most computationally expensive, yet most accurate, algorithm - the exhaustive search (ES), to assess the quality of motion fields generated using BMAs with RF data.
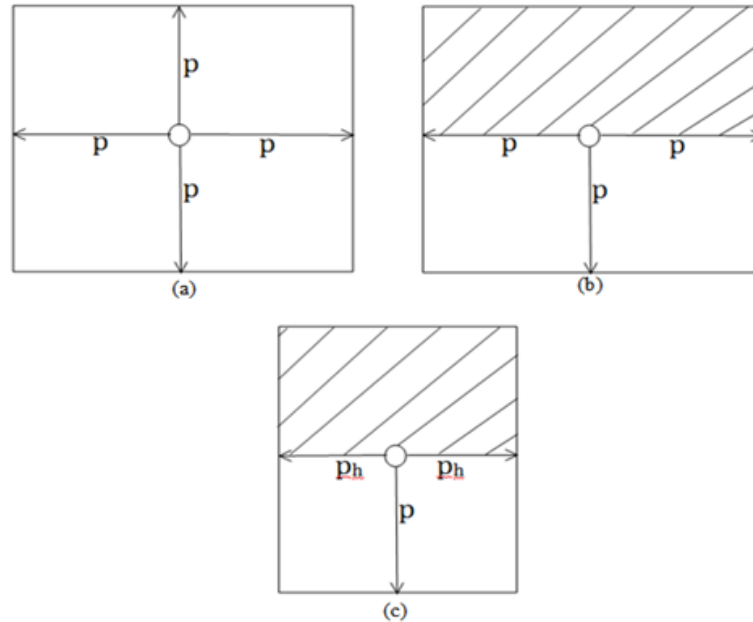
Figure 3.1: ES with modifications. (a) Basic ES. (b) ES with the first modification (lower-only search). (c) ES with the two modifications (lower-only and less horizontal search). In all configurations p represents the vertical search range and p_h represents the horizontal search range (which typically should be less than p).

The resultant axial TDE and strain (by LSQSE) fields by applying full ES to the whole (i.e. not cropped) RF data are shown in Figure 3.2. The size of the RF data is 1700*508 and we used a block size of 5*5 (empirical). The $SNRe$, $CNRe$ and runtime (t_{TDE}) for full ES are shown in Table 3.2 (the background and target measurement windows are delineated by the white rectangles in Figure 3.2(b)). The resulting fields are noisy and not comprehensible (compared to the ideal TDE field in Figure 2.11 (b)) and thus the quantitative measurements are not meaningful. Consequently, in the following sections we show our trials to modify and optimize the full ES algorithm to get better results.

Table 3.2: Quantitative measurements for full ES.

$SNRe$	$CNRe$	t_{TDE} (s)
0.01	0.01	742.23

(a) (b)
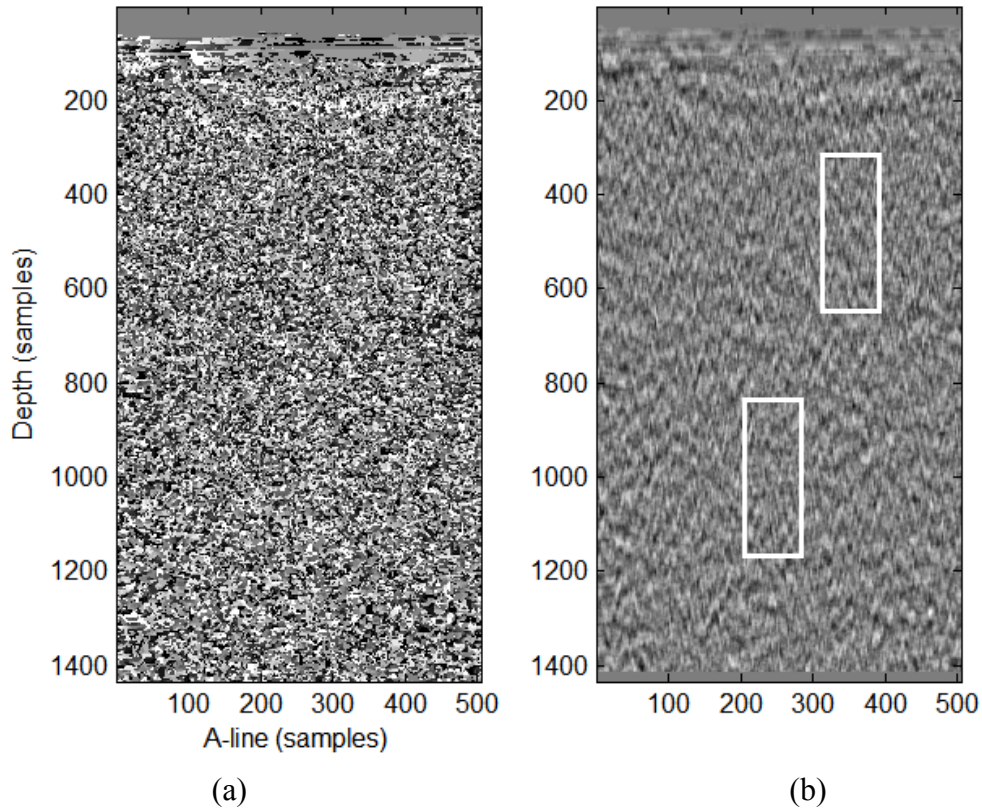
Figure 3.2: Axial (a) TDE and (b) strain fields by full ES.

3.1.2. First modification

After compressing the imaged tissue by the probe, the distance between any locus in the tissue and the probe gets smaller. Consequently, every locus appears in an upper location in the postcompression image than its original location in the precompression image. Utilizing this, and because we were using the postcompression image as the

reference image, we applied a modification to the ES algorithm in which we limit the search range vertically to the lower half of the search window (see Figure 3.1(b)). We expected this modification to enhance the quality of the displacement field (besides enhancing speed definitely) as it should reduce false positives. We set the vertical search range for ES to the applied axial compression depth (as it is the upper limit) according to the following formula:

$$dz \; [samples] = \frac{dz \; [m]}{c/2} \times f_s, \qquad \qquad 3.(3)$$

where dz is the applied compression length (0.2 inch), f_s is the sampling frequency (40 Mhz in our case) and c is the US wave propagation speed (assumed 1540 m/s). According to 3.(3), dz in samples was 264 and thus, even if this search range theoretically should contain any motion vectors, getting a result using such a huge search range is hard for a serial implementation of the ES algorithm.

3.1.3. Second modification

An additional property of elastography images is that the majority of the displacement should be in the vertical (axial) direction due to the nature of the compression (which is axial). This let us apply an additional modification to the ES algorithm in which we limited the search range in the horizontal (lateral) direction (as shown in Figure 3.1(c)) where p_h is the horizontal search parameter. Typically p_h should be less than p (we set p_h to 2). Again we expected this to further reduce false positives in addition to enhancing speed.

The resultant axial TDE and strain fields by applying the modified ES to the whole RF data are shown in Figure 3.3. The $SNRe, CNRe$ and runtime (t_{TDE}) for the modified ES are shown in Table 3.3.
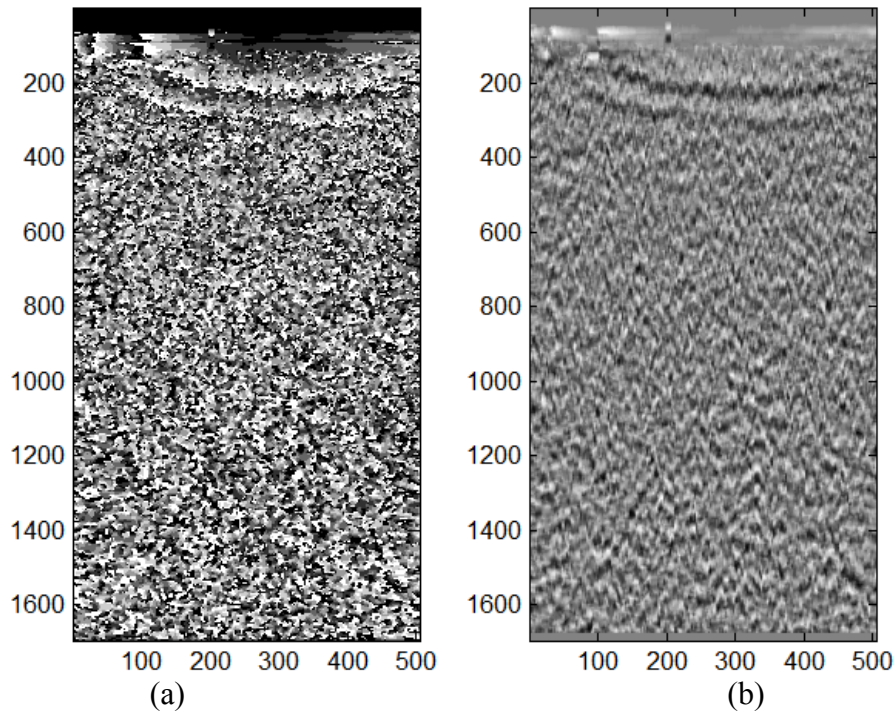
Figure 3.3: Axial (a) TDE and (b) strain fields by modified ES.

Table 3.3: Quantitative measurements for modified ES.

$SNRe$	$CNRe$	t_{TDE} (s)
0.03	0.04	210.31

3.1.4. Problems of the modified ES

The results show that the modified ES still does not produce a comprehensible strain field. This can be understood because the search ranges are empirical and small, so the search window may not contain the corresponding block for the current reference block. Also, the modified ES does not exploit the inherent tissue continuity and thus may be subject to false detections.

3.2. Optimization of Modified ES (Exploiting Tissue Continuity)

3.2.1. Axial continuity constraint (Axial Apriori)

A main problem facing application of conventional ES to elastography data (even after the previous two modifications) is that the continuity of displacement fields (as the tissue is a continuum) is not exploited by conventional ES. This results in noisy displacement fields with no continuity and with false peaks (especially when the search range is big) in addition to long search time.

To solve this problem, it is stated in [24] that due to the continuity of motion and low value of applied strain, movement of adjacent regions in the RF frame should not vary significantly. We applied the same concept to the BM problem as follows: let that the axial displacement of location (I, J) in the RF frame be $d_{axl}(I, J)$, then we can confine the search range for the axial displacement of the lower sample, $(I, J + 1)$, to $d_{axl}(I, J) - 1$, $d_{axl}(I, J)$, $d_{axl}(I, J) + 1$. This is equivalent to limiting the search range for the lower sample to 1 sample in the 4 directions provided that the search center is now updated with the displacement of the upper sample (i.e. the new search center is $(I, J + 1 + d_{axl}(I, J))$, not $(I, J + 1)$). Applying the same concept to lateral displacement, then we could confine the search range for displacement of location $(I, J + 1)$, to a 3-by-3 window centered at the location guided by the already-estimated displacement of the adjacent (upper) sample. This guided location is $(I + d_{lat}(I, J), J + 1 + d_{axl}(I, J))$. This idea can be expressed mathematically by changing the original formula of block matching from 3.(2) to

$$MAD(m,n) = \frac{1}{N_1 N_2} \sum_{j=-\frac{N_2-1}{2}}^{\frac{N_2+1}{2}} \sum_{i=-\frac{N_1-1}{2}}^{\frac{N_1+1}{2}} |G(I+i, J+1+j) - \acute{G}(I + d_{lat}(I,J) + i + m, J + 1 + d_{axl}(I,J) + j + n)|, \qquad 3.(4)$$

where m and n will be confined to -1, 0 and 1 only (i.e. a 3-by-3 search region around the guided search center).

To apply the previous idea, one should estimate the displacement field for the first row in the reference image region of interest (ROI) then use this estimate as a basis for the lower rows. So, we did modified ES for the first row (as no apriori are found yet) then used the resultant displacement vectors to guide the search for displacements of lower samples.

We implemented this modification using the axial search range calculated by 3.(3) for the first row for full search and using a lateral search range = 10 A-lines (empirical). The resultant axial TDE and strain fields by applying this optimized ES to the whole RF data are shown in Figure 3.4. In Figure 3.5, the TDE for the A-line whose index is 400 is shown separately for better visualization of the TDE trend. The $SNRe$, $CNRe$ and runtime (t_{TDE}) for the optimized ES are shown in Table 3.4.

(a)   (b)
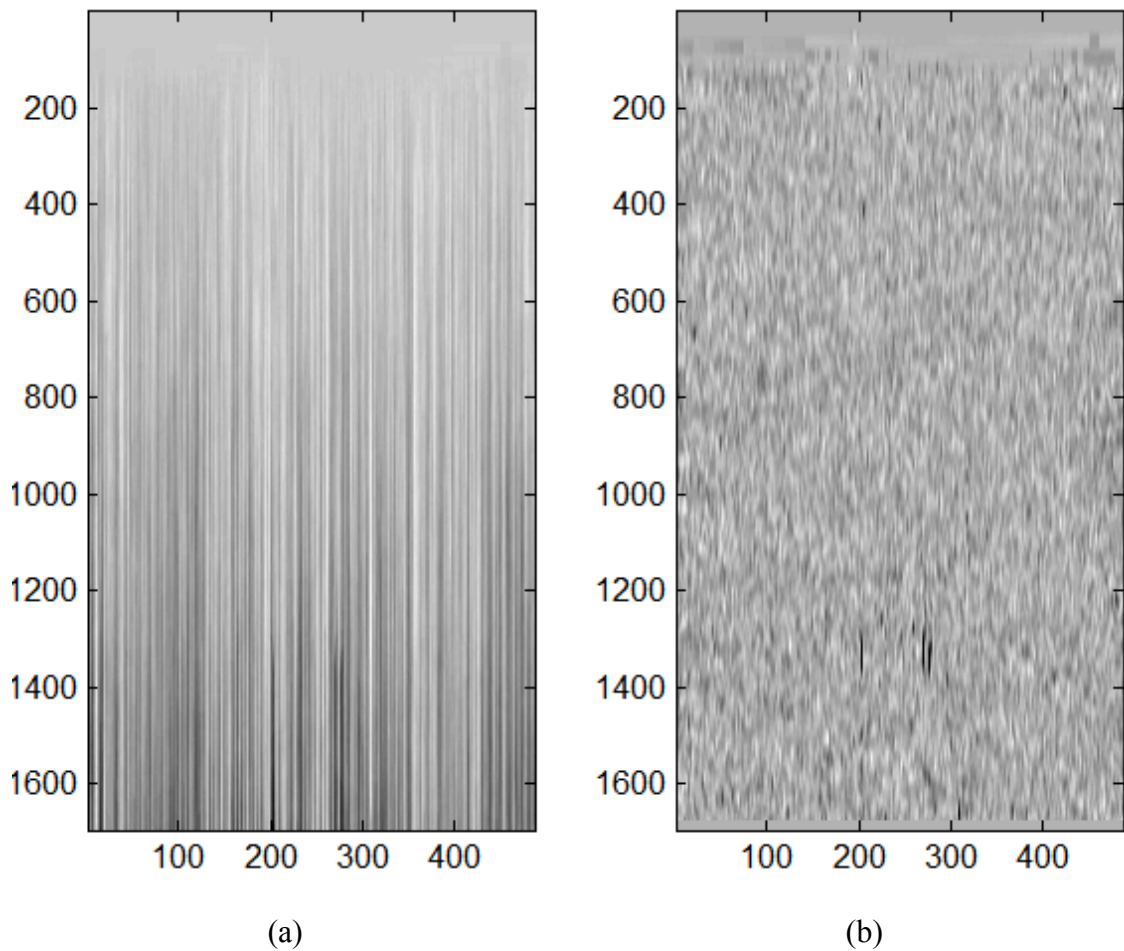
Figure 3.4: Axial (a) TDE and (b) strain fields by optimized ES (exploiting the inherent axial TDE continuity of tissues).

Table 3.4: Quantitative measurements for optimized ES.

$SNRe$	$CNRe$	t_{TDE} (s)
1.91	0.15	87.14

The results in Figure 3.4 and Figure 3.5 show that the axial TDE field undergoes axial continuity after imposing continuity condition in this algorithm (optimized ES).. Although the search window for the first row of the reference image is larger than that for the modified ES, Table 3.4 shows that the time for the optimized ES is overall less than that of modified ES (about 2.4x decrease - refer to Table 3.3). This is because full search is done only for the first row, then the search region is reduced to 3-by-3 for the rest of the reference samples.
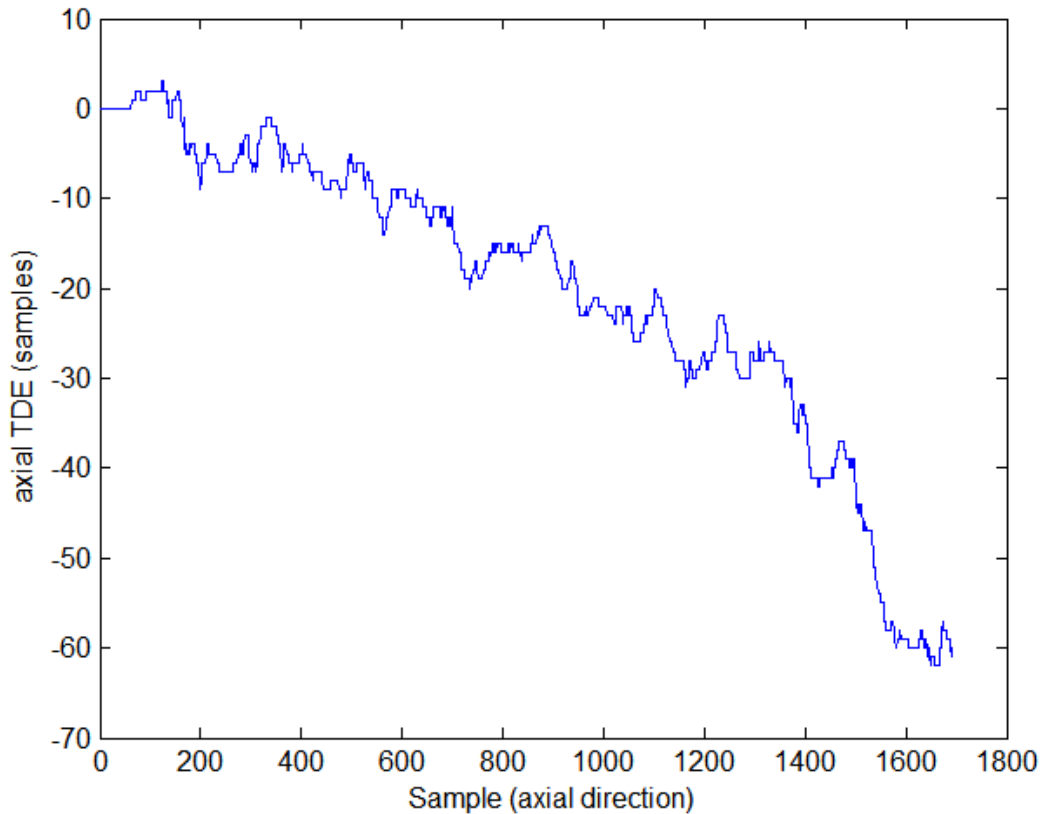
Figure 3.5: Axial TDE profile (by optimized ES) for the A-line whose index is 400.

However, it can be seen from Figure 3.4 (a) that the axial TDE undergoes lateral discontinuity. This can be seen also in Figure 3.6, in which the TDE for sample 500 axially is shown separately for. The reason for this is that the large search region for the first row leads to some false peaks appearing in the displacement estimation of the first row. Since this estimation is used to guide the search for the lower row (and so on), the false peaks propagate along the axial direction.

3.2.2. Lateral Continuity Correction (LCC)

We tried to solve the lateral discontinuity problem of the axial TDE field by applying 1D median filtration to the displacement estimates of each row to remove the outliers (false detections) before proceeding to the lower rows. The results of applying 1-by-15 median filtration as a LCC method to the axial TDE field in Figure 3.4 (a) are shown in Figure 3.7. We can see that the axial TDE field exhibits better lateral continuity (with some discontinuities still existing, especially at locations 205 and 340 laterally). The lesion boundaries are somehow delineated in the axial strain field in

Figure 3.7 (b) as shown by the red contour. This improvement in qualitative results comes also with improvement in the *SNRe* and *CNRe* values shown in Table 3.5 compared to quantitative results before the LCC step. Despite its improvement in both qualitative and quantitative results, the LCC step did not affect the runtime t_{TDE} compared to the runtime of the optimized ES without LCC in Table 3.4.
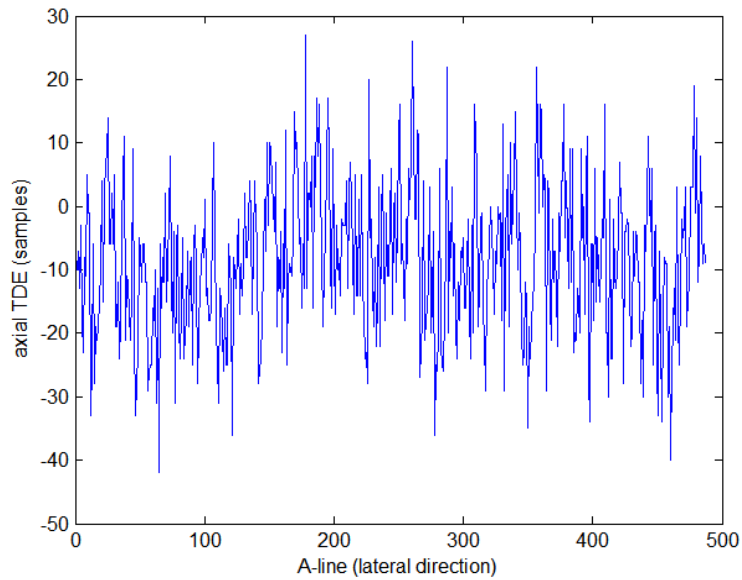
Figure 3.6: Axial TDE profile (by optimized ES) at sample 500.

(a)   (b)
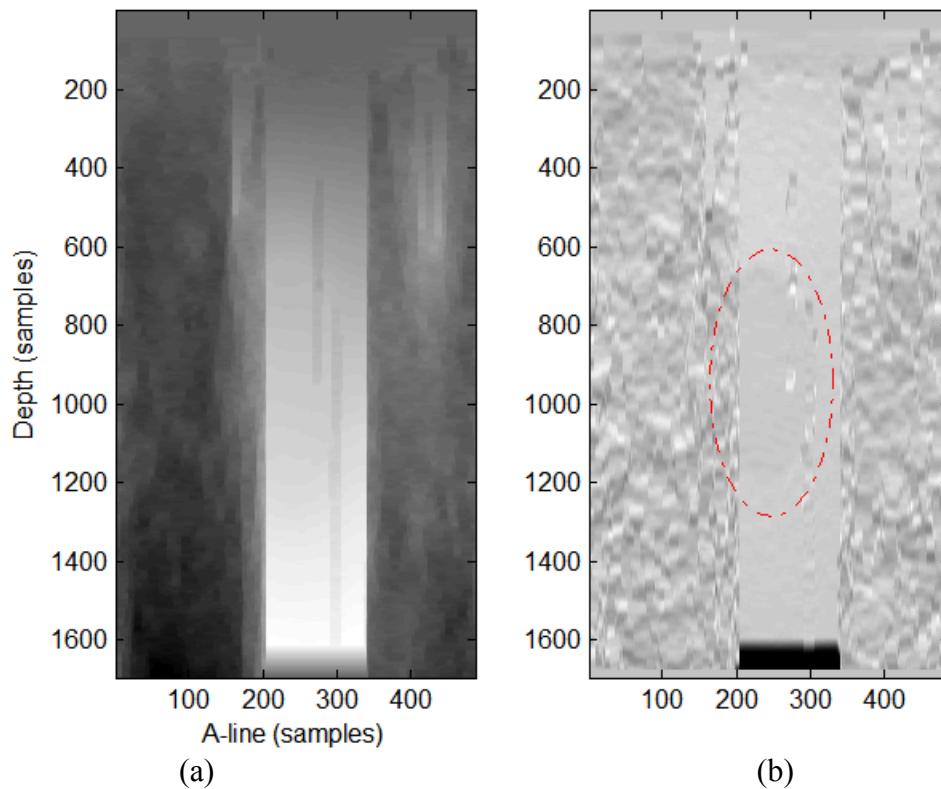
Figure 3.7: Axial (a) TDE and (b) strain fields by applying 1-by-15 median filtration as a LCC method to the axial TDE field in Figure 3.4 (a).

Table 3.5: Quantitative measurements for optimized ES with LCC.

$SNRe$	$CNRe$	t_{TDE} (s)
2.97	0.18	89.97

3.2.3. Limiting axial search to the lower region of guided search center

As stated in 3.2.1, the search region (m,n) were confined to -1, 0 and 1 only (i.e. a 3-by-3 search region around the guided search center). This resulted in the axial TDE and strain profiles shown in Figure 3.8 at A-line 160 (chosen arbitrarily). However, according to the ideal TDE field in Figure 2.11 (b), the axial TDE field for a homogeneous phantom with a stiff inclusion[4] should be single-signed and monotonic (consequently, the strain should be single-signed) [30]. The sign will be positive if the reference frame is the postcompression frame and vice versa. The reason for this is the following: since all measurements are relative to the transducer, the TDE at the start of the echo is smaller than at the end. For a phantom with a homogenous elastic modulus, the TDE would start at zero for the closest segment and increase up to $\frac{dz}{c/2}$ for the last segment. If there are changes in the elastic modulus along the A-line, then the increase in the time shift may be zero or very small in certain segments [44].

(a)   (b)
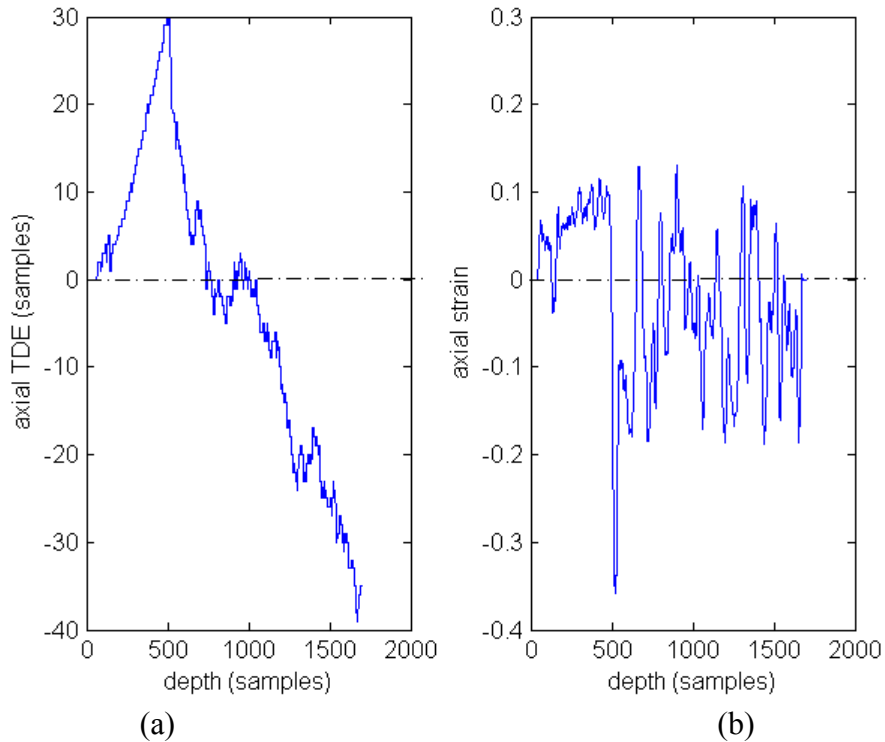
Figure 3.8: Axial (a) TDE and (b) strain profiles at A-line 160 (by applying optimized ES with LCC).

---

[4] This condition might not hold for in-vivo imaging where internal motion (e.g. blood flow) can exist. This can reverse the sign of the axial TDE even if the applied strain is axial and in one direction.

As seen in Figure 3.8, neither of the two constraints (single-sign and monotonicity of TDE) is satisfied. To apply this constraint to the optimized ES algorithm, Eq. 3.(4) will not change but the axial search range n will be constrained to values ≥ 0. This is another physical constraint (similar to the constraint in 3.1.2) that should be applied to the optimized ES (in addition to the axial and lateral continuity constraints previously applied).

Applying this constraint to the optimized ES resulted in the axial TDE and strain profiles shown in Figure 3.9 at A-line 160. By examining this figure, we can see that the axial TDE profile adheres to the single-sign (positive in our case) and monotonicity constraints and the axial strain consequently adheres to the single-sign constraint. However, the axial TDE profile begins to decay with a constant slope after a certain depth indicated by the vertical red line on Figure 3.9. This problem is investigated in the next section. The reduction in search range by this constraint by a factor of $\frac{2}{3}$ led to a reduction in t_{TDE} to 66.37 s. Comparing this value to t_{TDE} in Table 3.5, we find that the reduction is slightly less than $\frac{2}{3}$ due to the full modified ES search for the first row which is not affected by this constraint.
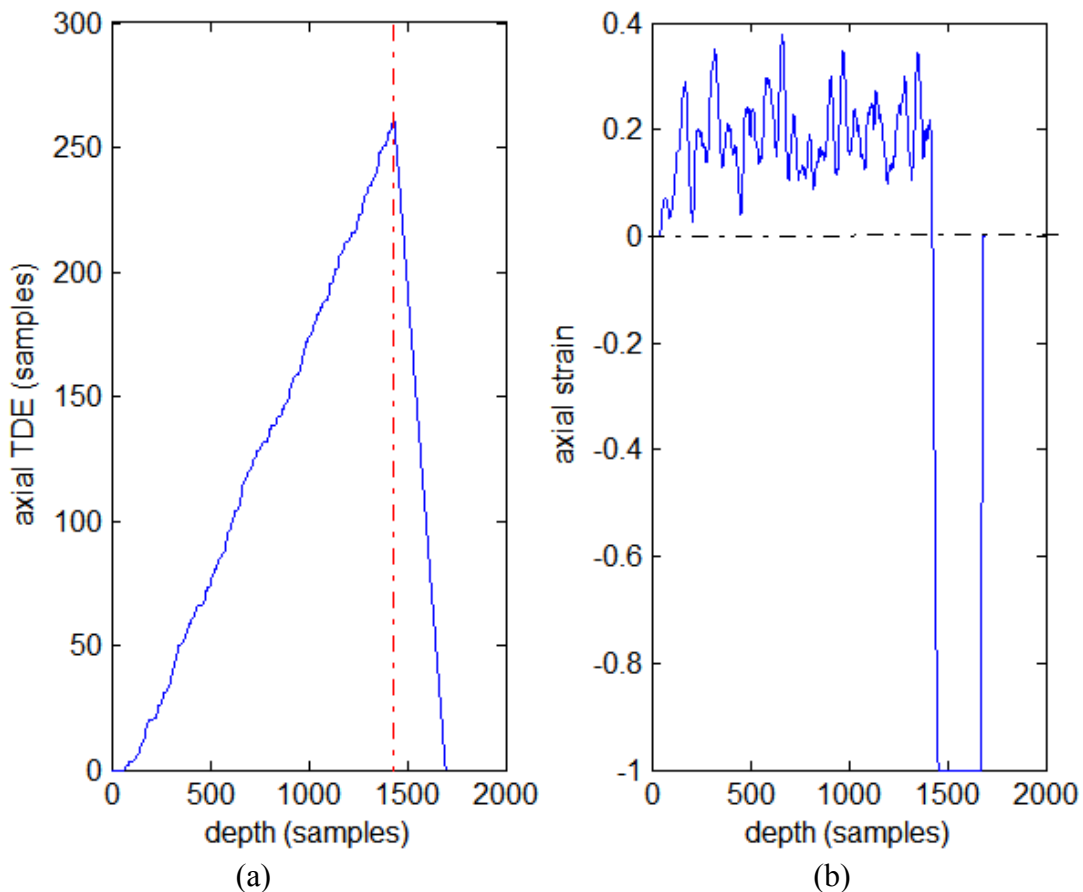
Figure 3.9: Axial (a) TDE and (b) strain profiles at A-line 160 after applying single-sign and monotonicity constraints to the optimized ES with LCC.

3.2.4. Axial FOV limitation

Figure 3.9 (a) shows that axial TDE begins to decline after a certain depth (after the vertical red line). This behavior disagrees with the ideal TDE profile in Figure 2.11 (b) that shows that the axial TDE should increase gradually from zero for the closest segment to the probe to $\frac{dz}{c/2}$. By examining our implementation, we found that some points appearing in the FOV of the postcompression RF frame will not be found in the FOV in the precompression frame. This is clarified in Figure 3.10. So, it is wrong to search for such points in the precompression frame. The depth added to the FOV in the postcompression state that was not included in the precompression state is equal to the applied displacement dz. That is,

$$d_{max} = H_{FOV} - \frac{dz}{c/2} \times f_s, \qquad 3.(5)$$

where d_{max} is the maximum depth in the postcompression frame for which displacement estimation can be done, H_{FOV} is the FOV height (i.e. image depth) , and $\frac{dz}{c/2} \times f_s$ is the applied displacement (in samples – refer to Eq. 3.(3)). This limitation is reported also in [38].
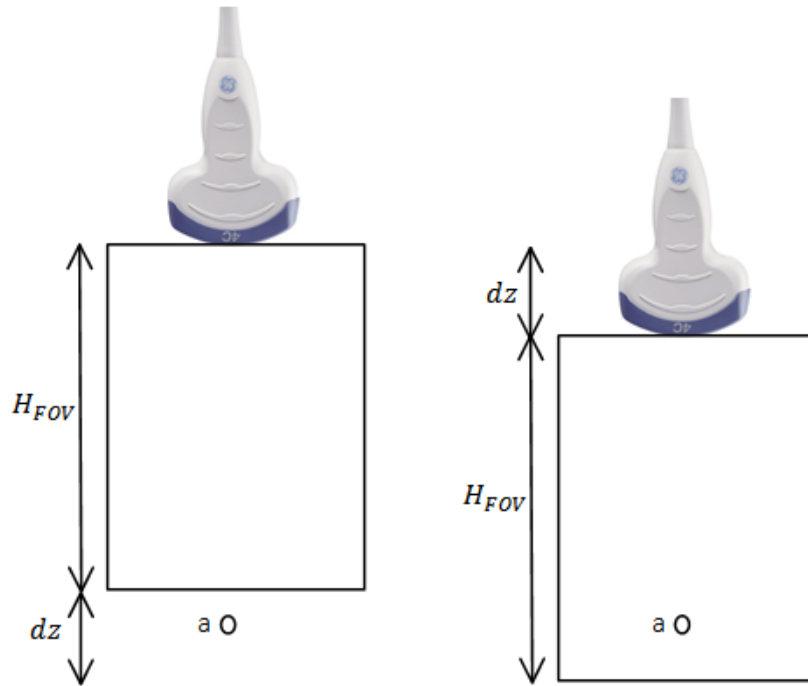
Figure 3.10: The scatterer at point a entered the FOV of the US probe after the compression. Hence, it is not possible to search for it in the precompression image (the reference image in our case is the postcompression).

By adding this constraint to the optimized ES algorithm, the axial TDE profile at A-line 160 is shown in Figure 3.11. This is the same as Figure 3.9 (a) but with excluding the erroneous zone after d_{max}. This axial TDE profile adheres to the single-sign and monotonicity constraints.
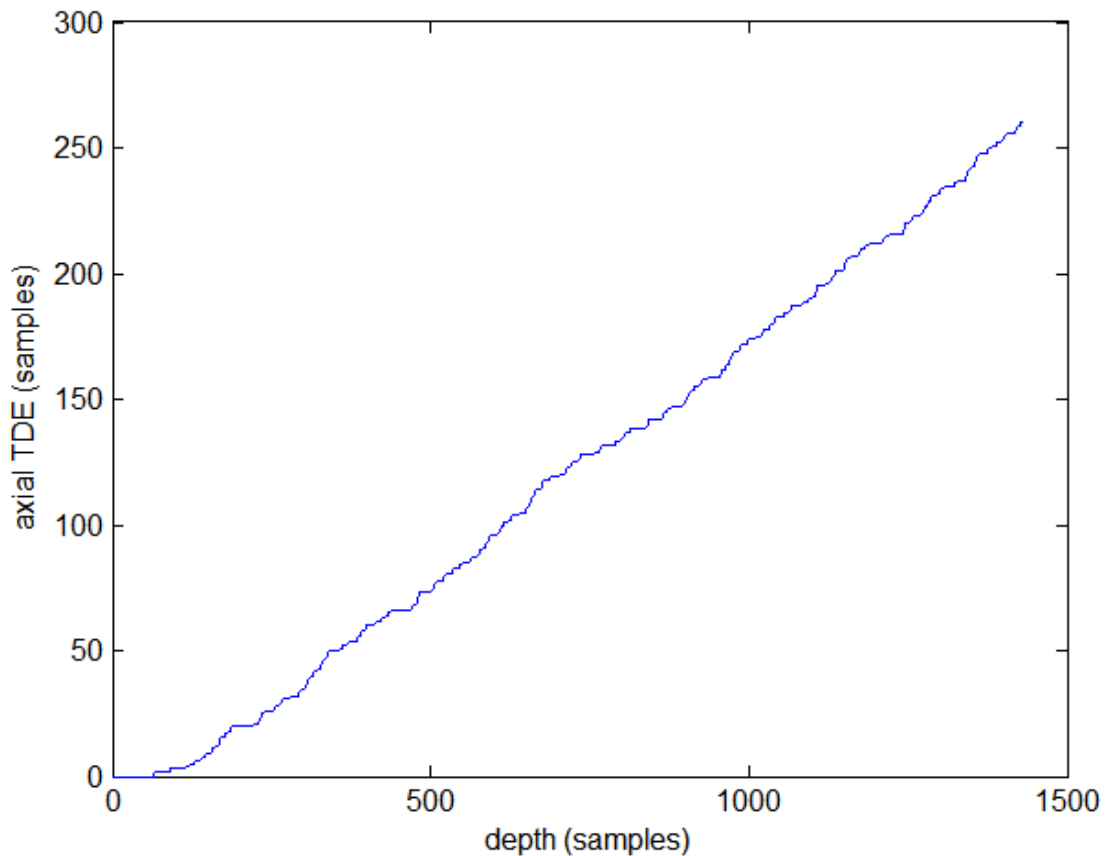
Figure 3.11: Axial TDE profile at A-line 160 after excluding the lower erroneous zone from the same profile in Figure 3.9 (a).

3.3. Effect of block size and shape

The kernel (block) size is a major parameter in BMAs affecting the accuracy and resolution of the resultant elastogram and the runtime of the TDE algorithm. Both the kernel size and shape can affect the output of the BMA. A trade-off between speckle tracking accuracy and spatial resolution based on the selection of block size should be done. The advantages of both large and small matching blocks are discussed in the following paragraph.

A large kernel size reduces the noise effects in the image and can improve image contrast as it increases the uniqueness of each data block and aligns the local data of weak or homogeneous speckle patterns to those of strong or structural speckle patterns [45]. However, a smaller kernel means a finer resolution and a better estimation of the displacement. That is, the gain in accuracy by using large blocks is usually at the expense of spatial resolution. In other words, a small kernel (about half the area of the 2D pulse-echo PSF of the US system) has the advantage of the assumption of rigid body motion which is increasingly accurate as the size of the kernel is decreased, and because spatial resolution is expected to improve with smaller kernels. For this reason, BMA using large matching blocks fail to resolve non-rigid or highly varying motion fields. By using a smaller size matching block, block matching algorithms perform better in resolving highly varying motion fields and avoid the problem of nonuniform motion vectors, often at the expense of increased susceptibility to noise and speckle

decorrelation-related tracking errors because they are prone to pattern matching ambiguities that can lead to displacement estimation errors. These ambiguities are due to RF echo signal de-correlation, echo signal saturation, specular reflection, homogeneous regions of weak scattering.

In Figure 3.12, Figure 3.13 and Figure 3.14[5], we show the effect of varying block size on the quality of the resultant axial TDE and strain fields by applying the optimized ES algorithm with all the constraints developed earlier. It could be seen that the smoothness of the TDE field and the visual quality of the strain field enhance gradually till a certain block size (by visual judgment, the best fields were determined at block size = 33*33 (Figure 3.13(a-b))) then begins to deteriorate again. As mentioned before, when choosing the kernel size, one should understand the tradeoff between the spatial resolution and the detection accuracy. The quantitative measures are shown in Table 3.6 (note that the background and target measurement windows are delineated with white and red rectangles in Figure 3.12(b) respectively). It is shown that a block size of 33*33 gives the best combination of SNR_e and CNR_e among our trials. This is in conformation with visual assessment. For the SNR_e and CNR_e measurements to be more reliable, we should take several values at different window locations in the background and the target. Concerning runtime, Figure 3.17 suggests a linear growth rate ($O(n)$) of t_{TDE} with block size.
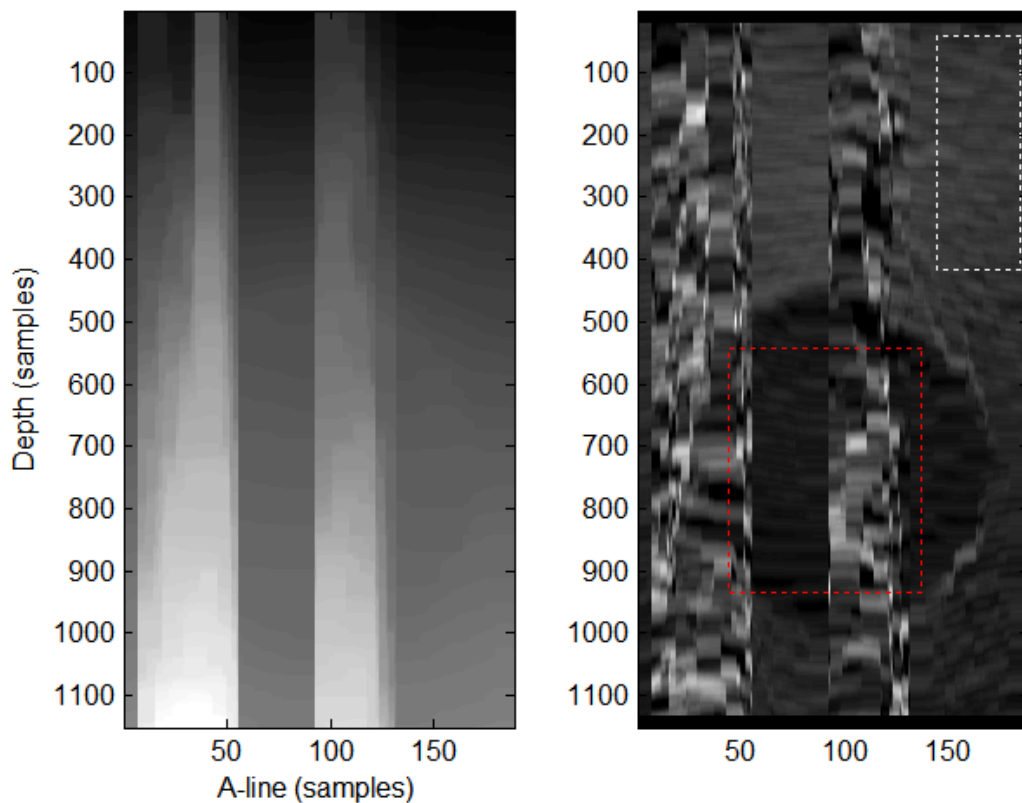
[5] Starting from this section, we will make our tests on the ROI around the inclusion (shown in Figure 2.9(c,d)), not the whole RF frame.
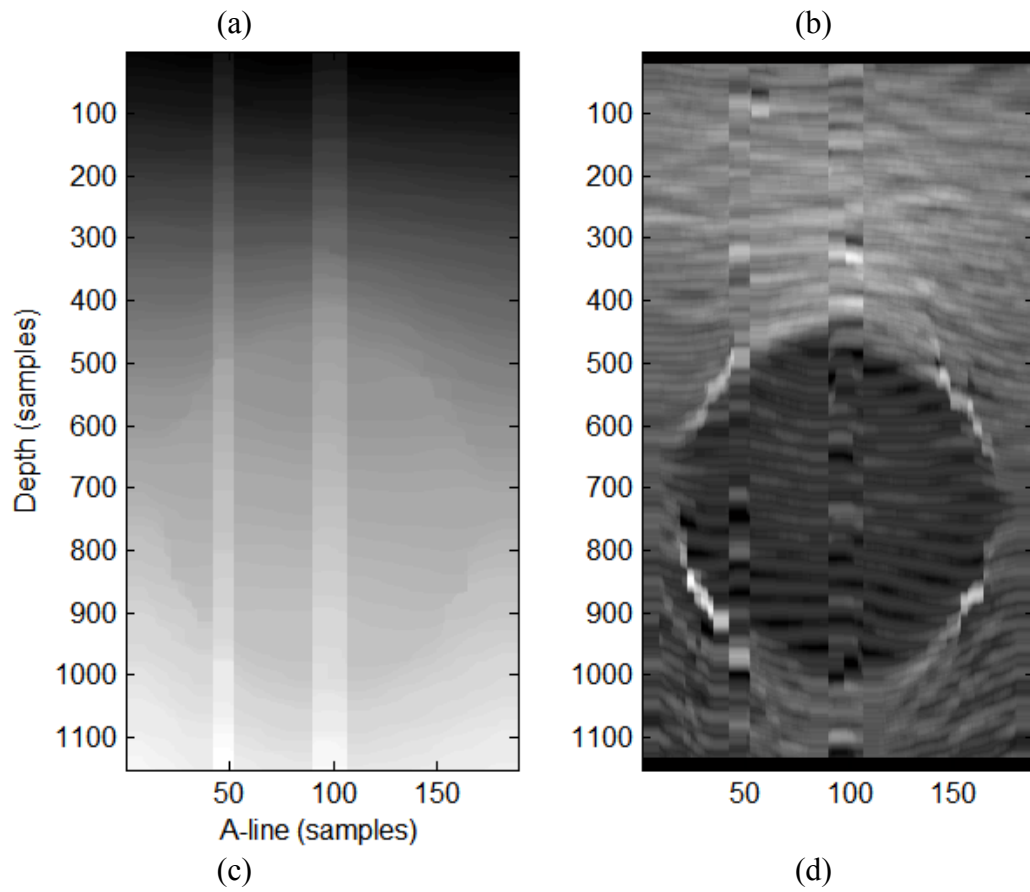
Figure 3.12: Axial (a) TDE and (b) strain fields by optimized ES with all constraints at block size = 11*11. Axial (c) TDE and (d) strain fields by optimized ES with all constraints at block size = 21*21.
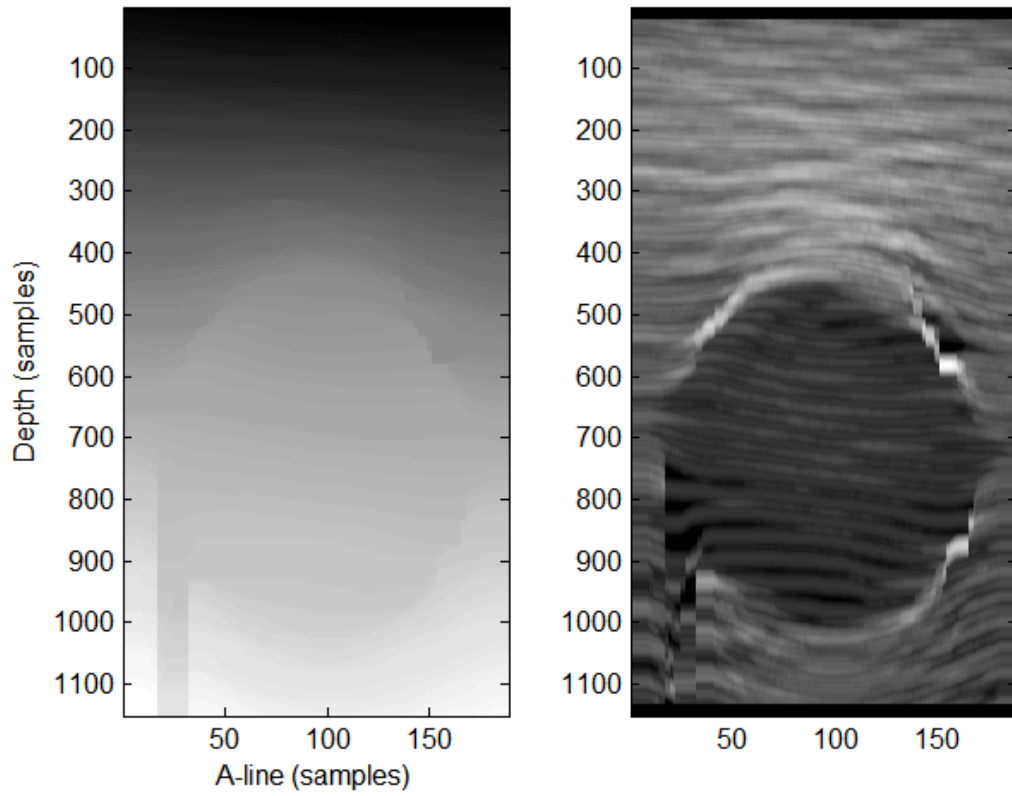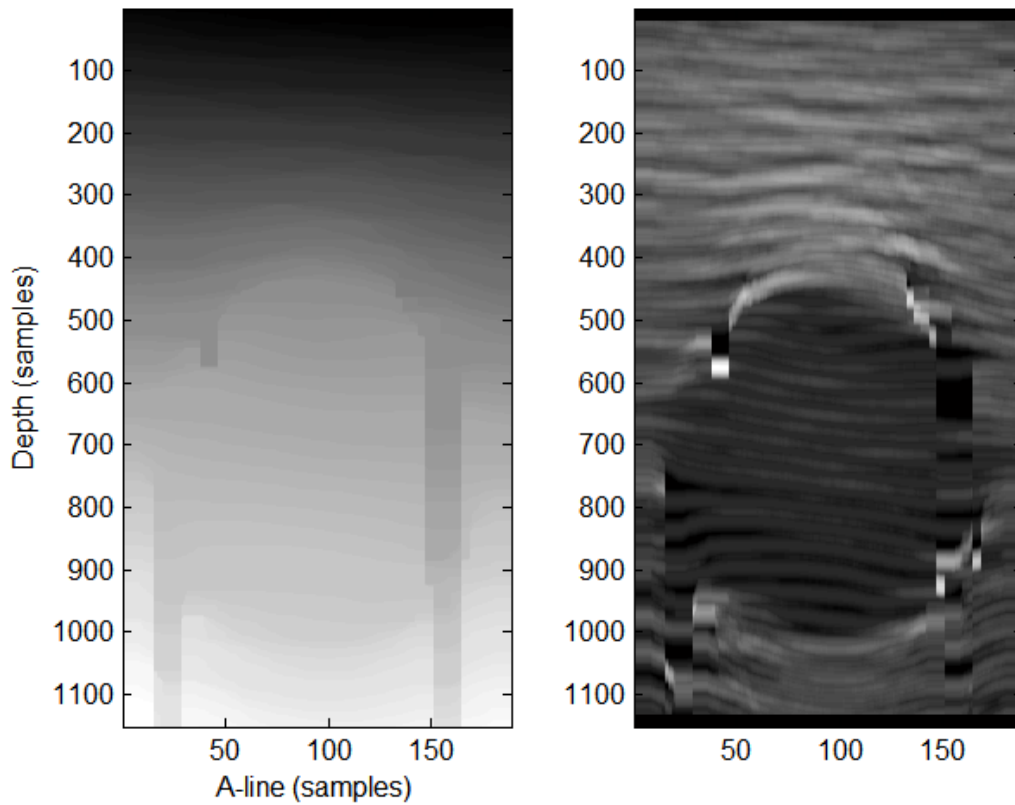
Figure 3.13: Axial (a) TDE and (b) strain fields by optimized ES with all constraints at block size = 33*33. Axial (c) TDE and (d) strain fields by optimized ES with all constraints at block size = 41*41.
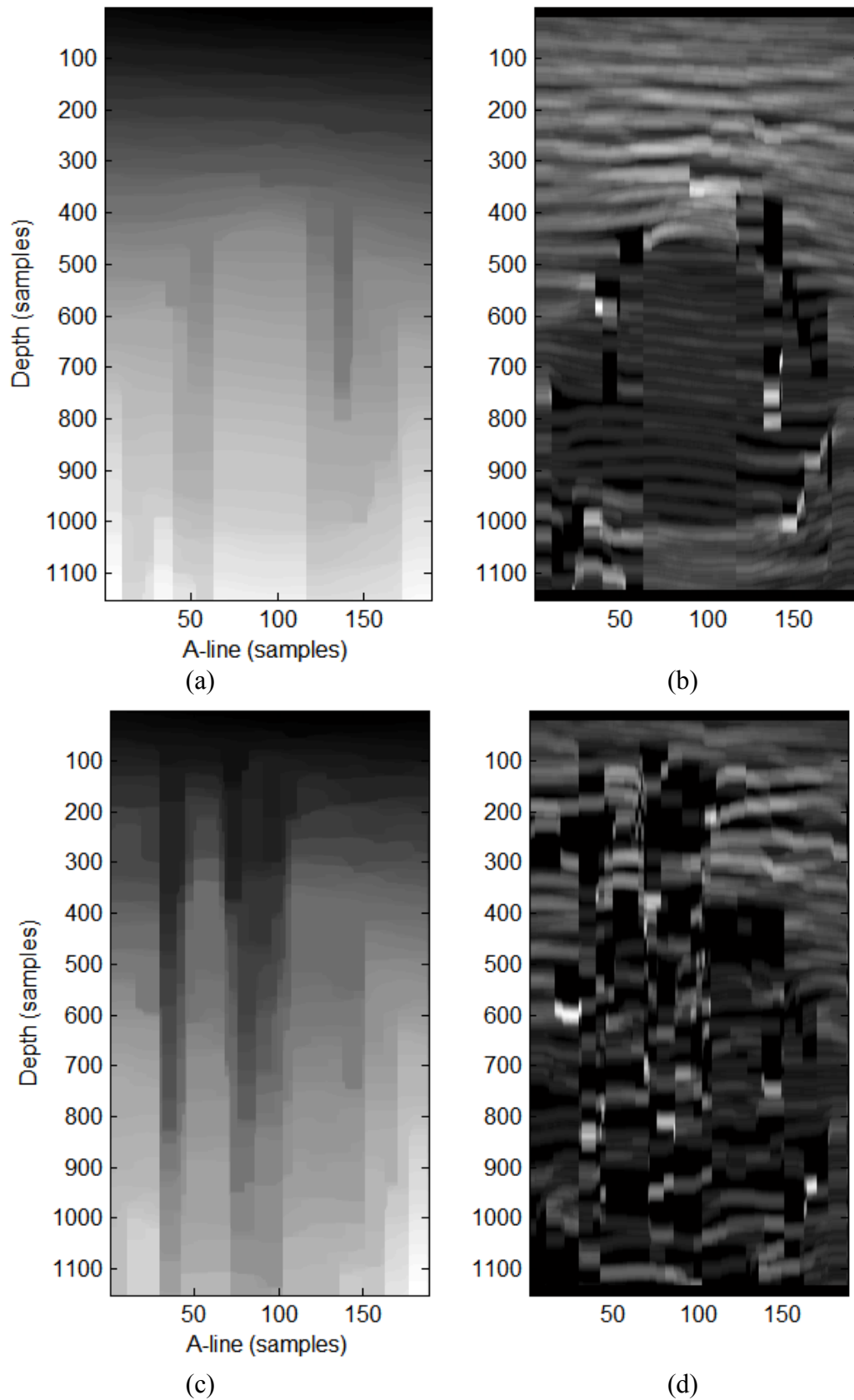
Figure 3.14: Axial (a) TDE and (b) strain fields by optimized ES with all constraints at block size = 51*51. Axial (c) TDE and (d) strain fields by optimized ES with all constraints at block size = 63*63.

Table 3.6: Quantitative measurements of strain elastogram generated by optimized ES at different block size.

block size (samples)	11×11	21×21	33×33	41×41	51×51	63×63
SNR_e	8.82	9.42	7.9	6.58	5	2.3
CNR_e	0.37	5.33	5.51	4.24	3.04	1.26
t_{TDE} (s)	31.27±0.36	48.62±0.02	83.57±0.07	118.12±3.18	166.8±0.26	236.48±0.28
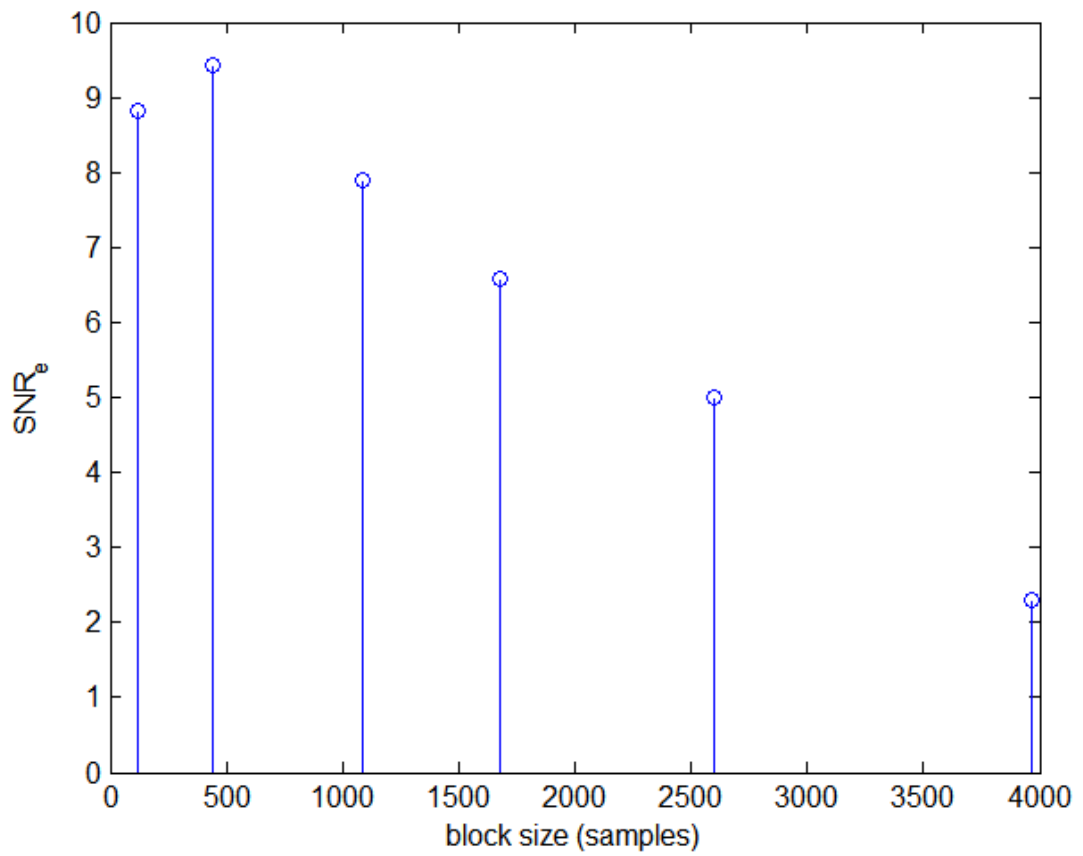
Figure 3.15: SNR_e values for strain estimation by optimized ES with all constraints at different block sizes.
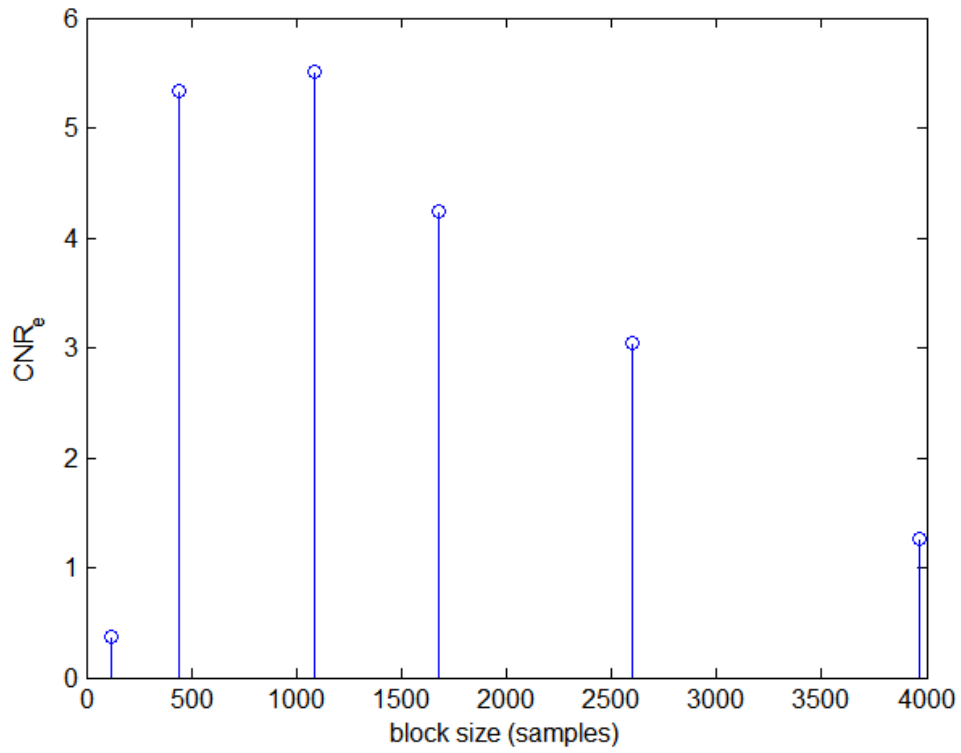
Figure 3.16: CNR_e **values for strain estimation by optimized ES with all constraints at different block sizes.**
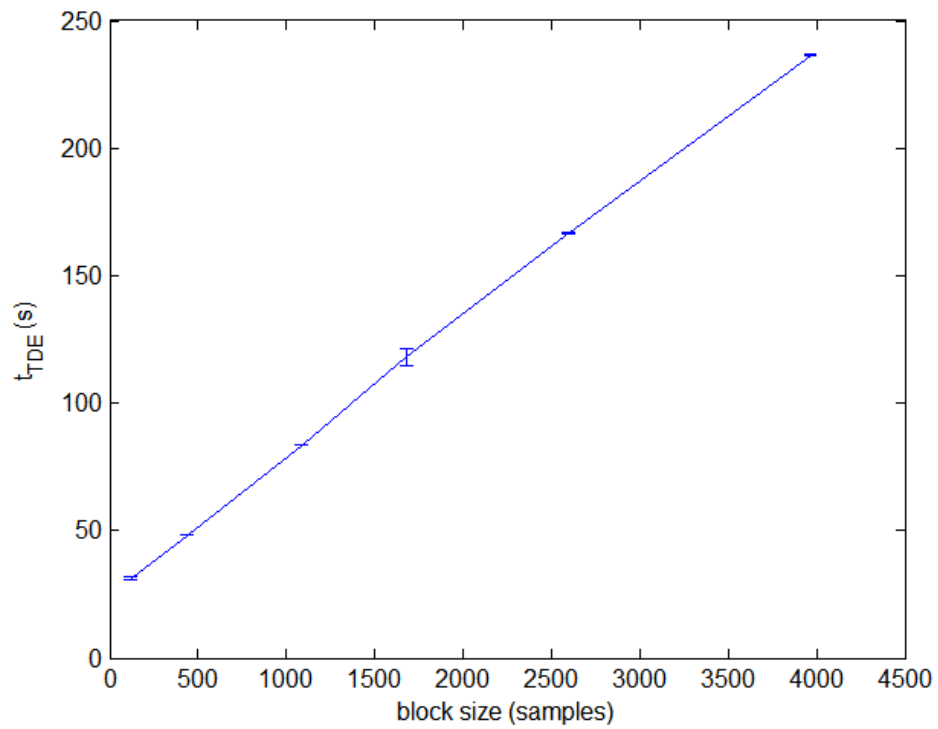
Figure 3.17: t_{TDE} **values for strain estimation by optimized ES with all constraints at different block sizes.**

42

The qualitative and quantitative results reported in Figure 3.12–Figure 3.17 are for fixed-size rectangular blocks. However, automatic selection of the block size and shape is desirable. A recent study showed that the optimal block size is a function of the area of 2D pulse-echo PSF of the US system [46]. The formation of an US RF image $r(x, y)$ can be modeled by a linear realtion involving the PSF of the US imaging system $h(x, y)$ and a discrete distribution of scatterers representing the medium $d(x, y)$ in the 2D space by the following relation [47, 48]:

$$r(x, y) = h(x, y) \circledast d(x, y),$$ 3.(6)

where $\circledast$ denotes the convolution operator defined as

$$f(x, y) \circledast g(x, y) \triangleq \iint_{-\infty}^{\infty} f(x, y) \circledast g(\eta - x, \beta - y) d\eta d\beta,$$ 3.(7)

and the scatterer distribution can be expressed as

$$d(x, y) = \sum_i A_i \delta(x - x_i, y - y_i),$$ 3.(8)

where A_i represents the ith scatter echogenicity and (x_i, y_i) its position. The area of the PSF $A_{PSF}(d)$ is depth dependent [46] and can be described as

$$A_{PSF}(d) = \Delta l(d) \times \Delta d(d),$$ 3.(9)

where $\Delta l(d)$ is the -20 dB width of the lateral profile of the US field and $\Delta d(d)$ is the -20 dB axial length of the envelope of the US pulse.

For the system used in [46] study, the axial and lateral beam profiles are shown in Figure 3.18. They reported that the optimal kernel size at a certain depth $\{W_{l_o}(d) \times W_{d_o}(d)\}$ can be determined as

$$\pm 2 \propto_{opt} (d, SNR(p_j; d)) (\Delta l(d) \times \Delta d(d)),$$ 3.(10)

where $\propto$ is a proportionality factor that is different in the areas at the boundary of the image from inside the ROI.
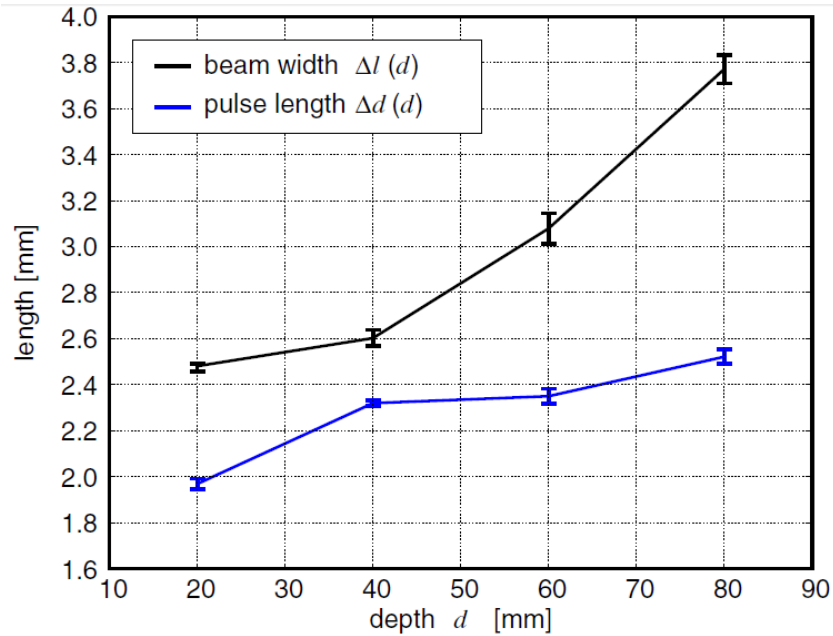
Figure 3.18: Distribution of -20 dB widths of lateral amplitude profile $\Delta l(d)$ and pulse envelope $\Delta d(d)$ of ultrasonic pulse at depths of 20, 40, 60, and 80 mm [46].

Eqn. 3.(10) shows that the optimal kernel size is not fixed, but depth-dependent and non-square. It shows also that the kernel size should get bigger with the depth of interest (this can be seen also from Figure 3.18). However, the study in [46] did not provide analytical expression for $\Delta l(d)$ and $\Delta d(d)$ as a function of US imaging parameters (f_c, BW, beamforming (focusing and apodization)) but measured it experimentally at several depths. This was not available in our study but can be investigated in the future (specially that in [46] study they were using curvilinear probes while we use rectilinear probes). Other studies provide more information about analytical calculation of US PSF for different US imaging parameters under certain assumptions [49, 50].

3.4. LCC in Optimized ES by Linear Regression

As shown before (see the enhancement from Figure 3.4 to Figure 3.7), the LCC step is a fundamental part in the TDE step in order to account for the lateral continuity property which is inherent in the imaged tissue. Until this point of discussion, we were using a 1D moving median filter along the TDEs of each row in the ROI to check & correct for lateral continuity before moving to the next (lower) row. Moving linear regression (least squares) windows can also be used to do LCC [51, 52]. In this technique, a finite 1D window is centered around a TDE point and a linear regression estimate is generated for each point in this window. Then, each point in this window is compared with the corresponding linear regression estimate. If the absolute difference between the two values is bigger than a certain threshold, the TDE at this point is considered a false peak and is replaced with its linear regression estimate. The regression window is then moved to the next TDE point until all the TDEs along the current row are checked for lateral continuity and corrected before proceeding to the TDE step of the lower row. The regression window needs to be small and overlapping because the correction step along the TDEs row is incremental. That is, the corrected TDE point should be used for the correction of the next point along the row.

We show the results of using an ordinary linear regression filter for LCC in Figure 3.19, Figure 3.20 for block sizes of 11 and 33 respectively. The regression window length was 3 RF samples and the threshold used for false peak detection was 0.5σ, where σ is the standard deviation of the TDEs in the current regression window. Also, the results of using robust linear regression (via iterative reweighted least squares (IRLS)) [53] are shown in Figure 3.21 and Figure 3.22 for block sizes of 11 and 33 respectively. A comparison of the runtime t_{TDE} between LCC using median filtration, ordinary linear regression and robust linear regression is shown in Table 3.7 for block sizes of 11 and 33 respectively. Despite being a naïve salt-and-pepper noise removal filter, the median filtration effect on quality and runtime was better than those of linear regression filter. We need to investigate the effect of different regression window sizes and detection threshold values on the efficiency of the LCC step. Also, nonlinear regression filters [52] can be investigated in future work.
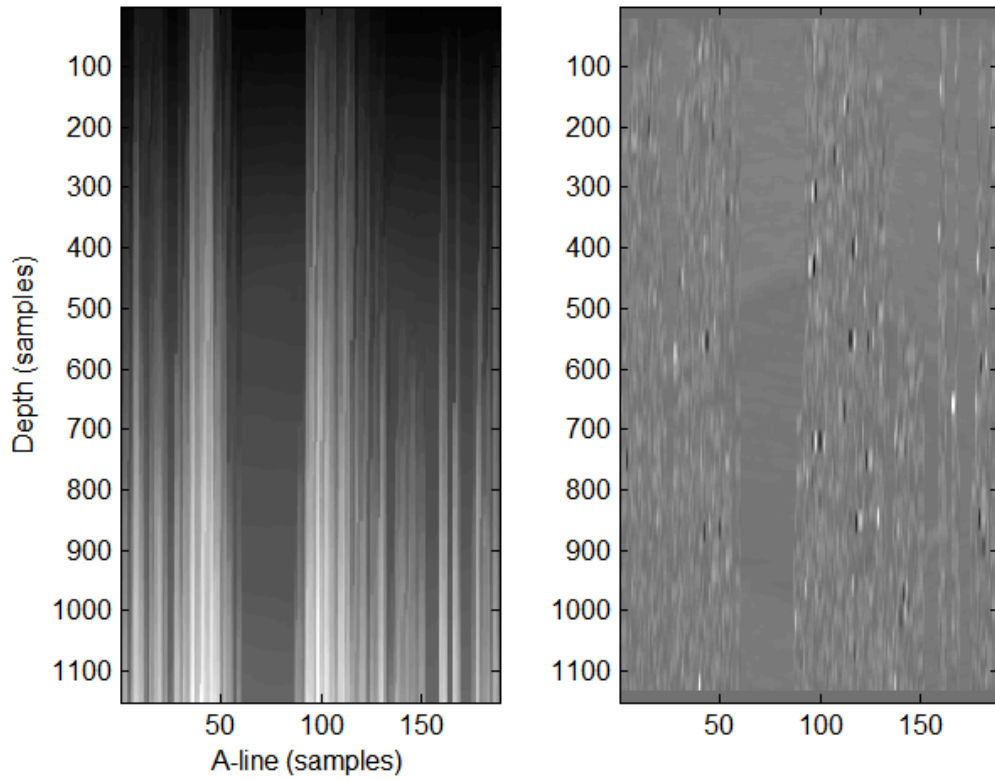
Figure 3.19: Axial (a) TDE and (strain) fields by applying ordinary linear regression as the LCC method in the optimized ES at block size = 11*11.
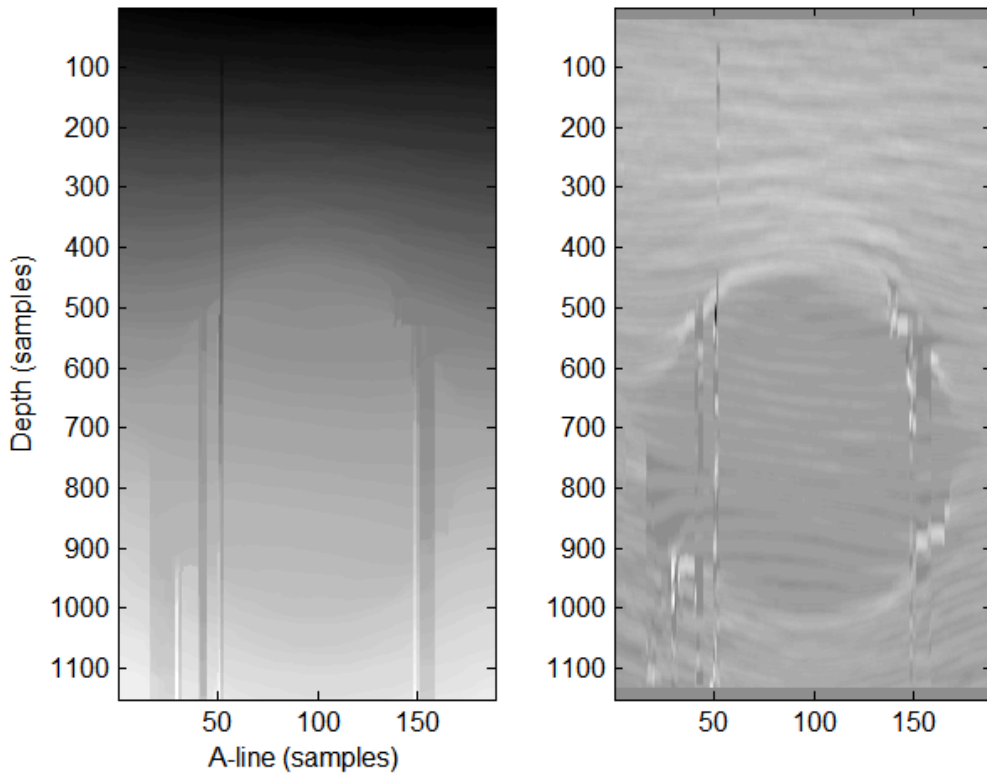
Figure 3.20: Axial (a) TDE and (strain) fields by applying ordinary linear regression as the LCC method in the optimized ES at block size = 33*33.
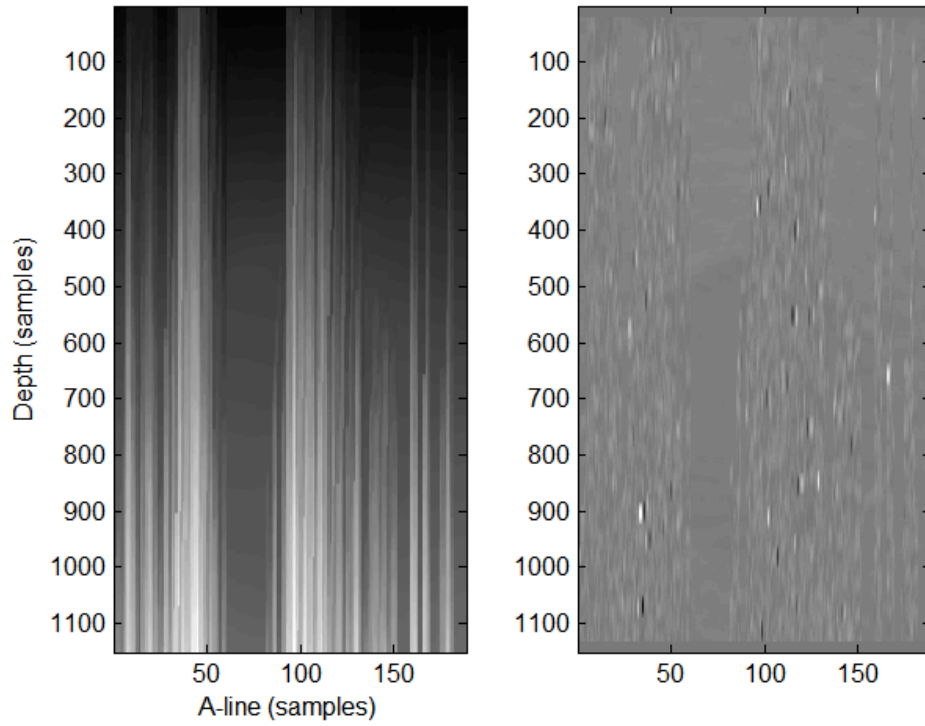
Figure 3.21: Axial (a) TDE and (strain) fields by applying robust linear regression (IRLS) as the LCC method in the optimized ES at block size = 11*11.
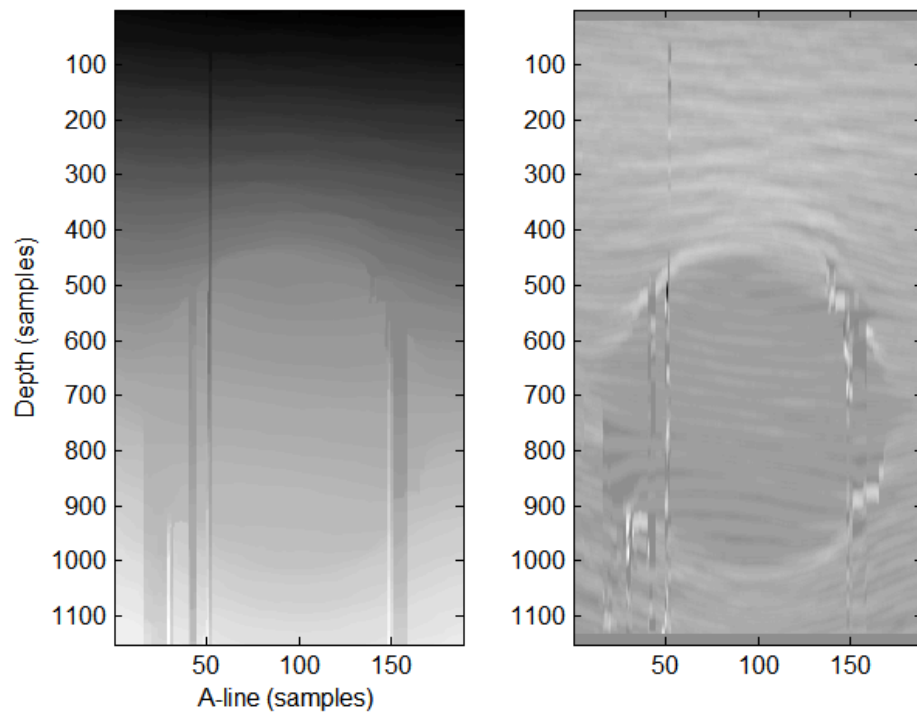


Figure 3.22: Axial (a) TDE and (strain) fields by applying robust linear regression (IRLS) as the LCC method in the optimized ES at block size = 33*33.

Table 3.7: Comparing t_{TDE} of the optimized ES algorithm when different LCC methods are used.

block size (samples)	11*11	33*33
t_{TDE} (s) (median)	31.27	83.57
t_{TDE} (s) (ordinary linear regression)	74.6	128.38
t_{TDE} (s) (robust linear regression)	202.14	275.08

3.5. Enhancing Strain Estimation

As stated before, axial strain generation from axial TDE field by direct spatial derivation (finite differences) amplifies noise in the resulting elastogram. This problem was alleviated by using the LSQSE method for strain generation and yielded appropriate results. However, some discontinuities that propagate from the TDE step to the strain generation step manifest in the resulting strain elastogram. Consequently, we tested further postprocessing of the resultant strain field (i.e. after the strain generation step) to enhance visual quality. 2D median filtration and Kalman filtration effects on the resulting strain elastogram (already generated by LSQSE) are shown in the following sections.

3.5.1. 2D Median Filtration

1D median filtration was already used in the LCC step in TDE to enhance lateral continuity. We also tested 2D median filtration effect on strain quality. The results of applying 2D median filtration (for constrained optimized ES block size = 21*21 samples) on strain generated by LSQSE are shown in Figure 3.23 and Figure 3.24 for different kernel sizes (square) of the 2D median filter. The reader can see the visual enhancement incurred by median postprocessing on strain elastogram (compared to the case of no postprocessing in Figure 3.12(d)). Some discontinuities begin to disappear gradually as the kernel size gets bigger. Also, the effect of kernel size on quantitative measures of the strain elastogram is shown in Figure 3.25 and Figure 3.26. The enhancement in both SNR_e and CNR_e conforms with the enhancement in visual quality. From Figure 3.27, we can see that the postprocessing step runtime, t_{pp}, using 2D median filtration is very small relative to the TDE step runtime reported before, t_{TDE} (even with small BMA kernels – see Figure 3.17). 2D median filtration proved to be effective for overall continuity checking and discontinuity removal in 2D (both axial and lateral).
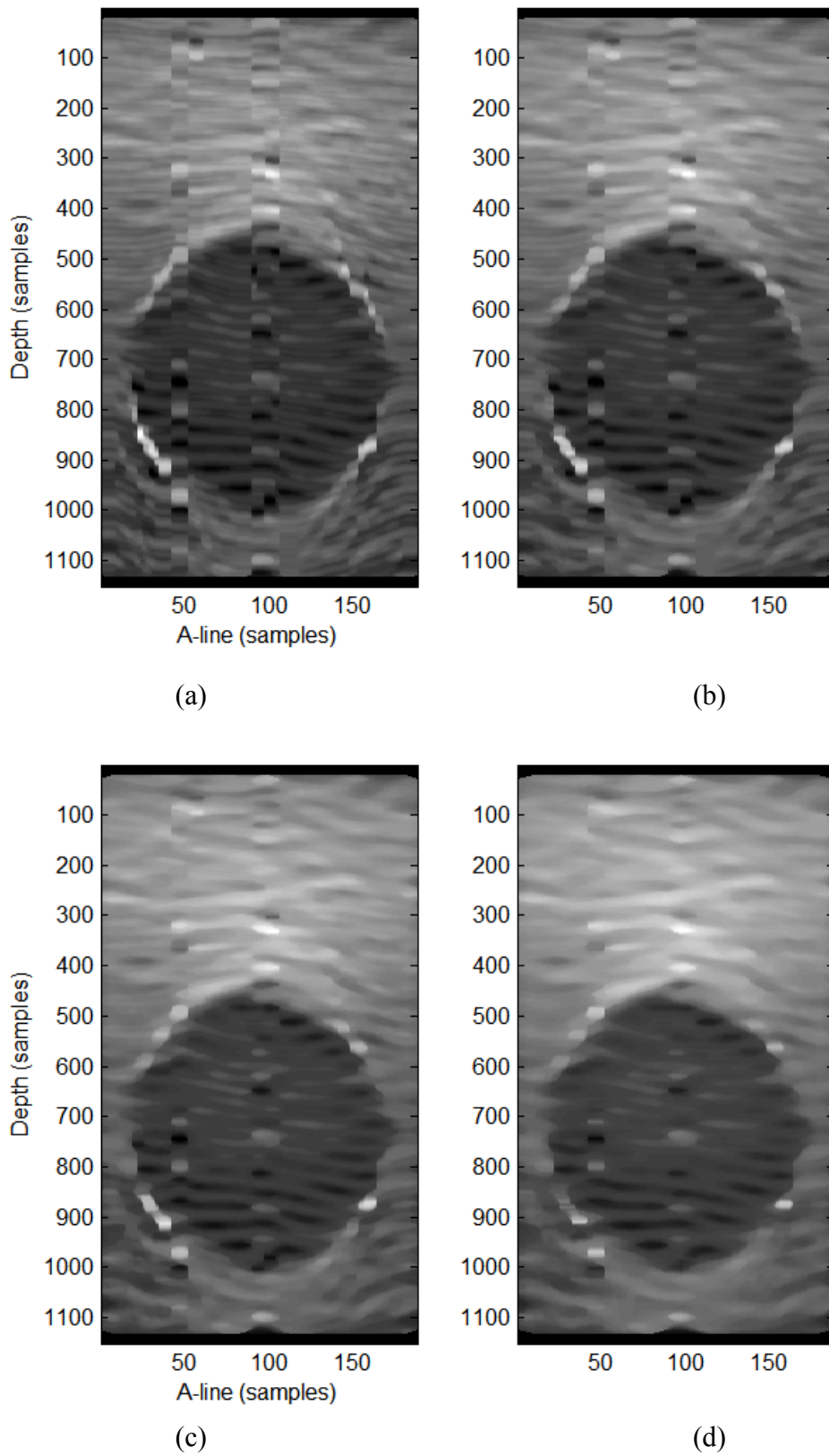
Figure 3.23: Postprocessing the axial strain field (by optimized ES at block size = 21*21) with 2D median filtration of different window sizes ((a) 5*5, (b) 9*9, (c) 13*13, (d) 17*17).

(a)

(b)

(c)

(d)
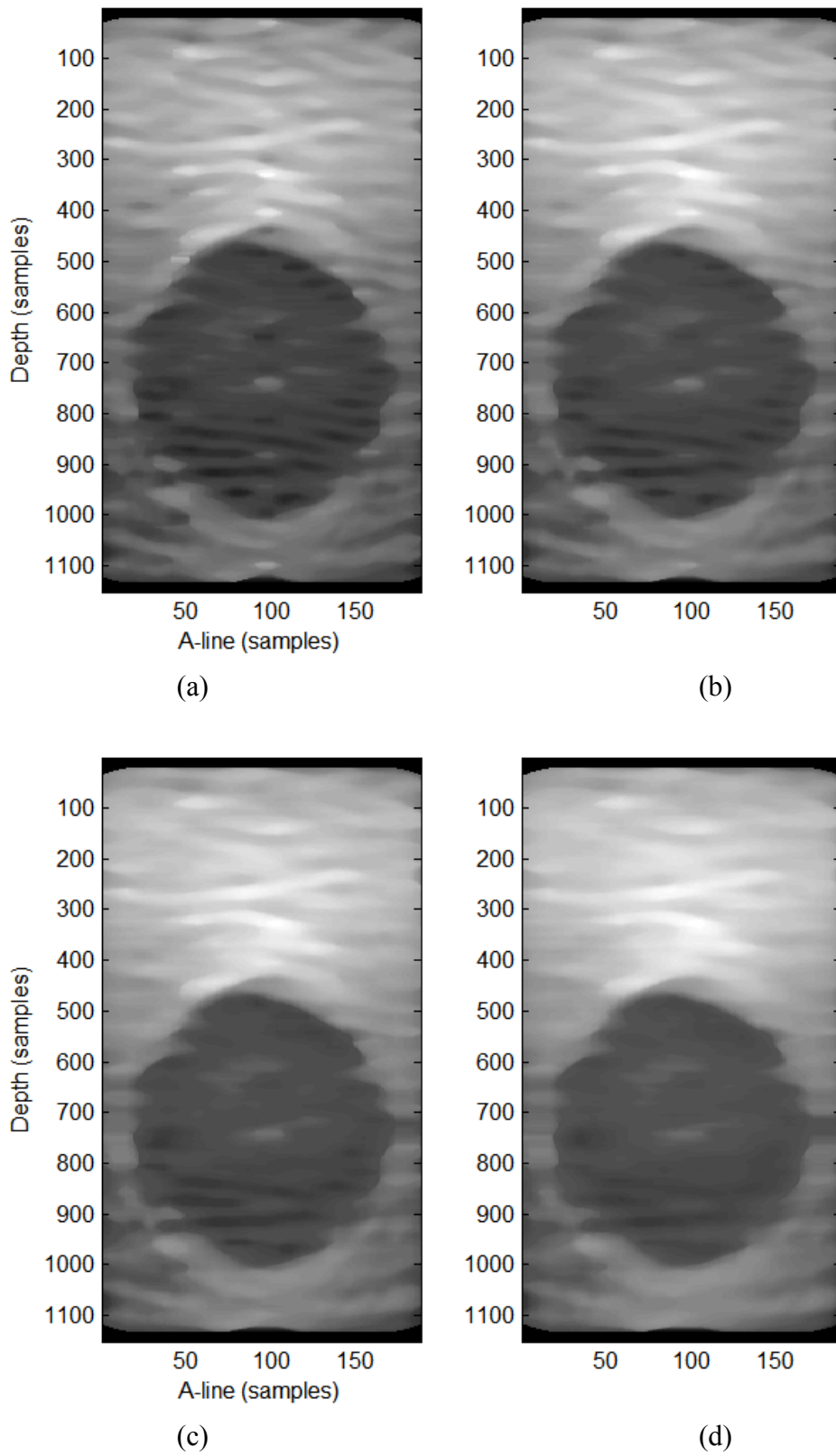
Figure 3.24: Postprocessing the axial strain field (by optimized ES at block size = 21*21) with 2D median filtration of different window sizes ((a) 21*21, (b) 25*25, (c) 29*29, (d) 33*33).
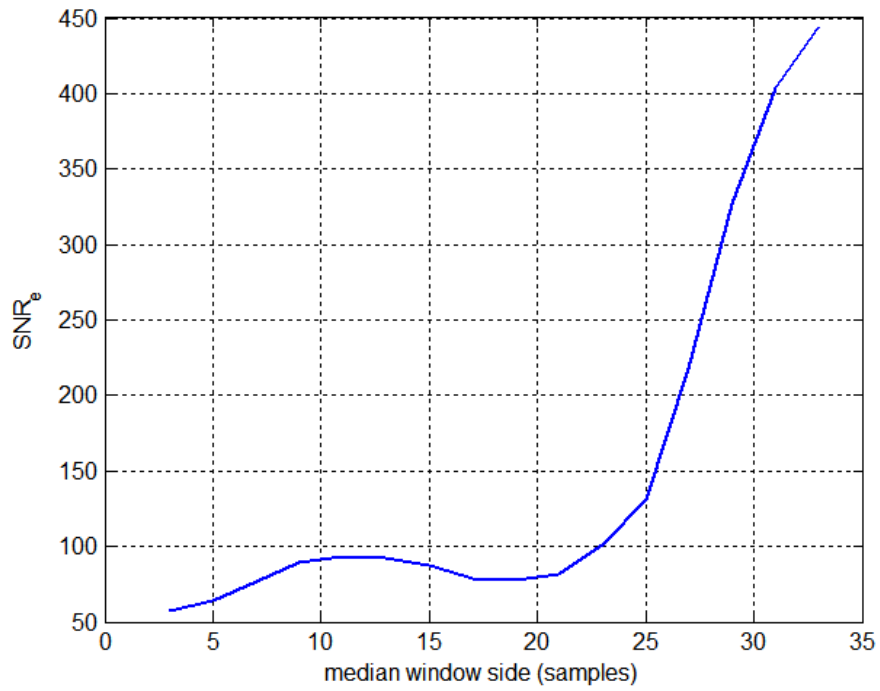
Figure 3.25: The effect of the window size of the postprocessing 2D median filter on SNR_e.
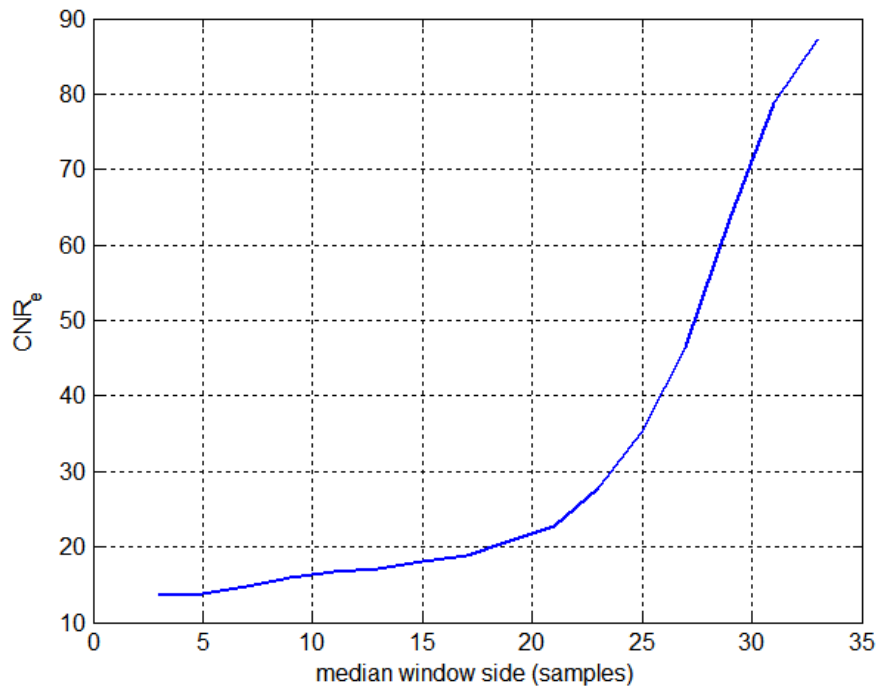
Figure 3.26: The effect of the window size of the postprocessing 2D median filter on CNR_e.
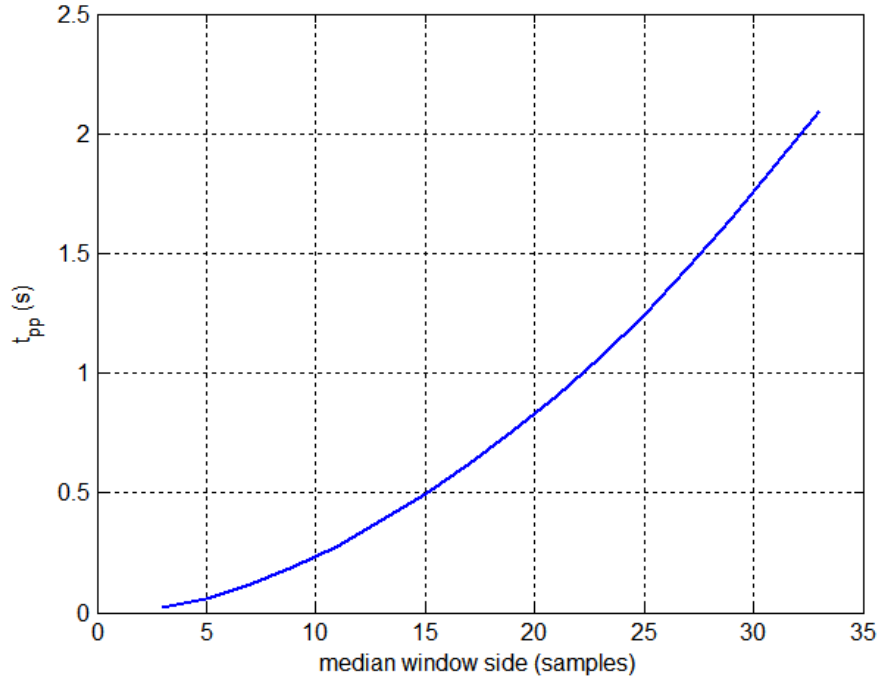
Figure 3.27: The effect of the window size of the postprocessing 2D median filter on t_{pp}.

3.5.1.   Kalman Filtration

In the LSQSE, adjacent RF lines are processed independently in axial strain calculation. However, the strain value of each pixel can hardly be considered independent from the strain value of its lateral neighbors. The only exception is the boundary of two tissue types with different mechanical properties where the strain field is discontinuous. This prior of piecewise strain continuity was exploited in [25] via a Kalman filter to improve the quality of strain estimation [54, 55]. In this method, the axial strain is calculated first using LSQSE as before. The axial continuity of the strain field is maintained in this step. Then, the Kalman filter is applied in the lateral direction. This step ensures continuity in the lateral direction.

We applied this technique to the axial TDE generated by our algorithm (constrained optimized ES) to get the axial strain fields shown in Figure 3.28 and Figure 3.29 for different block sizes. In these figures, the axial strain field for each block size without the Kalman filter is compared to itself with Kalman filtration to show the noise reduction caused by Kalman filtration. Compared to 2D median filtration in Figure 3.23 and Figure 3.24, the Kalman filter removes the noise from the strain image with minimal blurring and does not require manual selection of filtration window size. The quantitative measures in Table 3.8 are improved over the measures in Table 3.6 without Kalman filtration. This conforms with visual assessment.
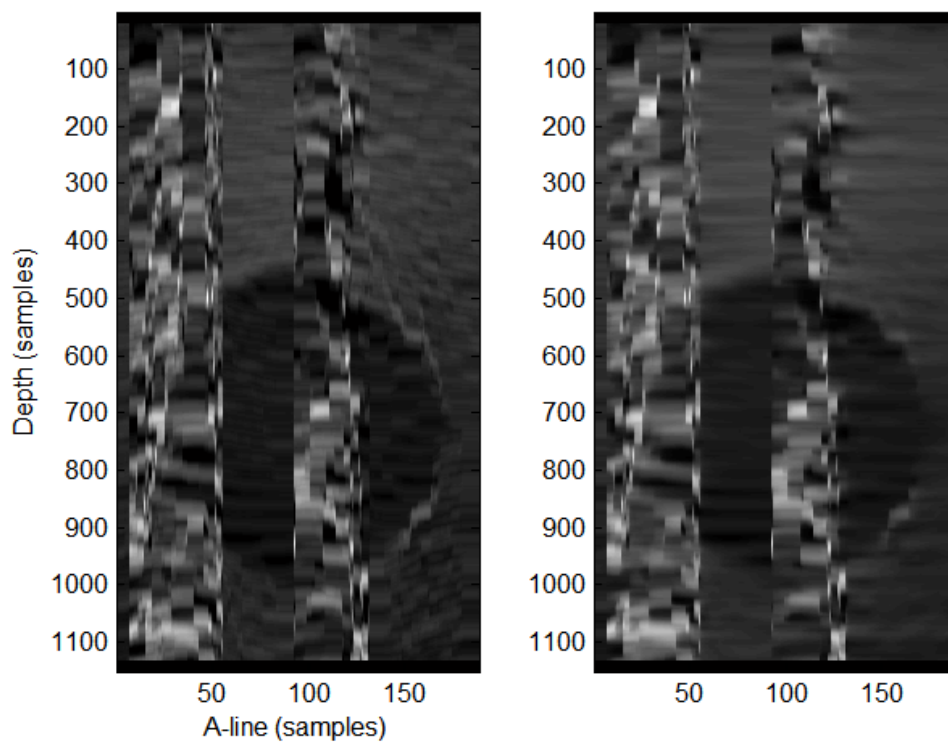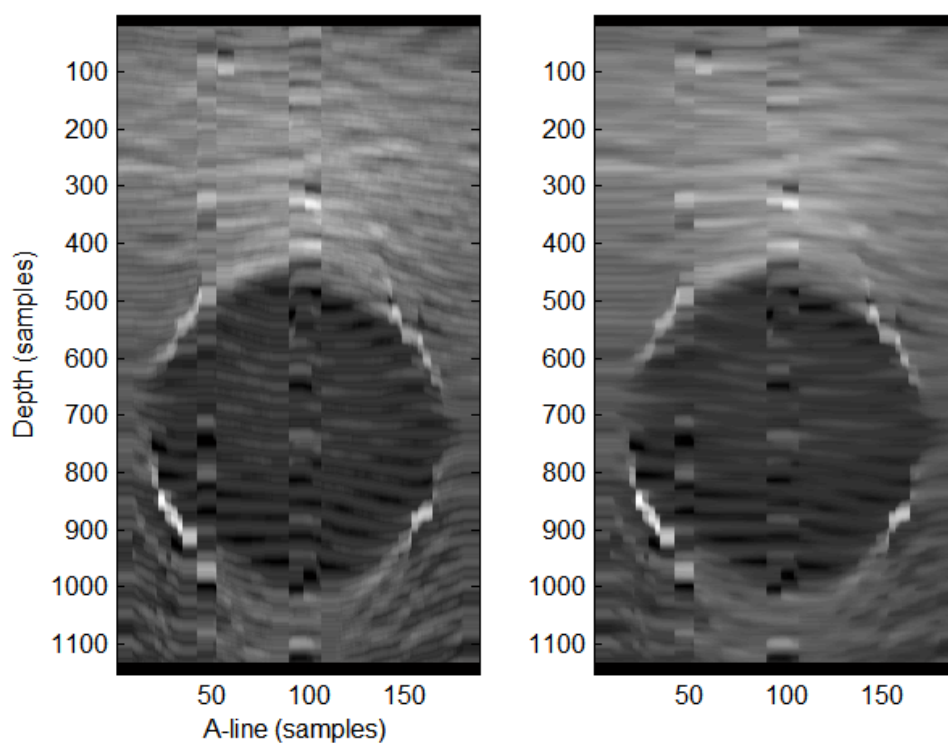
Figure 3.28: The axial strain (a) before and (b) after postprocessing by Kalman filtration (block size = 11*11). The axial strain (c) before and (d) after postprocessing by Kalman filtration (block size = 21*21).
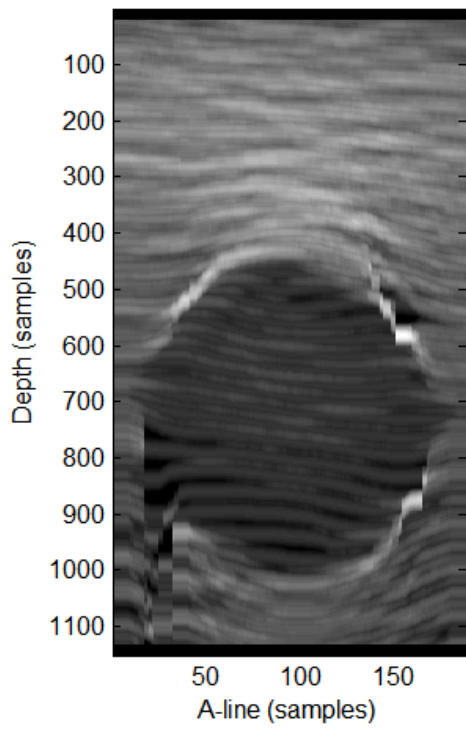
(a)
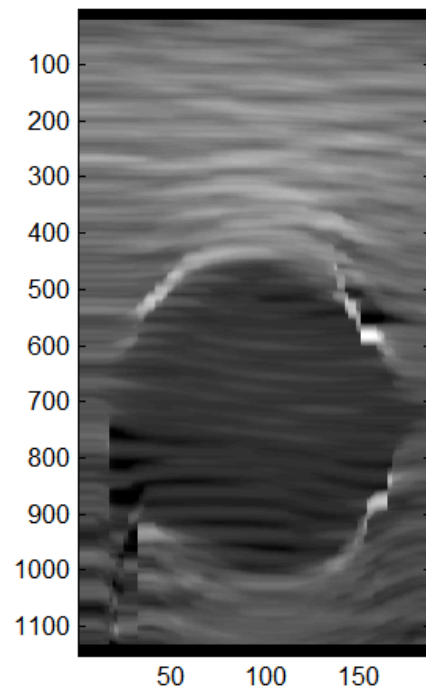
(b)
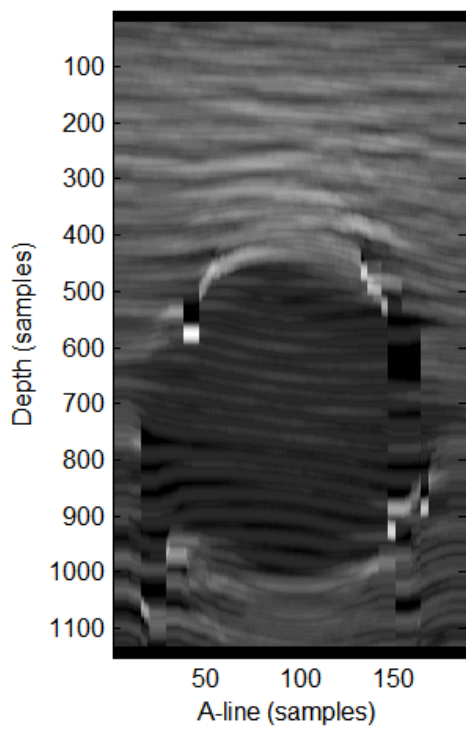
(c)
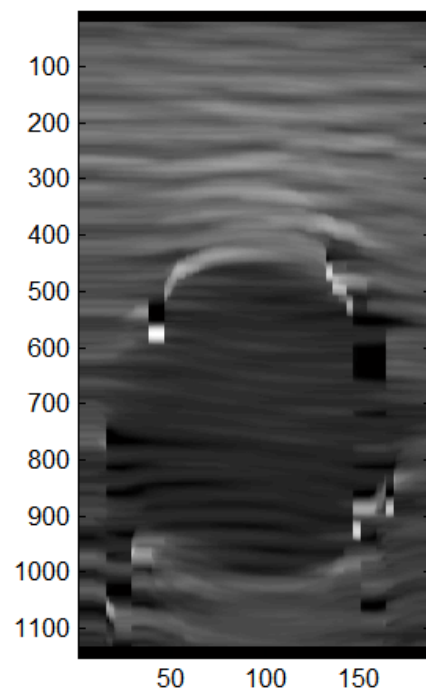
(d)

Figure 3.29: The axial strain (a) before and (b) after postprocessing by Kalman filtration (block size = 33*33). The axial strain (c) before and (d) after postprocessing by Kalman filtration (block size = 41*41).

Table 3.8: Quantitative measurements of axial strain generated by optimized ES with all constraints and postprocessed by Kalman filtration.

block size (samples)	11*11	21*21	33*33	41*41
SNR_e	12.34	11.09	8.81	7.31
CNR_e	0.48	6.14	6.18	4.69

3.6. Summary

In this chapter, we proposed a modified version of the ES algorithm to make it more oriented to work with US data. After examining the problems in the results, we utilized the inherent axial continuity in the imaged phantom (mimicking soft tissues) to further optimize modified ES. Results indicated that the lateral continuity of the axial TDE should also be taken into account. So, we tested three techniques (median, ordinary regression and robust regression correction) to do LCC. Additional constraints on the TDE were imposed to reduce discontinuities. Also, we tested the effects of the block size and postprocessing (by 2D median and Kalman filtration) on the estimation output. From Figure 3.30, it could be seen that the optimized 2D ES algorithm does not suffer from the problems of the basic 1D gated CC (the basic elastography approach) discussed in 2.4.

(a)   (b)
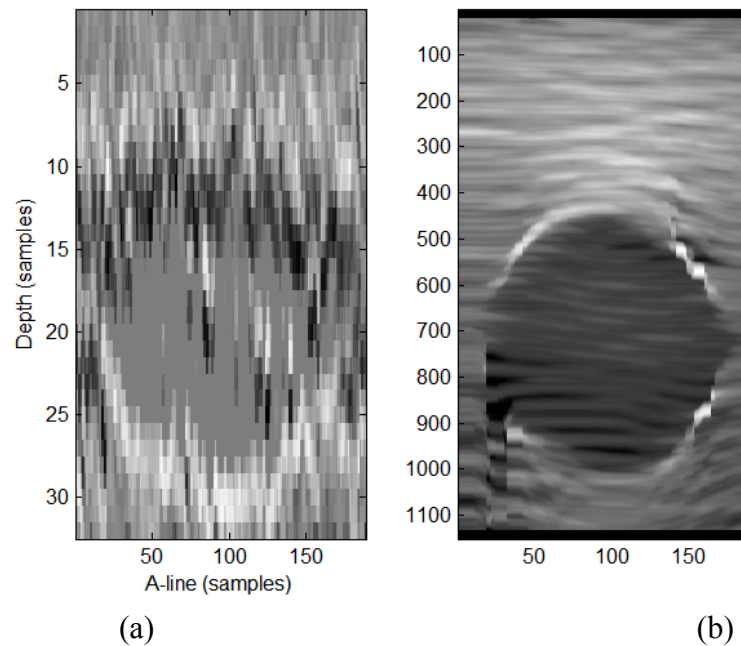
Figure 3.30: axial strain generated by (a) 1D gated CC (basic approach), and (b) 2D optimized ES with all constraints applied. Note that (b) is dense and smoother

than (a) due to continuity constrains. Overall, the optimized 2D ES algorithm does not suffer from the problems of the basic 1D gated CC.

Chapter 4 : Conclusion and Future Work

We presented an optimized version of the ES algorithm that exploits the inherent continuity in the successive US images to generate axial TDE and strain fields. The proposed algorithm was applied to elasticity phantom data. Results indicate that this direction is promising. All of the enhancements introduced to the TDE problem by means of 2D block matching yielded axial TDE and strain fields that are less noisy and more comprehensible than the results of the basic 1D gated CC algorithm and even the modified ES algorithm as seen in Figure 3.30. Overall, in optimized 2D ES, the stiff inclusion (representing lesions) can be delineated and differentiated from the soft material (representing healthy tissue of some echogenity as the stiff inclusion) compared to the normal B-mode image as seen in Figure 4.1.

(a)   (b)
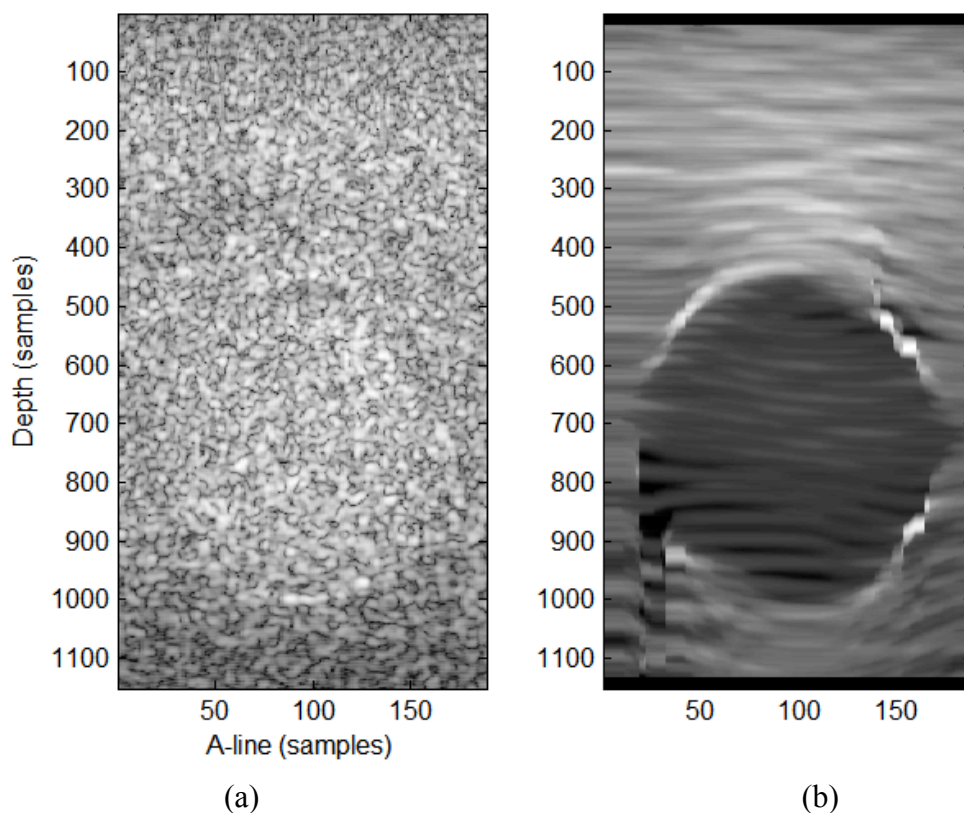
Figure 4.1: (a) B-mode image and (b) axial strain field by 2D optimized ES with all constraints applied.

Many points are potential to future work. In this study, we could investigate the image processing parameters effects as we experimented on phantom RF dataset already acquired, but we need to investigate the effects of US imaging params (e.g. f_c, BW, beamforming) on the TDE process. More constraints that were discussed before in

studies like Pellot-Barkat et al. [56], Shi and Varghese [57], Yeung et al. [40] and Zhu et al. [58] can be added to the cost function to enhance detection and runtime and reduce discontinuities. For example, the Cohen & Dinstein (CD2) cost function [59] is more suitable with US data as it incorporates the characteristics of the US imaging modality which considers the multiplicative speckle noise in US images. In our study of 2D BMAs, we did not perform 2D temporal stretching, which is expected to further enhance the results of the optimized ES algorithm by removing the scaling effect between the two tissue states (pre and postcompression) [22, 38, 60]. Clinical trials with different applied strain levels and more quantitative measures are needed to better assess the robustness of our algorithm to less bounded conditions found in in-vivo imaging and other challenges (like inherent pulsations and blood movement in the human body).

To enhance the runtime of the algorithm, several approaches are possible. But we need to study the asymptotic performance of the optimized ES with all constraints applied. We can use non-overlapping blocks for the reference image (like the case in MPEG motion estimation) to enhance speed then interpolate the displacement of skipped positions. Another approach is to apply motion estimation algorithm to undersampled versions of the RF frames then upsample the resulting displacement fields. A third approach is to make a parallel implementation of the motion estimation algorithm to leverage the power of multiple CPUs and GPUs [39].

References

[1] J. Ophir, S. K. Alam, B. S. Garra, F. Kallel, E. E. Konofagou, T. Krouskop, C. R. Merritt, R. Righetti, R. Souchon, and S. Srinivasan, "Elastography: imaging the elastic properties of soft tissues with ultrasound," *Journal of Medical Ultrasonics,* vol. 29, pp. 155-171, 2002.

[2] J. Ophir, S. Alam, B. Garra, F. Kallel, E. Konofagou, T. Krouskop, and T. Varghese, "Elastography: ultrasonic estimation and imaging of the elastic properties of tissues," *Proceedings of the Institution of Mechanical Engineers, Part H: Journal of Engineering in Medicine,* vol. 213, pp. 203-233, 1999.

[3] B. Ebbell, *The Papyrus Ebers: the greatest Egyptian medical document*: Levin & Munksgaard, 1937.

[4] G. H. SAKORAFAS and M. SAFIOLEAS, "Breast cancer surgery: an historical narrative. Part I. From prehistoric times to Renaissance," *European Journal of Cancer Care,* vol. 18, pp. 530-544, 2009.

[5] M. J. Stone, B. E. Aronoff, W. P. Evans, J. W. Fay, Z. Lieberman, C. M. Matthews, G. J. Race, R. P. Scruggs, and C. A. Stringer, "History of the baylor charles a. sammons cancer center," *Proceedings (Baylor University. Medical Center),* vol. 16, p. 30, 2003.

[6] P. H. Gann, "Interpreting recent trends in prostate cancer incidence and mortality," *Epidemiology,* vol. 8, pp. 117-120, 1997.

[7] J. Ferlay, H. R. Shin, F. Bray, D. Forman, C. Mathers, and D. M. Parkin, "Estimates of worldwide burden of cancer in 2008: GLOBOCAN 2008," *International journal of cancer,* vol. 127, pp. 2893-2917, 2010.

[8] M. Richard Clements, "The role of transrectal ultrasound in diagnosing prostate cancer," *Current urology reports,* vol. 3, pp. 194-200, 2002.

[9] J. Ophir, I. Cespedes, B. Garra, H. Ponnekanti, Y. Huang, and N. Maklad, "Elastography: ultrasonic imaging of tissue strain and elastic modulus in vivo," *European journal of ultrasound,* vol. 3, pp. 49-70, 1996.

[10] Y. Fung and S. Cowin, "Biomechanics: Mechanical properties of living tissues," *Journal of Applied Mechanics,* vol. 61, pp. 1007-1007, 1994.

[11] A. Sarvazyan, A. Scovoroda, and D. Vučelić, "Utilization of surface acoustic waves and shear acoustic properties for imaging and tissue characterization," in *Acoustical Imaging*, ed: Springer, 1992, pp. 463-467.

[12] K. Parker, S. Huang, R. Musulin, and R. Lerner, "Tissue response to mechanical vibrations for "sonoelasticity imaging"," *Ultrasound in medicine & biology,* vol. 16, pp. 241-246, 1990.

[13] M. Walz, J. Teubner, and M. Georgi, "Elasticity of benign and malignant breast lesions, imaging, applications and results in clinical and general practice," in *Eight International Congress of Ultrasonic Examination of the breast*, 1993.

[14] T. A. Krouskop, T. M. Wheeler, F. Kallel, B. S. Garra, and T. Hall, "Elastic moduli of breast and prostate tissues under compression," *Ultrasonic imaging,* vol. 20, pp. 260-274, 1998.

[15] P. S. Wellman, "Tactile imaging," Ph.D. Thesis, Harvard University, 1999.

[16] R. O. Cleveland and O. A. Sapozhnikov, "Modeling elastic wave propagation in kidney stones with application to shock wave lithotripsy," *The Journal of the Acoustical Society of America,* vol. 118, p. 2667, 2005.

[17] G. D. Ludwig and F. W. Struthers, "Considerations underlying the use of ultrasound to detect gallstones and foreign bodies in tissue," DTIC Document1949.

[18] C. Rados, "FDA Cautions Against Ultrasound" Keepsake" Images," *FDA Consumer Magazine. www. fda. gov/fdac/features/2004/104_images. html. Accessed,* vol. 11, 2005.

[19] J. Ophir, I. Cespedes, H. Ponnekanti, Y. Yazdi, and X. Li, "Elastography: a quantitative method for imaging the elasticity of biological tissues," *Ultrasonic imaging,* vol. 13, pp. 111-134, 1991.

[20] T. Varghese and J. Ophir, "Performance optimization in elastography: Multicompression with temporal stretching," *Ultrasonic imaging,* vol. 18, pp. 193-214, 1996.

[21] E. Céspedes, "Elastography: Imaging of biological tissue elasticity," Ph.D. dissertation, University of Houston, 1993.

[22] M. A. Lubinski, S. Y. Emelianov, K. Raghavan, A. E. Yagle, A. R. Skovoroda, and M. O'Donnell, "Lateral displacement estimation using tissue incompressibility," *Ultrasonics, Ferroelectrics and Frequency Control, IEEE Transactions on,* vol. 43, pp. 247-256, 1996.

[23] E. Konofagou and J. Ophir, "A new elastographic method for estimation and imaging of lateral displacements, lateral strains, corrected axial strains and Poisson's ratios in tissues," *Ultrasound in medicine & biology,* vol. 24, pp. 1183-1199, 1998.

[24] H. Rivaz, E. Boctor, P. Foroughi, R. Zellars, G. Fichtinger, and G. Hager, "Ultrasound elastography: a dynamic programming approach," *Medical Imaging, IEEE Transactions on,* vol. 27, pp. 1373-1377, 2008.

[25] H. Rivaz, E. M. Boctor, M. A. Choti, and G. D. Hager, "Real-time regularized ultrasound elastography," *Medical Imaging, IEEE Transactions on,* vol. 30, pp. 928-945, 2011.

[26] S. Srinivasan, R. Righetti, and J. Ophir, "Trade-offs between the axial resolution and the signal-to-noise ratio in elastography," *Ultrasound in Medicine and Biology,* vol. 29, pp. 847-866, 2003.

[27] T. Varghese and J. Ophir, "Estimating tissue strain from signal decorrelation using the correlation coefficient," *Ultrasound in medicine & biology,* vol. 22, pp. 1249-1254, 1996.

[28] E. E. Konofagou, T. Varghese, and J. Ophir, "Spectral estimators in elastography," *Ultrasonics,* vol. 38, pp. 412-416, 2000.

[29] M. O'Donnell, A. Skovorada, and B. Shapo, "Measurement of arterial wall motion using Fourier based speckle tracking algorithms," in *Ultrasonics Symposium, 1991. Proceedings., IEEE 1991*, 1991, pp. 1101-1104.

[30] R. Zahiri-Azar and S. E. Salcudean, "Motion estimation in ultrasound images using time domain cross correlation with prior estimates," *Biomedical Engineering, IEEE Transactions on,* vol. 53, pp. 1990-2000, 2006.

[31] S. K. Alam and J. Ophir, "Reduction of signal decorrelation from mechanical compression of tissues by temporal stretching: Applications to elastography," *Ultrasound in medicine & biology,* vol. 23, pp. 95-105, 1997.

[32] I. Céspedes and J. Ophir, "Reduction of image noise in elastography," *Ultrasonic imaging,* vol. 15, pp. 89-102, 1993.

[33] E. Turgay, "Imaging visco-elastic properties of soft tissue with ultrasound," M.Sc. thesis, University of British Columbia, 2004.

[34] S. K. Alam, J. Ophir, and E. E. Konofagou, "An adaptive strain estimator for elastography," *Ultrasonics, Ferroelectrics and Frequency Control, IEEE Transactions on,* vol. 45, pp. 461-472, 1998.

[35] I. Cespedes, Y. Huang, J. Ophir, and S. Spratt, "Methods for estimation of subsample time delays of digitized echo signals," *Ultrasonic imaging,* vol. 17, pp. 142-171, 1995.

[36] F. Kallel and J. Ophir, "A least-squares strain estimator for elastography," *Ultrasonic imaging,* vol. 19, pp. 195-208, 1997.

[37] R. Righetti, J. Ophir, and P. Ktonas, "Axial resolution in elastography," *Ultrasound in medicine & biology,* vol. 28, pp. 101-113, 2002.

[38] P. Chaturvedi, M. F. Insana, and T. J. Hall, "2-D companding for noise reduction in strain imaging," *Ultrasonics, Ferroelectrics and Frequency Control, IEEE Transactions on,* vol. 45, pp. 179-191, 1998.

[39] X. Yang, S. Deka, and R. Righetti, "A hybrid CPU-GPGPU approach for real-time elastography," *Ultrasonics, Ferroelectrics and Frequency Control, IEEE Transactions on,* vol. 58, pp. 2631-2645, 2011.

[40] F. Yeung, S. F. Levinson, D. Fu, and K. J. Parker, "Feature-adaptive motion tracking of ultrasound image sequences using a deformable mesh," *Medical Imaging, IEEE Transactions on,* vol. 17, pp. 945-956, 1998.

[41] M. H. Hussein and Y. M. Kadah, "Ultrasound Elastography as A Motion Estimation Problem," in *International Conference on Computer Medical Applications (ICCMA)*, Sousse, Tunisia, 2013.

[42] M. H. Hussein and Y. M. Kadah, "Motion Estimation for Ultrasound Elastography Using Optimized Block Matching with Lateral Continuity Correction," in *National Radio Science Conference (NRSC)*, Egypt, 2013.

[43] A. Barjatya, "Block matching algorithms for motion estimation," ed: unpublished.

[44] I. Hein and W. D. O'Brien Jr, "Current time-domain methods for assessing tissue motion by analysis from reflected ultrasound echoes-a review," *Ultrasonics, Ferroelectrics and Frequency Control, IEEE Transactions on,* vol. 40, pp. 84-102, 1993.

[45] W. Khaled and H. Ermert, "Ultrasonic strain imaging and reconstructive elastography for biological tissue," in *Bioengineering in Cell and Tissue Research*, ed: Springer, 2008, pp. 103-132.

[46] Y. Honjo, H. Hasegawa, and H. Kanai, "Optimization of Correlation Kernel Size for Accurate Estimation of Myocardial Contraction and Relaxation," *Jpn. J. Appl. Phys,* vol. 51, p. 07GF06, 2012.

[47] H. Liebgott, J. Wilhjehm, J. A. Jensen, D. Vray, and P. Delachartre, "PSF dedicated to estimation of displacement vectors for tissue elasticity imaging with ultrasound," *Ultrasonics, Ferroelectrics and Frequency Control, IEEE Transactions on,* vol. 54, pp. 746-756, 2007.

[48] R. F. Wagner, S. W. Smith, J. M. Sandrik, and H. Lopez, "Statistics of speckle in ultrasound B-scans," *IEEE TRANS. SONICS ULTRASONICS.,* vol. 30, pp. 156-163, 1983.

[49] J. A. Jensen and P. Munk, "A new method for estimation of velocity vectors," *Ultrasonics, Ferroelectrics and Frequency Control, IEEE Transactions on,* vol. 45, pp. 837-851, 1998.

[50] M. Aderson, "Multi-dimensional velocity estimation with ultrasound using spatial quadrature," *Ultrasonics, Ferroelectrics and Frequency Control, IEEE Transactions on,* vol. 45, pp. 852-861, 1998.

[51] S. Fleishman, D. Cohen-Or, and C. T. Silva, "Robust moving least-squares fitting with sharp features," in *ACM Transactions on Graphics (TOG)*, 2005, pp. 544-552.

[52] H. J. Motulsky and R. E. Brown, "Detecting outliers when fitting data with nonlinear regression–a new method based on robust nonlinear regression and the false discovery rate," *BMC bioinformatics,* vol. 7, p. 123, 2006.

[53] P. W. Holland and R. E. Welsch, "Robust regression using iteratively reweighted least-squares," *Communications in Statistics-Theory and Methods,* vol. 6, pp. 813-827, 1977.

[54] G. Welch and G. Bishop, "An introduction to the Kalman filter," ed, 1995.

[55] R. Dugad and N. Ahuja, "Video denoising by combining Kalman and Wiener estimates," in *Image Processing, 1999. ICIP 99. Proceedings. 1999 International Conference on*, 1999, pp. 152-156.

[56] C. Pellot-Barakat, F. Frouin, M. F. Insana, and A. Herment, "Ultrasound elastography based on multiscale estimations of regularized displacement fields," *Medical Imaging, IEEE Transactions on,* vol. 23, pp. 153-163, 2004.

[57] H. Shi and T. Varghese, "Two-dimensional multi-level strain estimation for discontinuous tissue," *Physics in Medicine and Biology,* vol. 52, p. 389, 2007.

[58] Y. Zhu, P. Chaturvedi, and M. F. Insana, "Strain imaging with a deformable mesh," *Ultrasonic imaging,* vol. 21, pp. 127-146, 1999.

[59] B. Cohen and I. h. Dinstein, "New maximum likelihood motion estimation schemes for noisy ultrasound images," *Pattern Recognition,* vol. 35, pp. 455-463, 2002.

[60] P. Chaturvedi, M. F. Insana, and T. J. Hall, "Testing the limitations of 2-D companding for strain imaging using phantoms," *Ultrasonics, Ferroelectrics and Frequency Control, IEEE Transactions on,* vol. 45, pp. 1022-1031, 1998.

الملخص

تصوير المرونة هي طريقة واعدة للتصوير الطبي لتوزيع خصائص المرونة في منطقة معينة من الجسم. يقوم هذا الأسلوب بترجمة توزيع المعاملات المتصلة بالسمات الميكانيكية في الهدف المصور الى معلومات بصرية ملونة. في التصوير الطبي، يتم دراسة تصوير المرونة كأداة تشخيصية فعالة في الكشف عن التغيرات المرضية في الأنسجة الرخوة من خلال مراقبة تغيرات صلابة الأنسجة. على سبيل المثال، يظهر سرطان الثدي كعقيدات صلدة للغاية في صورة المرونة التشخيصية.

توجد الكثير من الطرق لتقدير حركة الانسجة في تصوير المرونة بالموجات فوق الصوتية. الطريقة الاساسية التي تقوم على ايجاد الارتباط المشترك من خلال النوافذ المتحركة احادية الابعاد لديها بعض العيوب. هذه الطريقة لا يمكن أن تعمل بشكل جيد تحت الضغوط المرتفعة ولا تستغل الانسيابية الكامنة في الأنسجة في تقديرها للحركة. وهذا يؤدي إلى خطوات زائدة عن الحد و وجود نقاط عدم اتصال في صورة المرونة.

يمكن ملاحظة أن خطوة تقدير الحركة في تصوير المرونة مشابهة لمرحلة تقدير الحركة في تطبيقات ضغط الفيديو. وعلى الرغم من وجود بعض الاختلافات بين طبيعة صورة الموجات فوق الصوتية والصورة الفوتوغرافية، فانه يمكن استخدام طرق مطابقة الكتل ثنائية الابعاد مع صور الموجات فوق الصوتية ذات التردد الراديوي لانتاج مجالات حركة الانسجة.

في هذه الدراسة، نستعرض المبادئ الأساسية لتصوير المرونة. ثم نقدم الخطوات الاساسية لتقدير الحركة عن طريق ايجاد الارتباط المشترك من خلال النوافذ المتحركة احادية الابعاد وأثر كل خطوة على نسبة الضوضاء و التباين والوقت اللازم لحساب مجال الحركة. ثم نقوم بتقديم نسخة معدلة من احد طرق مطابقة الكتل ثنائية الابعاد و التي تجعلها صالحة اكثر للعمل مع صور الموجات فوق الصوتية. نقوم ايضا باستغلال الانسيابية الكامنة في الأنسجة المصورة لعمل طريقة أمثل من النسخة المعدلة سابقا. ثم نقوم بفرض قيود إضافية على طريقة تقدير الحركة للحد من نقاط الانفصال في الصور الناتجة. قمنا باختبار تأثير بعض المعاملات والمعالجات الاضافية على صور الحركة الناتجة. التقييمات الكمية والبصرية لصور حركة الانسجة الناتجة تبين أن التقنية الجديدة لا تعاني من نفس عيوب التقنية الاساسية. نختم اخيرا بالنقاط المستحقة للبحث في المستقبل لتحسين نوعية ووقت تشغيل الطريقة ثنائية الابعاد المقترحة لتقدير مجالات الحركة.

مهندس:	مروان حسن حسين محمد
تاريخ الميلاد:	1988\5\10
الجنسية:	مصري
تاريخ التسجيل:	2012\4
تاريخ المنح:	...........\.....\.....
القسم:	الهندسة الطبية الحيوية و المنظومات
الدرجة:	ماجستير

المشرفون:

ا.د. ياسر مصطفى قدح

الممتحنون:

أ.د.ياسر مصطفى قدح (المشرف الرئيسي)

أ.د. عبدالله سيد أحمد (الممتحن الداخلي)

أ.د. محمد إبراهيم العدوي (الممتحن الخارجي)

عنوان الرسالة:	طرق تكوين مجال الحركة في تصوير المرونة بالموجات فوق الصوتية

الكلمات الدالة:

تصوير المرونة، الموجات فوق الصوتية، طرق تقدير الحركة، طرق مطابقة الكتل ثنائية الابعاد، قيود انسيابية الانسجة.

ملخص الرسالة:

تصوير المرونة هي طريقة واعدة للتصوير الطبي لتوزيع خصائص المرونة في منطقة معينة من الجسم. يقوم هذا الأسلوب بترجمة توزيع المعاملات المتصلة بالسمات الميكانيكية في الهدف المصور الى معلومات بصرية ملونة. في التصوير الطبي، يتم دراسة تصوير المرونة كأداة تشخيصية فعالة في الكشف عن التغيرات المرضية في الأنسجة الرخوة من خلال مراقبة تغيرات صلابة الأنسجة. على سبيل المثال، يظهر سرطان الثدي كعقيدات صلدة للغاية في صورة المرونة التشخيصية.

توجد الكثير من الطرق لتقدير حركة الانسجة في تصوير المرونة بالموجات فوق الصوتية. الطريقة الاساسية التي تقوم على ايجاد الارتباط المشترك من خلال النوافذ المتحركة احادية الابعاد لديها بعض العيوب. هذه الطريقة لا يمكن أن تعمل بشكل جيد تحت الضغوط المرتفعة ولا تستغل الانسيابية الكامنة في الأنسجة في تقديرها للحركة. وهذا يؤدي إلى خطوات زائدة عن الحد و وجود نقاط عدم اتصال في صورة المرونة.

يمكن ملاحظة أن خطوة تقدير الحركة في تصوير المرونة مشابهة لمرحلة تقدير الحركة في تطبيقات ضغط الفيديو. وعلى الرغم من وجود بعض الاختلافات بين طبيعة صورة الموجات فوق الصوتية والصورة الفوتوغرافية، فانه يمكن استخدام طرق مطابقة الكتل ثنائية الابعاد مع صور الموجات فوق الصوتية ذات التردد الراديوي لانتاج مجالات حركة الانسجة.

في هذه الدراسة، نستعرض المبادئ الأساسية لتصوير المرونة. ثم نقدم الخطوات الاساسية

لتقدير الحركة عن طريق ايجاد الارتباط المشترك من خلال النوافذ المتحركة احادية الابعاد وأثر كل خطوة على نسبة الضوضاء و التباين والوقت اللازم لحساب مجال الحركة. ثم نقوم بتقديم نسخة معدلة من احد طرق مطابقة الكتل ثنائية الابعاد و التي تجعلها صالحة اكثر للعمل مع صور الموجات فوق الصوتية. نقوم ايضا باستغلال الانسيابية الكامنة في الأنسجة المصورة لعمل طريقة أمثل من النسخة المعدلة سابقا. ثم نقوم بفرض قيود إضافية على طريقة تقدير الحركة للحد من نقاط الانفصال في الصور الناتجة. قمنا باختبار تأثير بعض المعاملات والمعالجات الاضافية على صور الحركة الناتجة. التقييمات الكمية والبصرية لصور حركة الانسجة الناتجة تبين أن التقنية الجديدة لا تعاني من نفس عيوب التقنية الاساسية. نختم اخيرا بالنقاط المستحقة للبحث في المستقبل لتحسين نوعية ووقت تشغيل الطريقة ثنائية الابعاد المقترحة لتقدير مجالات الحركة.

عنوان الرسالة
طرق تكوين مجال الحركة في تصوير المرونة بالموجات فوق الصوتية

اعداد
مروان حسن حسين محمد

رسالة مقدمة إلى كلية الهندسة — جامعة القاهرة
كجزء من متطلبات الحصول على درجة الماجستير
في
الهندسة الطبية الحيوية والمنظومات

يعتمد من لجنة الممتحنين:

الاستاذ الدكتور: ياسر مصطفى قدح   المشرف الرئيسى

الاستاذ الدكتور: عبدالله سيد أحمد   الممتحن الداخلي

الاستاذ الدكتور: محمد إبراهيم العدوي   الممتحن الخارجي

كليـــة الهندســـة - جامعـــة القاهـــرة
الجيـزة - جمهوريـة مصـرالعربيـة

يونيو 2013

عنوان الرسالة

طرق تكوين مجال الحركة في تصوير المرونة بالموجات فوق الصوتية

اعداد

مروان حسن حسين محمد

رسالة مقدمة إلى كلية الهندسة ــ جامعة القاهرة
كجزء من متطلبات الحصول على درجة الماجستير
في
الهندسة الحيوية الطبية والمنظومات

تحت اشراف

ياسر مصطفى إبراهيم قدح
أستاذ بقسم الهندسة الحيوية الطبية
والمنظومات

كليــة الهندســة - جامعــة القاهــرة
الجيــزة - جمهوريــة مصـرالعربيــة

يونيو 2013

عنوان الرسالة

طرق تكوين مجال الحركة في تصوير المرونة بالموجات فوق الصوتية

اعداد

مروان حسن حسين محمد

رسالة مقدمة إلى كلية الهندسة — جامعة القاهرة
كجزء من متطلبات الحصول على درجة الماجستير
في
الهندسة الحيوية الطبية والمنظومات

كليــة الهندســة-جامعــة القاهــرة
الجيــزة-جمهوريــة مصــر العربيــة

يونيو 2013